

Arne Christian Rosenfeldt

Time-resolved photoelectron spectroscopy
of low energy excitations of
4x4 C₆₀ / Cu(111)

2009

Experimentelle Physik

Time-resolved photoelectron spectroscopy
of low energy excitations of
 4×4 C₆₀ / Cu(111)

Inaugural-Dissertation
zur Erlangung des Doktorgrades
der Naturwissenschaften im Fachbereich Physik
der Mathematisch-Naturwissenschaftlichen Fakultät
der Westfälischen Wilhelms-Universität Münster

vorgelegt von
Arne Christian Rosenfeldt
aus Braunschweig

–2009–

| | |
|-----------------------------|------------------------|
| Dekan: | Prof. Dr. J. Wessels |
| Erster Gutachter: | Prof. Dr. H. Zacharias |
| Zweiter Gutachter: | Prof. Dr. G. F. Hanne |
| Tag der mündlichen Prüfung: | 15.06.2009 |
| Tag der Promotion: | 15.06.2009 |

Contents

| | | |
|----------|---|-----------|
| 1 | Introduction | 1 |
| 1.1 | Electronic and vibronic states of the Buckminster Fullerene | 2 |
| 1.1.1 | Fullerite | 3 |
| 1.1.2 | Influence of nuclear motion | 5 |
| 1.1.3 | Dynamics | 8 |
| 1.1.4 | Thin films on Cu(111) | 10 |
| 1.2 | Electronic states in C ₆₀ | 10 |
| 1.2.1 | Photoemission | 12 |
| 1.2.2 | Time-resolved 2PPE from C ₆₀ | 14 |
| 1.2.2.1 | Two-photon absorption | 14 |
| 1.2.2.2 | Two-photon absorption in a statistical ensemble | 15 |
| 1.2.2.3 | Simulation: Solving the rate equations | 16 |
| 1.2.3 | Inverse photoemission in combination with UPS | 19 |
| 1.2.4 | Electrostatic effects | 19 |
| 2 | Experiment | 23 |
| 2.1 | Sample preparation | 23 |
| 2.1.1 | Calibration of the film thickness | 28 |
| 2.2 | Laser system | 30 |
| 2.2.1 | Optical parametric oscillator | 32 |
| 2.2.2 | Optical parametric amplifier | 33 |
| 2.3 | Photoemission | 35 |
| 2.3.1 | Approach | 35 |
| 2.3.2 | Set-up | 36 |
| 2.3.3 | Measurement software | 38 |
| 2.3.4 | Analysis | 38 |
| 2.3.4.1 | Photodiode signals | 38 |
| 2.3.4.2 | Separation of time-delay spectra into states | 39 |
| 2.3.4.3 | Positive populations | 41 |
| 2.3.4.4 | Minimum of a function | 42 |
| 2.3.4.5 | Fitting the simulation to the measured state dynamics | 43 |
| 3 | Two-photon photoemission on fullerite films | 45 |
| 3.1 | Spectroscopic results | 45 |
| 3.2 | Time-resolved results | 49 |
| 3.3 | Warm preparation | 51 |
| 3.3.1 | Singlet exciton | 51 |

Contents

| | | |
|----------|--|------------|
| 3.3.1.1 | Efficacy and lifetime dependencies | 59 |
| 3.3.1.2 | Interstate rate | 66 |
| 3.3.1.3 | Comparison with the literature and conclusions . . . | 67 |
| 3.3.2 | Triplet exciton | 68 |
| 3.3.2.1 | Dependence on film thickness and temperature . . . | 71 |
| 3.4 | Cold preparation | 75 |
| 3.4.1 | Efficacy dependence on photon energy | 76 |
| 3.4.2 | Improved beam overlap | 79 |
| 3.4.3 | Conclusions | 82 |
| 4 | Summary | 83 |
| 4.1 | German translation | 85 |
| A | Ellipsometry details | 87 |
| B | References | 89 |
| C | Lebenslauf | 99 |
| D | Acknowledgment | 100 |

1 Introduction

The low-energy vibronic excitations of the 4×4 reconstruction of C_{60} thin films on Cu(111) are investigated by time-resolved two-photon photoelectron spectroscopy in this thesis. Carbon atoms have been known for a long time to condense in crystal forms as graphite and as diamond, which is metastable at a temperature of 300 K and a pressure of 101 kPa [1]. A wide variety of non-crystalline structures is commonly known as soot or coal.

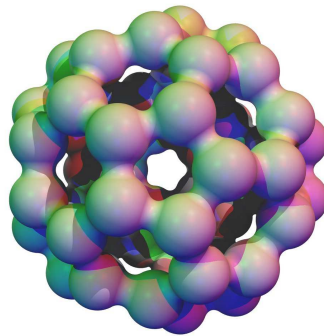


Figure 1.1: The geometric structure of C_{60} is a truncated icosahedron.

One special non-crystalline form is C_{60} . The basic geometric structure is, as shown in figure 1, a truncated icosahedron. This structure has been discussed by Archimedes, Euler, and Kepler [2]. In their 1985 Noble Prize winning investigation Kroto and coworkers [3] found C_{60} using mass spectroscopy of soot. Starting from initial guesses it was eventually proven to have that specific geometric structure of a truncated icosahedron and the molecule was named “Buckminster Fulleren”. C_{60} molecules condense — this time by means of van der Waals bindings — into a crystal which is called fullerite. Fullerite is a semiconductor and thus may be useful in electronics [4, 5] and solar cells [6–9]. In the present investigation, the electronic structure of up to 100 monolayers (ML) fullerite on Cu(111) is studied. The focus is on the low-lying, long-living excited states, especially the triplet exciton for which up to now no lifetime τ is known. Gruen and coworkers [10] measured a lifetime of $400\ \mu\text{s}$ for C_{60} dissolved in toluene at a temperature of 9 K. For photopolymerized fullerite (especially above 260 K an absorbed photon can lead to a formation of a covalent bond between neighbouring C_{60} molecules) Kabler and coworkers [11] measured a lifetime of $15\ \mu\text{s}$ at 300 K. In fullerite this excitation is mobile and thus can drift to and onto adsorbed molecules, which has been investigated by Marzok [12], Hoger [13] and Grimmer [14]. Different photon energies were used to

excite fullerite, but no quantitative comparison of the efficacy in the case of time-resolved two-photon photoemission has been published. In the present investigation the pump photon energy is varied by means of a tunable optical parametric amplifier and the efficacy is derived from the results of measurements in the range of 373 to 432 nm (2.87 to 3.33 eV). Lifetimes of excited states are measured by time-resolved two-photon photoemission (2PPE) using an opto-mechanical and an electronic delay.

1.1 Electronic and vibronic states of the Buckminster Fullerene

This is an experimental one, yet some theory is necessary to introduce the common language which describes the electronic states of C_{60} and fullerite. In comparison, many analytical steps can be used to simplify the problem in case of the electronic states of the hydrogen atom so that the final numerical evaluation of energies has a low computational effort and a high accuracy. This is not possible for C_{60} . In this section the approach to the electronic states of C_{60} is based on the Slater determinant [15], which is a well known [16–18] description for a subset of all many-electron wave functions. The Hartree-Fock method allows one to numerically and iteratively evaluate the Slater determinant with the lowest energy, which is an approximation to the electronic ground state. Each molecular orbital (MO) of C_{60} is further approximated by a linear combination of atom centred orbitals (LCAO) and the analytical problem is transferred into a linear algebra equation. Atom centred orbitals for C_{60} are inspired by the hydrogen orbitals and adopt the s, p, or d [19] angular parts and have up to three radial parts [20]. Famous results of LCAO are the sp^2 -hybridisation in graphite and the sp^3 -hybridisation in diamond [21]. The many-electron wave function is approximated by a single Slater determinant [15] of MOs. Starting from pure s and p atomic orbitals the Hartree-Fock method iteratively yields occupied MOs (OMO) which have a Slater determinant with decreasing energy approaching the ground state of the system. From this Slater determinant the energy of the real ground state can be estimated by modifying the Hamilton matrix in the Hartree-Fock equation. For this the local density approximation (LDA) within the Kohn-Sham density functional theory (DFT) defines at each point in space a potential, which is a function of the electron density at that point and in the order of ± 1 eV [22]. This function is optimized to simulate the effect of correlation, which cannot be expressed by the Slater determinant. Often it is used to replace the exchange energy calculation of the Hartree-Fock method, which demands a high computational effort. Gensterblum [22] notes that the results reported in literature for C_{60} mostly agree no matter whether obtained by the Hartree-Fock method without LDA or by LDA without Hartree-Fock exchange energy.

Inserting all ground state OMOs into the (modified) Hartree-Fock equation the unoccupied MOs (UMOs) are given by the eigenvectors of this equation.

Removing one electron from one of the highest 120 occupied MOs, thus creating a hole, and placing the electron into one of the lowest 120 unoccupied MOs [23] generates a singly excited state. The $120 \cdot 120 = 14400$ possible singly excited states are no eigenstates of the symmetry matrices of C_{60} and thus are no eigenvectors of the Hamilton matrix. But linear combinations of singly excited states are eigenstates of the symmetry matrices. For example, the 5-fold degenerate HOMO and the 3-fold degenerate LUMO allow to create 15 singly excited states. Suitable linear combinations lead to a 3-fold (triplet) F_{1g} , a 3-fold (triplet) F_{2g} , a 4-fold G_g and a 5-fold H_g degenerate eigenvector of the symmetry matrices ($3 + 3 + 4 + 5 = 5 \cdot 3$) [24, 25]. Hara and coworkers [26] calculated that the eigenvalues of F_{1g} and the F_{2g} are lower than the eigenvalues of G_g and H_g . In the eigenvectors F_{1g} , F_{2g} , G_g and H_g the electron and the hole are correlated. By definition from Frenkel and Wannier [27, 28] an exciton is a Coulomb-correlated electron-hole pair. Yet this definition is usually [10, 29–31] not used if only free or isolated (in buffer gas, in solution, or matrix isolated) C_{60} is discussed.

The completely filled OMOs have a total spin $S = 0$. With a hole in the shell the spin of the remaining electrons in this shell couples to $S = 1/2$, and this spin is then assigned to the hole. The possible direct product wave functions of two $S = 1/2$ particles (the hole and the electron) are no eigenvectors of the rotation matrices and thus are no eigenvectors of the Hamilton matrix. But suitable linear combination leads to a singlet (S: $S = 0 = 1/2 - 1/2$) state and a triplet (T: $S = 1 = 1/2 + 1/2$) eigenvector ($1 + 3 = 2 \cdot 2$) of the rotation matrices. The triplet state consists of 3 magnetic substates. Furthermore, due to electrons being Fermions the total wave function is antisymmetric. For the symmetric triplet state the wave function in position space is antisymmetric. This wave function has a lower energy (0.4 eV in the calculation of Hara and coworkers, 0.3 eV in experiments on fullerite in the present investigation), because the Coulomb repulsion between the electrons is reduced or in other words the Coulomb attraction between the hole and the electron is increased.

1.1.1 Fullerite

Condensed C_{60} (fullerite) is shown in figure 1.2. The molecular and crystal structure of fullerite was established by X-ray diffraction [22]. The energies of the electronic states shift up to 1 eV as was calculated using LDA [22]. Troullier and Martins [32] used a linear combination of up to 110000 plane waves and Shirley and Louie [33] used a linear combination of 27000 plane waves to express the delocalised electronic states. They applied the so called GW approximation to their 2400 conduction band states (LUMO, LUMO+1) and a not mentioned number of valence band states (HOMO) to calculate the band structure of a free electron or a free hole under the influence of the dynamical screening due to the bound electrons. The results are listed in table 1.1. The valence band and the conduction band are separated

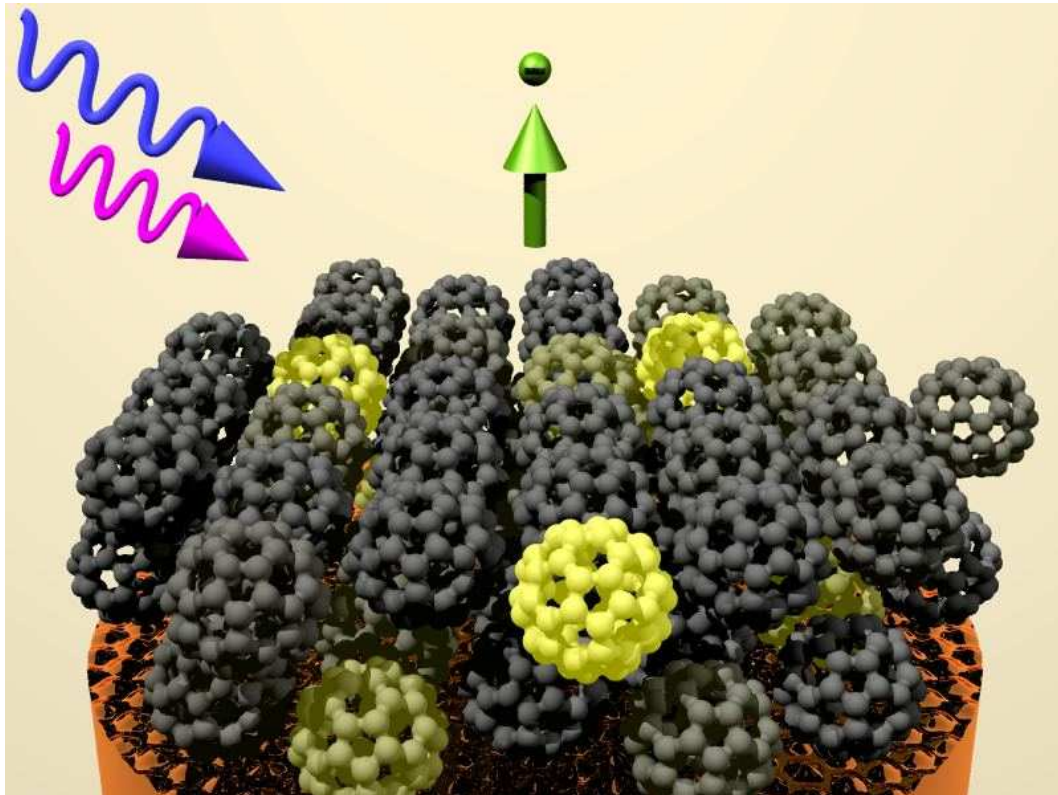


Figure 1.2: Buckminster Fullerene condensed on a copper substrate.

energetically by a gap of 2.5 eV, thus fullerite is a semiconductor and not a metal. Based on this band structure they simulated the effect of disorder in the crystal and extracted hopping integrals [33], but without reporting numbers.

Andersen and coworkers [19] used linear muffin-tin orbitals and estimated [34] the hopping integrals within C_{60} to be 2.59 eV (626 THz) for the single bond and 2.78 eV (672 THz) for the double bond. The hopping integral between two C_{60} molecules for the face-centered cubic (fcc) structure is 0.84 eV (203 THz). From this hopping integrals they calculated the electronic structure for different crystals structures, and Sawatzky and coworkers [25] derived hopping strengths between C_{60} molecules of less than 10 meV (2 THz) for both HOMO (valence band) and LUMO.

In agreement with the theoretical results Gensterblum and coworkers [35] measured a hole bandwidth in the HOMO of 0.4 eV. Smalley and coworkers [36] measured an electron bandwidth in the LUMO of 0.5 eV. Gensterblum and coworkers [37] measured an electron bandwidth in the LUMO of 0.26 eV. In figure 1.3 the impulse averaged energies of these bands are shown on the left.

Based on their GW approximation results Shirley and Louie [54] used linear combinations of singly excited states in fullerite to describe excitons. Their singly excited states were generated by exciting one electron from the HOMO of one molecule, and placing it into the LUMO of the same or a neighbouring molecule. They found an infinite, discrete series of 20 meV wide bands starting from the lowest

1.1 Electronic and vibronic states of the Buckminster Fullerene

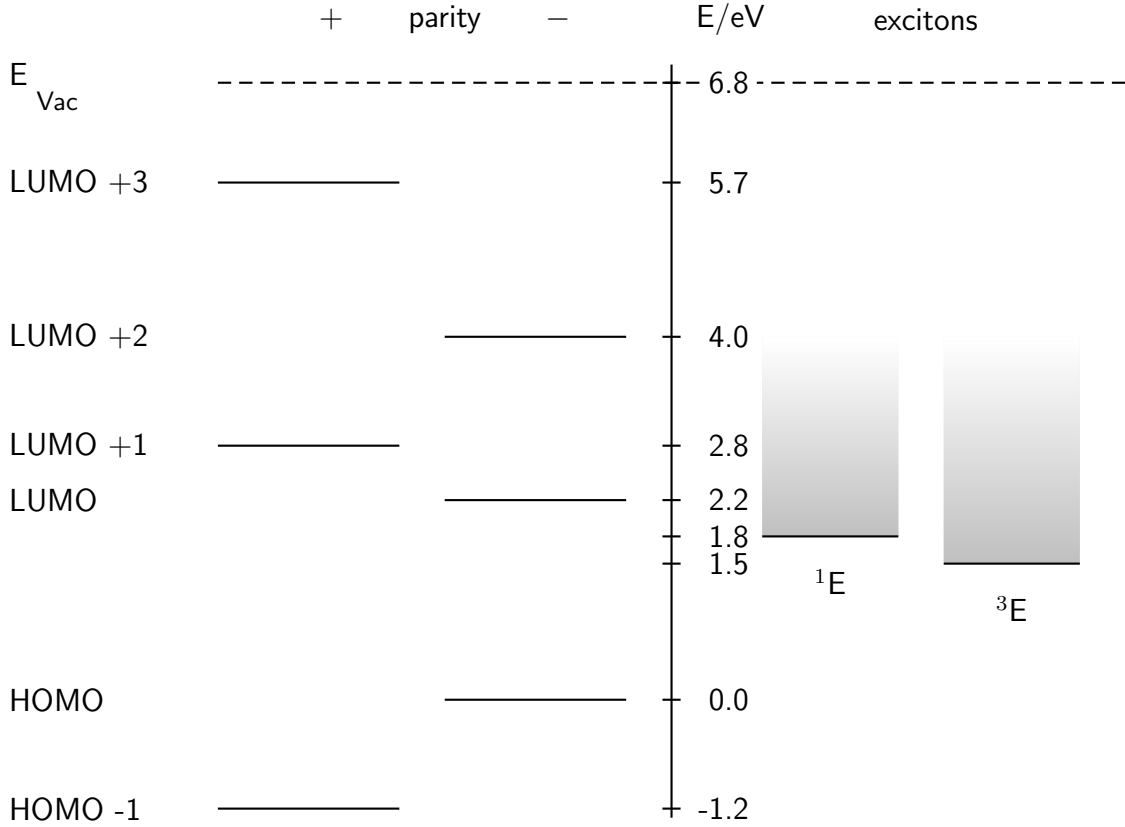


Figure 1.3: Electronic structure of fullerite. 1E =singlet exciton, 3E =triplet exciton. The horizontal lines represent band minima. On the right hand side they also represent metastable excitons. The graded shading represents the higher excitons.

triplet exciton with a band minimum of 1.3 eV [33] (experimental value: 1.4 eV in table 4.1) and ending at the conduction band gap at 2.5 eV [33] (experimental value: 2.3 eV in table 1.1). Excited excitons are typically larger.

From their hopping integrals Sawatzky and coworkers [25,53] derived a bandwidth in the order of 80 meV for the excitons.

The electronic structure resulting from this theory and from experiment is shown in figure 1.3. On the left side energies of the free charge carriers are shown. On the right side the excitons are shown, where the series of bands is indicated by the shaded area. Additionally the vacuum energy E_{Vac} of the fullerite (111) surface is shown. For reference in table 1.1 the individual values reported in the literature are listed and compared to the results of the present investigation.

1.1.2 Influence of nuclear motion

Allowing nuclear motion three effects appear which are important for the present investigation.

In quantum mechanics the nuclei are described by a wave function. The Frank-

1 Introduction

| LUMO lowest triplet singlet exciton | | chemical potential μ | LUMO excited band singlet minimum excitons | | LUMO+1 exciton band centre | | LUMO+2 exciton | method or figure |
|--|--------|--------------------------------|---|--------|----------------------------------|------|-------------------|---------------------|
| | 1.9 | 2.18 | | 2.2 | | 3.0 | 4 | TR2PPE [38] |
| 1.55 | 1.8 | 2.18 | | 2.2 | | 3.0 | | TR2PPE [39] |
| 1.54 | 1.87 | | | 2.0 | | | | TR2PPE [40] |
| | | | | | | 2.87 | 4 | 2PPE [41] |
| 1.55 | 1.8 | | 2.2 | | | | | EELS [31] |
| 1.54 | | | | | | | | EELS [42] |
| | | | 2.1 | | | 2.7 | | AS [43, 44] |
| | 1.83 | | | | | | | SFG [45] |
| | < 1.99 | | | < 2.36 | | | | PC [46] |
| | 1.85 | | | 2.5 | | | | PC [47] |
| 1.6 | | | | 2.25 | | | | PC [48] |
| | | | 2.2 | 2.35 | 2.9 | | | PC, PS [49] |
| | 1.871 | | | | | | | PS [50] |
| 1.50 | | | | | | | | TRPS [51] |
| 1.45 | 1.6 | | | | | | | TRPS [52] |
| | | | | 2.3 | | 4.7 | | UPS, IPE [53] |
| 1.30 | 1.58 | | | 2.5 | | | | theory [33, 54] |

Table 1.1: Energetic positions / eV referenced to the HOMO inferred by different experiments and calculations. 2PPE: two-photon photoemission, TR2PPE: time-resolved 2PPE, EELS: electron energy loss spectroscopy, AS: absorption spectroscopy, SFG: sum frequency generation, PC: photoconductivity, PS: photoluminescence spectroscopy, TRPS: time-resolved PS, UPS: ultraviolet photoelectron spectroscopy, IPE: inverse photoelectron spectroscopy. Additionally, an exciton composed of a hole in the HOMO-1 and an electron in the LUMO is visible in AS at 2.7 eV [44].

Condon principle assumes that at a change of the electronic state the nuclear wave function stays fixed. This is a good approximation because many electronic transitions are faster than many nuclear transitions.

After the electronic transition the forces upon the nuclei do not add up to zero any more, and the nuclei are accelerated. This means an electronic transition in a molecule always excites a vibration. A detailed calculation shows that the electronic transition instantaneously leads to an energy uncertainty of the nuclear wave function. However, this would violate energy conservation and thus it is concluded that the instantaneous transition is only a mathematical tool. In reality all transitions are vibronic. They change the electronic state and the vibrational state. In C_{60} all vibronic transitions which are composed of the same electronic transition span an energy range of about 0.4 eV. The vibrational states are approximately 40 meV apart [55] and are partly resolved in photoemission spectroscopy [22]. In fullerite the vibrational states become phonons, which cannot be resolved in photoemission spectroscopy of fullerite [35, 40].

The HOMO-LUMO transition does not have an electric dipole moment. Due to the Herzberg-Teller effect [56, 57] the HOMO-LUMO transition is still visible

1.1 Electronic and vibronic states of the Buckminster Fullerene

in absorption spectroscopy and one can excite fullerite with readily available radiation with a wavelength of 532 nm (2.33 eV) as is mentioned by Dresselhaus and coworkers [58] and Gensterblum and coworkers [35]. In contrast to fullerite free C_{60} is usually excited by radiation with a wavelength of 355 nm (3.49 eV). The absorption in fullerite may be more effective due to transitions between delocalised states which may have an electric dipole moment if the C_{60} molecules oscillate out of phase [44]. Chergui and coworkers [59] depicted the Herzberg-Teller effect schematically and Hara and coworkers [60] briefly reviewed the mathematical formulation before they applied it to C_{60} : a vibration of the nuclear positions leads to a periodic change of the electronic wave function. The Rayleigh Schrödinger perturbation theory expresses the perturbed wave function in the basis of the unperturbed Hamiltonian. Though this theory is time-independent the mathematical derivation leads to a resonance like denominator:

$$\frac{1}{E_1 - E_0}$$

Here E_0 is the energy of the applied photons and a transition without an electric dipole moment and E_1 is the energy of a transition with an electric dipole. From this it can be concluded that energetically close electronic states exert a stronger perturbation on a vibronic state. Considering an electronic transition in a vibrating molecule, it is a superposition of transitions between all the electronic states which are involved due to the perturbation. Even if the transition between the unperturbed electronic states does not have a dipole moment, the other transitions may do. Although in perturbation theory the perturbation is assumed to be small, Hara and coworkers [60] calculated that in C_{60} the Herzberg-Teller effect leads to an oscillator strength of 0.001484, significantly larger than the multipole moments of the unperturbed electronic transition, which are of the order of 10^{-5} .

The triplet exciton leads to the Jahn-Teller effect. With the triplet exciton one electron is in the 3-fold degenerate LUMO (corresponding to the 3-fold rotational axes in figure 1) and one hole is in the 5-fold degenerate HOMO (corresponding to the 5-fold rotational axes in figure 1). The nuclei move away a bit from the symmetric position because this allows to lower the energy of some of the originally degenerate substates. In a quasi-classical view each molecule undergoes spontaneous symmetry breaking. Two molecules may decide to break the symmetry in different ways and multiple molecules form a statistical ensemble. Looking at the time axis, a single molecule may be excited into the symmetric position and then de-excited into another symmetry breaking position. In the quantum mechanical view an individual molecule is in a superposition of the two degenerate states with the superposition being symmetric again. The lowest triplet state lives long enough for a complete nuclear motion. In fullerite the triplet exciton can only hop to the next molecule if the modified nuclear wave function hops as well. This was introduced by Kuzmany and coworkers [61] mentioned by Wang and coworkers [55] and later verified by Tosatti and coworkers [62]. This reduces the hopping rate and thus reduces the

1 Introduction

chance of the triplet exciton to be lost to the copper substrate [11].

At a temperature of 140 K, at which the the present investigation is performed, the C_{60} molecules rotate around one axis. Neighbouring molecules try to align their rotation axis and orientation to minimize their energy, and cooling below 90 K they completely stop rotating [58].

1.1.3 Dynamics

In this section the dynamics is described which is initiated by absorption of a photon.

Echt and coworkers [29] indirectly excited the lowest singlet state of free C_{60} , which then decays into the lowest triplet state. The lifetime of the lowest triplet state is reduced with increased internal energy. Energy conservation holds and the energy can only be rearranged between different nuclear and electronic degrees of freedom. Still this energy can be interpreted as a mean energy, which allows to assign a temperature [63], which in turn allows the following model: the comparatively slow decay rate of the lowest triplet state and the comparatively fast rates between the excited states leads to a Fermi-Dirac distribution of the population in the excited states. This opens up new decay channels and measurably shortens the lifetime of the triplet states for temperatures above 4 K. The present investigation does also aim at measuring the temperature dependence of a lifetime of a state with a spin triplet.

Isolated C_{60} is in contact to a heat bath and assumes its temperature, thus local energy conservation does not hold. Chergui and coworkers [64] reported that the absorption of a photon with an energy of 3 eV excites C_{60} into an excited singlet state, which decays within 20 ps into the lowest singlet state. This is faster than the laser pulse duration in the current work, and thus only the lowest excited singlet state needs to be considered in figure 1.3. The lowest singlet state cannot decay to the ground state by means of electric dipole radiation, and it is nearly in resonance with a triplet state, into which it can relax by means of spin orbit interaction [65]. Kao and coworkers [66] reported that the singlet state almost exclusively decays into a triplet state. The excited triplet states decay to the lowest triplet state, which in turn decays into the ground state of C_{60} with a very low rate due to the necessary spin flip.

As already discussed in section 1.1.1 in fullerite excited states are not only delocalised over a single molecule, but over multiple molecules forming excitons, which can also be spin singlets or spin triplets. Optical absorption in fullerite is best described by the creation of an exciton. An exciton does have an impulse, but the creating photon delivers only a small impulse and the exciton slows down, so after 1 ps it is certainly in the band minimum [39]. Thus, for the present investigation this band minimum is important as depicted in figure 1.3. The triplet exciton may be trapped at a defect [50] leading to a slightly lower energy.

Eberhardt and coworkers [39] reported that an electron excited from the HOMO

1.1 Electronic and vibronic states of the Buckminster Fullerene

to the LUMO+1 decays into the LUMO with decay time of 1.1 ps. Sawatzky and coworkers [45] noted that the electron in the LUMO+1 belonging to the exciton lies energetically within the band of free electrons in the LUMO and thus in the course of the photo absorption 1% of the excitons dissociate [11, 46]. The precise percentage depends on the temperature and the applied electric field. Eberhardt and coworkers [39] reported that a lifetime of 134 ps can be assigned to the free electrons in the LUMO band. Henninger and coworkers [46] reported that in the ps and ns time regime the number of free electrons decays proportional to $1/t$, with t being the time, which they explained by the spatial distribution of traps and electron hopping. Kabler and coworkers [11] determined a lifetime of 25 ns in photopolymerised fullerite at 81 K. 35% of the singlet excitons decay into the triplet exciton with an intersystem crossing time of 2.5 ns. Eberhardt and coworkers [39] found a singlet exciton lifetime of 998 ps without resolving the decay channels. Kabler and coworkers [11] determined that at fluences higher than 1 mJ/cm^2 triplet exciton creation due to collision between a free carrier and a singlet exciton becomes important. A free carrier colliding with a triplet exciton allows a decay of the triplet exciton into the ground state without a spin flip. The lifetime of the triplet exciton and the influence of the fluence is also investigated in the present investigation.

As mentioned in the last section, in fullerite a strong electron-phonon coupling is present. Chulkov and coworkers [67] calculated the electron-phonon coupling at metal surfaces using the Debye approximation. They used the Fermi-Dirac distribution to express that the system is not in the electronic ground state and they used the Bose-Einstein distribution to express that the vibrational system is not in its ground state. They showed that the temperature dependence of the linewidth in 2PPE experiments (see section 1.2) can be characterized by a single parameter, the electron-phonon coupling constant. Lizzit and coworkers [68] removed the free electrons from this theory and applied it to the temperature dependence of the linewidth of ARUPS of the band-insulator C_{60}K_8 . Their equation reads:

$$\Gamma = \Gamma_0 + \lambda \cdot 2\pi\hbar \int_0^{\omega_D} \left(\frac{\omega}{\omega_D} \right)^2 \left(1 + \frac{2}{e^{\hbar\omega/kT} - 1} \right) d\omega$$

Here Γ is the linewidth, and T is the temperature. These two parameters are used to fit the equation to the experimental results. π , \hbar , e , k are the well known constants, ω_D is the Debye frequency in the original theory. Below 9 K fullerite can be described by the Debye model and the Debye temperature is in the order of 190 K (16 meV, $3.0 \cdot 10^{14} \text{ rad/s}$) [69]. Lizzit and coworkers achieved good results in the range 30 to 700 K by inserting the maximum phonon frequency for fullerite, 200 meV, instead. λ is the hole-phonon coupling constant, which is to be fitted. The measured linewidth increases from 0.57 eV at 40 K to 0.58 eV at 300 K and to 0.66 eV at 600 K. The hole-phonon coupling parameter was fitted to $\lambda = 1.15 \pm 0.05$.

In the present investigation 2PPE spectra are taken in the temperature range from 140 K to 300 K and thus a linewidth change due to electron-phonon coupling

1 Introduction

of about 1 % is expected.

1.1.4 Thin films on Cu(111)

Tsuei and coworkers [70, 71] measured ultraviolet photoemission (UP) spectra of thin fullerite films and observed for the first ML that the states near the Fermi level are highly hybridized between the surface and the molecule. Further MLs show the spectrum of fullerite. In 2004 Louie and coworkers [72] calculated by means of DFT the electron redistribution for the adsorption of a single C₆₀ molecule on Au(111) and on Ag(100). Similarly Wang and Cheng [73] calculated the electron redistribution for the adsorption of one ML on Cu(111). The charge redistribution integrated in planes parallel to the surface is a function of the distance between the chosen plane and the position of the metal nuclei. In all three investigation this function changes its algebraic sign many times. The electric field is related to this distribution by Gauss's law,

$$\nabla \cdot \mathbf{E} = \frac{\rho}{\varepsilon_0} \quad ,$$

where ∇ denotes the divergence, \mathbf{E} is the electric field, ρ is the electric charge density, and ε_0 is the vacuum permittivity. Integration of this field into a potential yields a nearly unchanged work function. Integration of the charge redistribution yields the net charge transfer into C₆₀ as a function of the definition of the precise position of the interface between Cu(111) and C₆₀. The range of values of this integral explains the range of the reported charge transfers which is 0.8 [73] to 2.0 [74] electrons per C₆₀ molecule.

Eberhardt and coworkers [38] observed the LUMO+1, the LUMO and the singlet exciton in a 3 nm thick fullerite film on Ag(100). They determined the lifetime of the LUMO+1 to be 300 ps for a film of 20 nm thickness, 268 ps for 10 nm, 107 fs for 3 nm and 60 fs for 1 nm. Dutton and Zhu [41] showed that the lifetimes of excitations involving the LUMO+2 and LUMO+1 exhibits an exponential dependence on film thickness which is in agreement with charge diffusion into the copper substrate.

Kern and coworkers [75] used a spacer layer of alkanethiol between C₆₀ and gold and silver. By means of surface SHG they showed that down to a distance of 1 nm classic dipole-dipole damping mechanisms prevail and the non-radiative transfer rate decreases with the cube of the distance.

1.2 Electronic states in C₆₀

The electronic structure of C₆₀ is investigated by multiple complementary methods. Table 1.1 compares the energies of the electronic states of fullerite measured by these methods. Methods using either free electrons or free photons or a combination of both are briefly presented here together with their respective main result for

C_{60} . Real measurements take the average over a large number of independent micro experiments: electron and laser beams are assumed to consist of independent electrons and photons, respectively, and single particle detection data are typically averaged. The micro experiment view will be used in the following.

In absorption spectroscopy (AS) a photon flux is applied onto the sample and the transmitted photon flux is detected. To isolate the micro experiments the photon intensity needs to be low enough, on some materials below the intensity of direct sunlight. Due to the measurement process in quantum mechanics repeated micro experiments lead to different results, but the average converges to a well defined absorption coefficient. In this way a transition from an OMO to an UMO is directly visible as absorption as shown by measurements conducted by Eklund and coworkers [44] and listed in table 1.1 under AS.

In photoluminescence spectroscopy (PS) the energy of the emitted photon differs from the energy of the incoming photon. Performing time-resolved PS (TRPS) on a fullerite single crystal Byrne and coworkers [52] found a state with a lifetime of 1.2 ns around 1.6 eV and another state with a lifetime longer than 10 ns around 1.45 eV. In a similar way Chergui and coworkers [76] determined the lifetime of the triplet exciton at 4 K to be 16 μ s in Xe and 60 μ s in Kr. Lee and coworkers [77] determined the lifetime of the triplet exciton at 5 K to be 90 μ s in Xe doped with Ne.

In time-resolved two-photon absorption (TR2PA) a photon flux is applied onto the sample and the transmitted photon flux is detected. The photon intensity needs to be high enough that the so called probe photon has a good chance to hit a point of the sample which has been excited by a so called pump photon. Gruen and coworkers [10] excited the lowest singlet state in isolated C_{60} using 515 nm (2.41 eV) radiation. By measuring the absorption from 400 to 580 nm (from 3.1 to 2.1 eV) they determined a lifetime of 33 ps for the lowest singlet state. The corresponding decay rate matched the formation rate of the lowest triplet state. For isolated C_{60} at room temperature Koishi and coworkers [65] determined the lifetime of the singlet exciton to be 1 ns and they showed that the lowest triplet state is populated by intersystem crossing from the lowest singlet state.

The electron para-electric resonance (EPR) uses photons in the GHz range to probe transitions between the magnetic substates of the triplet exciton. By using an optical pump photon in a time-resolved set-up Gruen et al. [10] measured the lifetime of the lowest triplet state in isolated C_{60} to be 470 μ s at 9 K. Mehring and coworkers [78] measured the lifetime of the lowest triplet state of isolated C_{60} to be 400 μ s at 9 K.

In electron energy loss spectroscopy (EELS) electrons are shot through the sample and their energy loss is detected. The EELS probes similar transitions like absorption spectroscopy, but is not dependent on the dipole matrix element. Using EELS Gensterblum and coworkers [79] measured the energy of the triplet exciton in fullerite to be 1.5 eV.

In sum frequency generation (SFG) two photons are applied onto the sample

1 Introduction

and one photon having the sum frequency is detected. In this way Sawatzky and coworkers [45,80] showed that the energy of the transition into the singlet exciton is resonant to photons with an energy of 1.826 eV (666 nm). Kern and coworkers [75] generated an exciton population by means of pulses with 3.49 eV photon energy (355 nm). Their probe pulses had a photon energy of 1.17 eV (1060 nm) and generated a surface second harmonic in the centrosymmetric fullerite. The photon energy of 1.17 eV is resonant to transitions between the lowest excited singlet exciton and a higher excited singlet exciton. Thus, the exciton population could be probed by absorption and a lifetime of 560 ps for the singlet exciton was observed.

Applying a photon to the sample can lead to the desorption of an absorbed molecule, which is then detected. In this respect, our group [13,81] investigated the desorption of NO molecules from fullerite. The set-up allows to separate directly desorbing molecules from molecules desorbing due to energy transfer from the triplet exciton.

Absorption can create electron-hole pairs in semiconductors, which can lead to photocurrent (PC) as explained in section 1.1.3. Photocurrent can discharge the surface dipole of C_{60} which is visible in surface photovoltage spectroscopy [82]. In this way Shapira and coworkers [48] detected occupied and unoccupied localized states within the conduction band gap which they assumed are due to defects. With increasing temperature the number of electrons and holes increases and leads to a reduced resistance. From the resulting curve a conduction band gap of 1.85 eV was deduced [83].

1.2.1 Photoemission

In photoemission one photon is applied onto the sample and an emitted electron can be detected [84–86]. For the interpretation of PE experiments on condensed matter the three-step model by Berglund and Spicer [87,88] has proven to be useful. Step 1 is the absorption of a photon and the excitation of an electron. In the present investigation final states for the electron with an energy ranging from 1.4 to 5.4 eV above the vacuum energy are populated. In this case fullerite offers a high and relatively constant density of states, see also figure 1.6. Step 2 is the propagation of conduction electrons in fullerite, which has already been introduced in section 1.1.1. Half of the electrons propagate towards the surface. On the way to the surface some electrons are inelastically scattered and lead to a background signal in the measurement. Shirley [89] described the background simply as an indefinite integral of the spectrum, integrating from high to low energies. This scattering makes photoemission a surface sensitive technique. For example after absorption of 5 ML C_{60} no photoelectrons originating from the copper can be detected as can be seen in figure 2.7.

Step 3 is the transmission of an electron across a surface into the vacuum. The surface is assumed to be planar, thus the electron in the vacuum is best described by

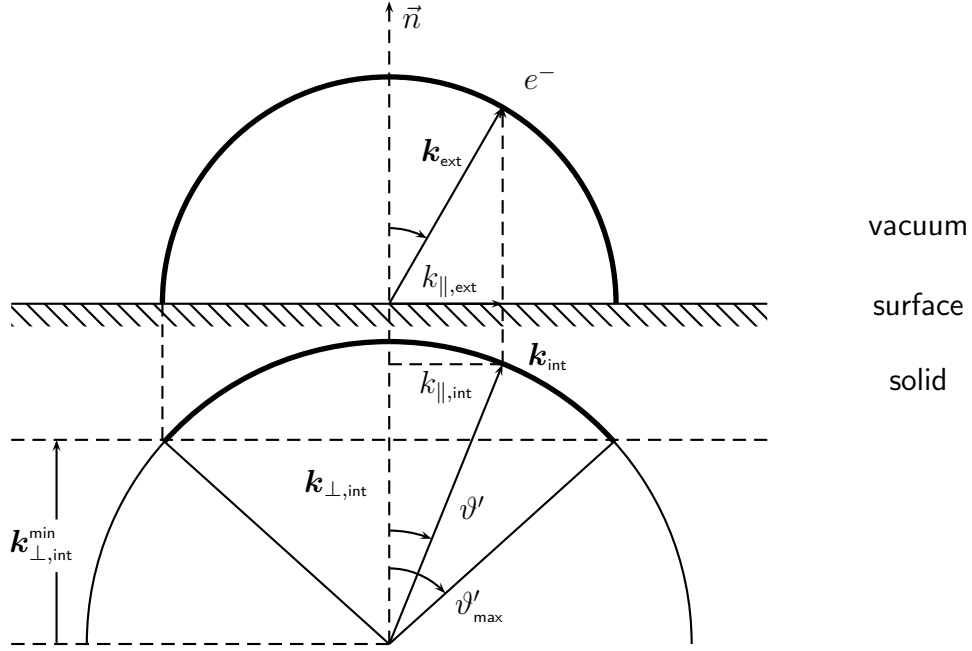


Figure 1.4: The third step of the three-step model explicitly features the impulse within the solid (after Courths and Hüfner [88]). Note that this figure contains two axes in k -space, which are shifted with respect to each other to denote the impulse of the electron inside the solid and outside of the solid.

plane waves which are infinite in space as requested for the general photoemission and whose wave vector is proportional to the impulse of the electron. Only such electrons which have an energy higher than the work function Φ can leave the solid. In fullerite any energy is referenced relative to the HOMO and $E_{\text{vac}} = \Phi + \mu$. The energy centred view is supplemented by an impulse centred view in figure 1.4. The impulse parallel to the surface is conserved. Only electrons whose momentum perpendicular to the surface $k_{\text{int},\perp}$ is larger than

$$\frac{\hbar^2 k_{\text{int},\perp}^2}{2m_e} > \Phi,$$

are emitted.

Parallel to the surface the momentum is conserved $\mathbf{p}_{\parallel} = \hbar \mathbf{k}_{\text{ext},\parallel}$ up to a reciprocal lattice vector

$$\mathbf{k}_{\text{ext},\parallel} = \mathbf{k}_{\text{int},\parallel} + \mathbf{G}_{\parallel} \quad .$$

From the minimum of the perpendicular component of \mathbf{k}_{int} and from

$$\hbar^2 k_{\text{int}}^2 = \hbar^2 k_{\text{int},\perp}^2 + \hbar^2 k_{\text{int},\parallel}^2 = 2m_e E_f$$

1 Introduction

follows a maximum of the component parallel to the surface

$$k_{\text{int},\parallel}^{\text{max}} = \sqrt{\frac{2m_e}{\hbar^2}(E_f - \Phi)} \quad .$$

This corresponds to electrons emitted perpendicular to the surface. In vacuum

$$\hbar^2 k_{\text{ext}}^2 = 2m_e E_{\text{kin}} = \hbar^2 k_{\text{ext},\perp}^2 + \hbar^2 k_{\text{ext},\parallel}^2$$

holds, where E_{kin} is the kinetic energy of the emitted photoelectrons. These electrons are transmitted through the surface if

$$k_{\text{ext},\perp}^2 = \frac{2m_e}{\hbar^2} E_{\text{kin}} - (\mathbf{k}_{\text{int},\parallel}^2 + \mathbf{G}_{\parallel})$$

is greater than zero. In other words, only electrons which have an impulse \mathbf{k}_{int} within the cone with an opening angle of $2\vartheta'_{\text{max}}$ can be emitted.

1.2.2 Time-resolved 2PPE from \mathbf{C}_{60}

In two-photon photoemission (2PPE) two photons are applied and the emitted photoelectron is detected. The electron emission and detection is practically identical to one-photon photoemission, the remainder of this section discusses the absorption of two photons in step 1 of the three step model. The discussion is based on simple model systems. In the present investigation time-resolved 2PPE (TR2PPE) is employed, where the two photons belong to different laser pulses with a time delay in between.

1.2.2.1 Two-photon absorption

The absorption of two photons is described by the following two models. Göppert-Mayer [90] deduced two-photon absorption from linearly perturbed matter and quantum cavity electrodynamics. She showed that absorption can occur via intermediate electronic states as long as the sum of the photon energies is equal to the transition from the initial to the final state. The intermediate electronic states are all other eigenstates of the unperturbed Hamiltonian of the matter. If the transition from the initial state to the intermediate state is close to resonance with the applied photon energy, the two-photon absorption is very efficient. For a semiconductor all the states in the valence and the conduction band contribute to the two-photon absorption from the valence band maximum to the conduction band minimum. This process is still efficient enough for technical applications in short pulse lasers. Van Stryland and coworkers [91] showed that two-photon absorption is related to the nonlinear Kerr effect by the Kramers-Kronig relation. The Kerr effect is described by a macroscopic nonlinear relation between the classical electric field strength and the classical mean polarization of the matter. The same explanation is used for

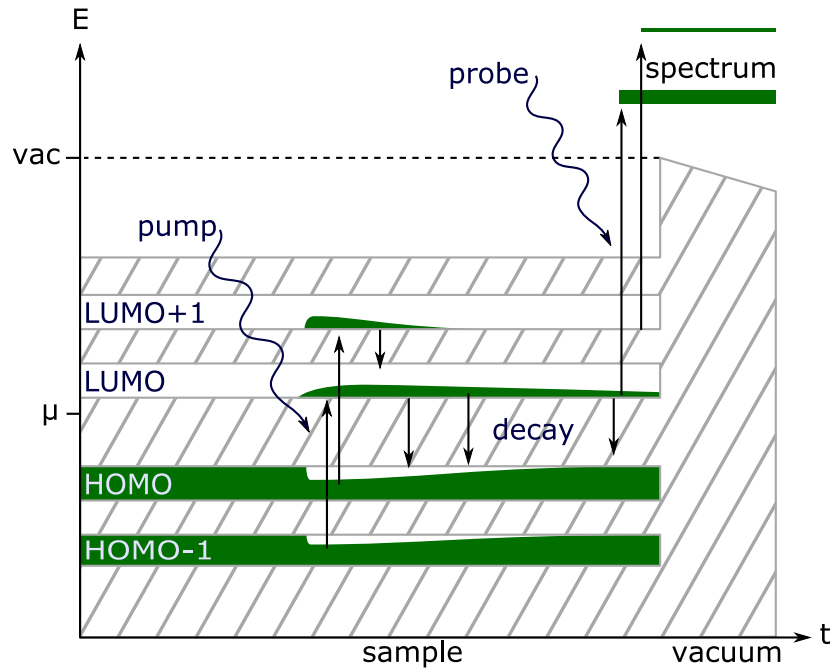


Figure 1.5: Rate equation governed time-resolved 2PPE of a semiconductor.

second harmonic generation by Franken and coworkers [92], and in its original linear relation it describes the refractive index. It is explained by the deformation of the electron cloud around each atom and thus only uses the ground state of the atom which is in contrast to the approach taken by Göppert-Mayer. In 1961 Kaiser and Garrett [93] performed the first two-photon absorption experiment.

1.2.2.2 Two-photon absorption in a statistical ensemble

Up to now the theoretical description was based on ideal systems, which are basically described by the Schrödinger equation, and where the perturbation by the light can be calculated in the Dirac picture. In the experiment a decay of excited states is observed, while the Schrödinger equation predicts excited states with infinite lifetime. To resolve this paradox, Ueba [94] applied the density matrix, which was introduced by von Neumann and coworkers [95], to two-photon photoemission. Von Neumann and coworkers showed that the dynamics of the density matrix can be calculated in the Heisenberg picture of quantum mechanics. Formally the resulting equation allows to add decay and dephasing terms, which are then used to fit the theoretical results to the experimental results. If the laser pulse duration is significantly longer than the dephasing time, the state of the system can be approximated by populations and the dynamics is described by a rate equation [96,97] as depicted in figure 1.5.

1.2.2.3 Simulation: Solving the rate equations

Following Ueba and Mii [94] and section 1.2.2.1, the 2PPE is based on a 3-level system consisting of an initial occupied (Ψ_0), an intermediate unoccupied (Ψ_1) and a final photoelectron state (Ψ_2). In the present investigation the Ψ s are populations. The dynamics is expressed as a system of equations:

$$\begin{aligned}\frac{d}{dt}\Psi_0(t) &= r_{0,0}(t)\Psi_0(t) + r_{0,1}(t)\Psi_1(t) + r_{0,2}(t)\Psi_2(t) \\ \frac{d}{dt}\Psi_1(t) &= r_{1,0}(t)\Psi_0(t) + r_{1,1}(t)\Psi_1(t) + r_{1,2}(t)\Psi_2(t) \\ \frac{d}{dt}\Psi_2(t) &= r_{2,0}(t)\Psi_0(t) + r_{2,1}(t)\Psi_1(t) + r_{2,2}(t)\Psi_2(t)\end{aligned}\quad (1.1)$$

Here r are the rates between the states.

For a weak pump pulse the occupied state can be assumed not to deplete, and for a weak probe pulse the influence on all states but $\Psi_2(t)$ can be ignored, leading to

$$\begin{aligned}\frac{d}{dt}\Psi_0(t) &= 0 \\ \frac{d}{dt}\Psi_1(t) &= r_{1,0}(t)\Psi_0(t) + r_{1,1}\Psi_1(t) \\ \frac{d}{dt}\Psi_2(t) &= r_{2,1}(t)\Psi_1(t)\end{aligned}\quad ,$$

where $r_{1,0}(1)$ is the pump rate, $r_{1,1}$ is the decay rate, and $r_{2,1}(t)$ is the probe rate. This system of equations can be solved in the order: Ψ_0 , Ψ_1 , Ψ_2 . The first equation expresses the non-depleting occupied state. Before solving Ψ_1 some abbreviations are introduced — $r_{1,0}(t)\Psi_0 = S(t)$ (source), $\Psi_1(t) = \Psi$, $r_{1,1} = R$ (rate) — , yielding

$$\dot{\Psi}(t) - R\Psi = S(t) \quad . \quad (1.2)$$

In the frequency domain the population is defined as ¹

$$\Psi(t) = \int_{-\infty}^{+\infty} \Psi(\omega)e^{i\omega t}d\omega \quad . \quad (1.3)$$

Equation 1.3 is applied to equation 1.2. For the first part this means that

$$\dot{\Psi}(t) = \frac{d}{dt} \int_{-\infty}^{+\infty} \Psi(\omega)e^{i\omega t}d\omega = \int_{-\infty}^{+\infty} \Psi(\omega)(i\omega) \cdot e^{i\omega t}d\omega \quad .$$

¹Since in the current section all functions in the time domain always have their parameter, time (t), explicitly written out and all functions in the frequency domain have the parameter, angular frequency (ω), explicitly written out, the more proper designation by an additional index is omitted.

Furthermore, substituting

$$S(t) = \int_{-\infty}^{+\infty} S(\omega) e^{i\omega t} d\omega$$

in equation 1.2 leads to

$$\int_{-\infty}^{+\infty} \Psi(\omega)(i\omega) e^{i\omega t} d\omega - R \int_{-\infty}^{+\infty} \Psi(\omega) e^{i\omega t} d\omega = \int_{-\infty}^{+\infty} S(\omega) e^{i\omega t} d\omega \quad .$$

This equation holds true if the integrands are already equal, thus transforming the whole equation into the frequency domain:

$$\Psi(\omega)(i\omega) - R\Psi(\omega) = S(\omega)$$

Isolating the wave function yields

$$\Psi(\omega) = \frac{S(\omega)}{i\omega - R} \quad .$$

This can also be read as a matrix equation in order to include multiple states like the LUMO and the LUMO+1 in C_{60} .

Ψ_2 is solved by integration,

$$\Psi_2(t) = \int R_{2,1}(t) \Psi_1(t) dt \quad .$$

The experimental set-up measures approximately $I = \Psi_2(+\infty)$, employs probe laser pulses $R_{2,1}(t) = P_1(t - t_1)$ with a fixed shape, which are delayed by t_1 relative to the time basis. Then this delay is varied in a series of measurements. In the calculation for each delay the already numerically evaluated $\Psi_1(\omega)$ and $\Psi_1(t)$ are reused.

$$I(t_1) = \int_{-\infty}^{+\infty} P_1(t - t_1) \Psi_1(t) dt$$

Applying the convolution theorem yields

$$I(\omega_1) = 2\pi P_1(\omega_1) \Psi_1(\omega_1) \quad . \quad (1.4)$$

In the present investigation a laser pulse can well be modelled as a Gaussian pulse,

$$P(t_2) = P_A e^{-\left(\frac{t_2}{w}\right)^2} \quad ,$$

1 Introduction

which is transformed into

$$P(\omega_2) = \frac{1}{2\pi} \int_{-\infty}^{+\infty} P(t_2) e^{-i\omega_2 t_2} dt_2 = P_A \frac{w}{\sqrt{2}} e^{-\left(\frac{w\omega_2}{4}\right)^2} .$$

Substituting the factors on the right hand side of equation 1.4 for their definitions,

$$I(\omega_1) = 2\pi P_{1,A} \frac{w_1}{\sqrt{2}} e^{-\left(\frac{w_1\omega_2}{4}\right)^2} \frac{S(\omega)}{i\omega - R} ,$$

substituting S for its definition,

$$= 2\pi P_{1,A} \frac{w_1}{\sqrt{2}} e^{-\left(\frac{w_1\omega_2}{4}\right)^2} \frac{R_{1,0}(\omega)\Psi_0}{i\omega - R} ,$$

substituting $R_{1,0}$ for a Gaussian,

$$= 2\pi P_{1,A} \frac{w_1}{\sqrt{2}} e^{-\left(\frac{w_1\omega_2}{4}\right)^2} P_{0,A} \frac{w_0}{\sqrt{2}} e^{-\left(\frac{w_0\omega_2}{4}\right)^2} \frac{\Psi_0}{i\omega - R} ,$$

and regrouping yields

$$I(\omega_1) = \pi P_{0,A} P_{1,A} w_0 w_1 \Psi_0 e^{-(w_0^2 + w_1^2)\left(\frac{\omega_2}{4}\right)^2} \frac{1}{i\omega - R} .$$

To reduce the time needed for numerical evaluation within Matlab to an acceptable level the frequency has to be rounded to 1 MHz — equivalent to 1/20000 of the fitted laser bandwidth of around 20 GHz — and only frequencies up to 5 times the laser bandwidth can be included, thus yielding a Fourier series:

$$I(t_1) = 10^5 \pi P_{0,A} P_{1,A} w_0 w_1 \Psi_0 \cdot \sum_{f=-10^5}^{10^5} e^{-(w_0^2 + w_1^2)\left(\frac{2\pi}{4\text{MHz}}f\right)^2} \frac{1}{i\frac{2\pi}{\text{MHz}}f - R} e^{i\frac{2\pi}{\text{MHz}}ft} . \quad (1.5)$$

Here f is an integer to help sum over the frequencies. For lifetimes above 7 ns the repetitive nature of the Fourier series produces a positive baseline in front of the laser pulse. This would be realistic for an experiment with a laser repetition rate which equals the above mentioned 1 MHz. Since in the present investigation the laser has a repetition rate of 1 kHz, ideally the same rounding needs to be employed in theory. Pragmatically a rounding precision above 1 kHz is sufficient if the baseline is below 1% of the signal peak.

The resulting $I(t_1)$ can be plotted as continuous curves like in figure 3.15 (blue and green curve) and the rates are fitted to the measured data which are plotted as symbols. Later in section 2.3.4.5 the derivative of equation 1.5 with respect to its parameters is useful.

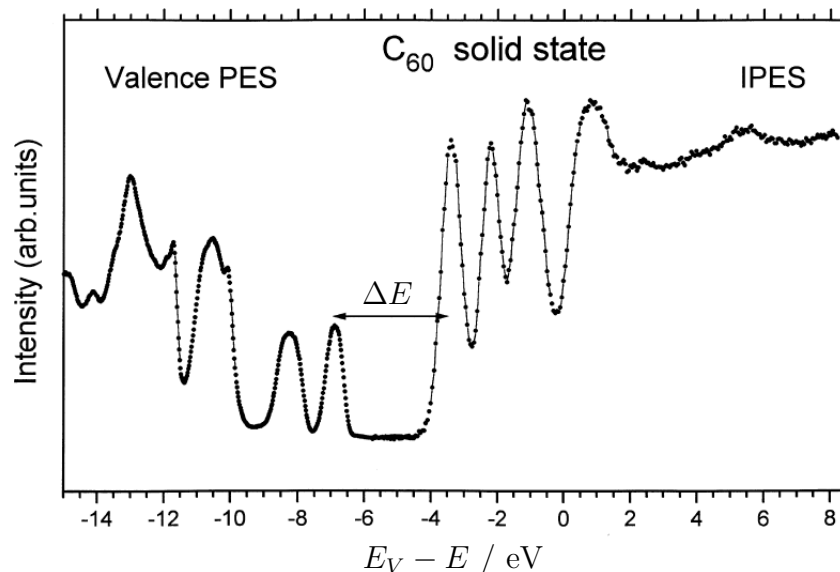


Figure 1.6: Combination of photoelectron spectroscopy of the valence bands (21.2 eV) and inverse photoelectron spectroscopy at $C_{60}/Au(110)$. E_v = vacuum level, ΔE = HOMO-peak to LUMO-peak distance, adapted from [31].

1.2.3 Inverse photoemission in combination with UPS

In inverse photoemission electrons are injected into the sample and photons are detected. A combination of both inverse and direct photoemission was used by Rudolf and coworkers [31] to present the occupied and unoccupied states of fullerite together, as shown in figure 1.6. They stressed that ΔE is not the conduction band gap. Sawatzky and coworkers [53] acknowledged that it is rather the energy needed for a transition from the middle of the valence band to the middle of the conduction band. For the conduction band gap the high energy onset of the HOMO and the low energy onset of the LUMO have to be used. Additionally these onsets correspond to the smallest energy lost to vibrations or other parasitic excitations. They presented experimental spectra which merged into the noise level within 100 meV, and thus measured an energy difference with an uncertainty of about 144 meV. Then they simply subtracted the experimental energy resolution from this value to obtain a realistic conduction band gap of 2.3 eV. To reduce the energy uncertainty Kabler and coworkers [11] used a model theory, which they fitted to the whole lineshape.

1.2.4 Electrostatic effects

The elementary photoemission process creates a hole. In the case of a metallic sample the hole is distributed across the whole macroscopic sample and is then neutralized by the connection to electrical ground. In the present investigation a thin film of fullerite is condensed onto a copper substrate. A hole in the fullerite film needs some time to drift to the copper, and for multiple emission events the holes can accumulate. Similarly, in any photoemission experiment there can be a large

1 Introduction

number of electrons in the vacuum. All these charge carriers interact electrostatically leading to artefacts in the spectrum: the spectrum changes with fluence, the effective extraction voltage is reduced and the spectrum shifts towards lower energies. None of the effects mentioned above has been observed in the present investigation, which uses single electron detection and thus naturally has a very low density of electrons in the vacuum.

One result of the GW approximation is that the polarisability of the environment has a strong influence on the energy needed to dissociate an electron-hole pair. This energy is called the Hubbard U which is taken from the Hubbard model [98], where it originally denotes the Coulomb energy of two electrons being on the same ion [99] within a crystal. In the metal substrate the Hubbard model does not really apply ($U = 0.0$ eV). The Hubbard U of fullerite can be estimated to $U = 0.8$ eV from the conduction band gap and the lowest exciton energy. Zhu and coworkers [74] showed that going from 20 to 2 ML fullerite on Cu(111) U decreases to 0.3 eV, which is in agreement with figure 2.7. In the surface layer U is 1.0 eV [40, 100]. For a free C_{60} the Hubbard energy is $U = 3.0$ eV [31].

If an electron-hole pair is separated in such a way that the hole moves into the metal and the electron moves into the fullerite an energy of $U = 0.8/2 = 0.4$ eV is needed. The chemical potential of Cu(111) appears 2.1 eV above the HOMO (figure 2.7) and does not shift with the adsorption of fullerite. With the above mentioned correction the chemical potential is placed 1.7 eV above HOMO. This is above the middle of the conduction band gap and above the triplet exciton. Thus, the triplet exciton may be obscured by gap states due to defects. Since the fullerite is undoped and the conduction band gap is much larger than kT , with k being the Boltzmann constant and T being the temperature, the positions of the HOMO and the LUMO bands shift antisymmetric around the chemical potential with film thickness and are determined by the interface only.

With PES the HOMO band can be probed. As already mentioned in 1.1.3 in fullerite the absorption of a photon most of the time does not generate free charge carriers and other effects obscure the conduction band gap in 2PPE, EELS, or AS [41]. As pointed out by Sawatzky and coworkers [83] and Kabler and coworkers [40] the conduction band gap is given by the onset of the PE spectra and the IPE spectra, because the conduction electrons and holes have energies as close as possible to the band gap.

In PES the LUMO band needs to appear above the chemical potential, otherwise it would be populated in equilibrium. In figure 2.7 the chemical potential does not shift with the adsorption of fullerite. PES out of the metal substrate leaves behind a hole with an energy of 0.0 eV. PES out of the HOMO or one of the excitons leaves behind a hole 2.0 eV below the chemical potential. This energy is lost for the kinetic energy of the emitted electron.

X-rays can be used to excite an electron out of a 1s core state of the carbon atom leaving behind a hole. In X-ray photoelectron spectroscopy (XPS) the electron

is then emitted into the vacuum. In X-ray fluorescence a second electron falls from a HOMO into the hole and the energy is used to emit an X-ray fluorescence photon. In a competing decay channel, the Auger process, electrostatic interaction between the electrons transfers the energy to a third electron in the HOMO, which is then emitted. Brühwiler and coworkers [31] showed that the resulting spectrum is well approximated by a self-convoluted PE spectrum shifted to lower energies by a Hubbard U of 1.4 eV. The convolution is based on the following observation: in the final state of the Auger process two holes are in the OMOs both reducing the energy which is available for the emitted electron. The convolution then iterates through all possible combinations of OMOs. The electric field to the one hole in the $1s$ orbital shifts all states to lower energies by U .

In a near edge X-ray absorption fine structure (NEXAFS) measurement the electron is excited to the various LUMOs. In this way the absorption spectrum depicts the LUMOs. The LUMOs are inside the electric field generated by the core hole and may be distorted. In autoionisation an electron falls out of a HOMO into this hole and the energy is used in the participator process to emit the first electron from the LUMO and in the spectator process to emit a third electron from the HOMO. By comparing autoionisation with Auger spectroscopy Sawatzky and coworkers [53] determined the Hubbard energy U to be 1.6 eV. The participator process leaves a hole in the HOMOs behind and, even though the process is very complex, in the end the spectrum of direct photoemission out of the HOMO is reproduced. In this way Brühwiler and coworkers [101] showed that only the electronic structure of the first ML of fullerite on Au(111) is changed from the bulk structure.

In fullerite the electron in the LUMO can hop to another molecule. After hopping a spectrum similar to the photoemission experiment on a C_{60}^+ ion is generated. The fullerite spectrum is a superposition of two replica of the spectrum of isolated C_{60} shifted by U with respect to each other. The weighting of the two replica multiplied with the core hole lifetime gives the hopping rate. Using this method, Rudolf and coworkers [102] showed that the hopping rate for an electron in the LUMO+1 is roughly equal to the core decay rate of $1.7 \cdot 10^{14}$ Hz (6 fs) in the presence of a C $1s$ hole, which is in rough agreement with the theoretical hopping rates in section 1.1.1.

1 Introduction

2 Experiment

This experiment needs an atomically clean surface. This requires ultra high vacuum (UHV) of about 10 nPa (10^{-10} mbar) or lower.

The chamber (see figure 2.1) is fitted with optical viewports, electrical feedthroughs and manipulation devices, which are designed to enable precise relative motion via edge welded bellows. The vacuum is established by two turbomolecular pumps (Pfeiffer TPU 180H, H_2 pressure ratio: 10^6), which are backed by a two-stage rotary vane pump (Leybold Trivac D8B, pumping speed: $8\text{m}^3/\text{h}$). A detailed description of the vacuum chamber has been given by Jabs [103] and Göhler [104].

2.1 Sample preparation

A copper single crystal cylinder with 5 mm radius and 2 mm thickness is mounted in the middle of the chamber. The Cu(111) surface has been polished to optical quality and then introduced into the chamber where it is sputter annealed.

In figure 2.2 an angle resolved UP spectrum (ARUPS) of Cu(111) taken with a photon energy of 8.24 eV is shown. The Shockley surface state is quite intense compared to UP spectra taken with 21 eV [71].

As shown in figure 2.3, the C_{60} monolayers are prepared by vapour deposition. A crucible is heated to 700 K by 400 to 420 eV electron bombardment. The crucible contains C_{60} powder (99.9%+ purity; Proteomics GmbH, Frankfurt; Alfa Aesar, USA), and the C_{60} vapour pressure is 3.6 mPa at a temperature of 700 K following the vapour pressure equation [105, 106]:

$$\log(p/\text{Pa}) = 23.23 - 20193/(T/\text{K}) \quad ^1$$

The electron beam evaporator is fabricated close to a commercial design. As the vapour leaves the crucible it is partially ionised by the incoming electron beam. Some of the ions will be collected by the flux monitor electrode, generating a small positive current which is related in magnitude to the vapour flux.

The crucible is outgassed at 430 K for two days together with the chamber to remove any solvents, then the heating voltage is calibrated to condense one ML every 300 s onto the sample (see section 2.1.1), which is comparable to one ML every 600 s at 373 K used by Koma and coworkers [107]). A quadrupole mass spectrometer measures the evaporating CO, when the CO concentration has been below other

¹The present work uses e as the basis for \log .

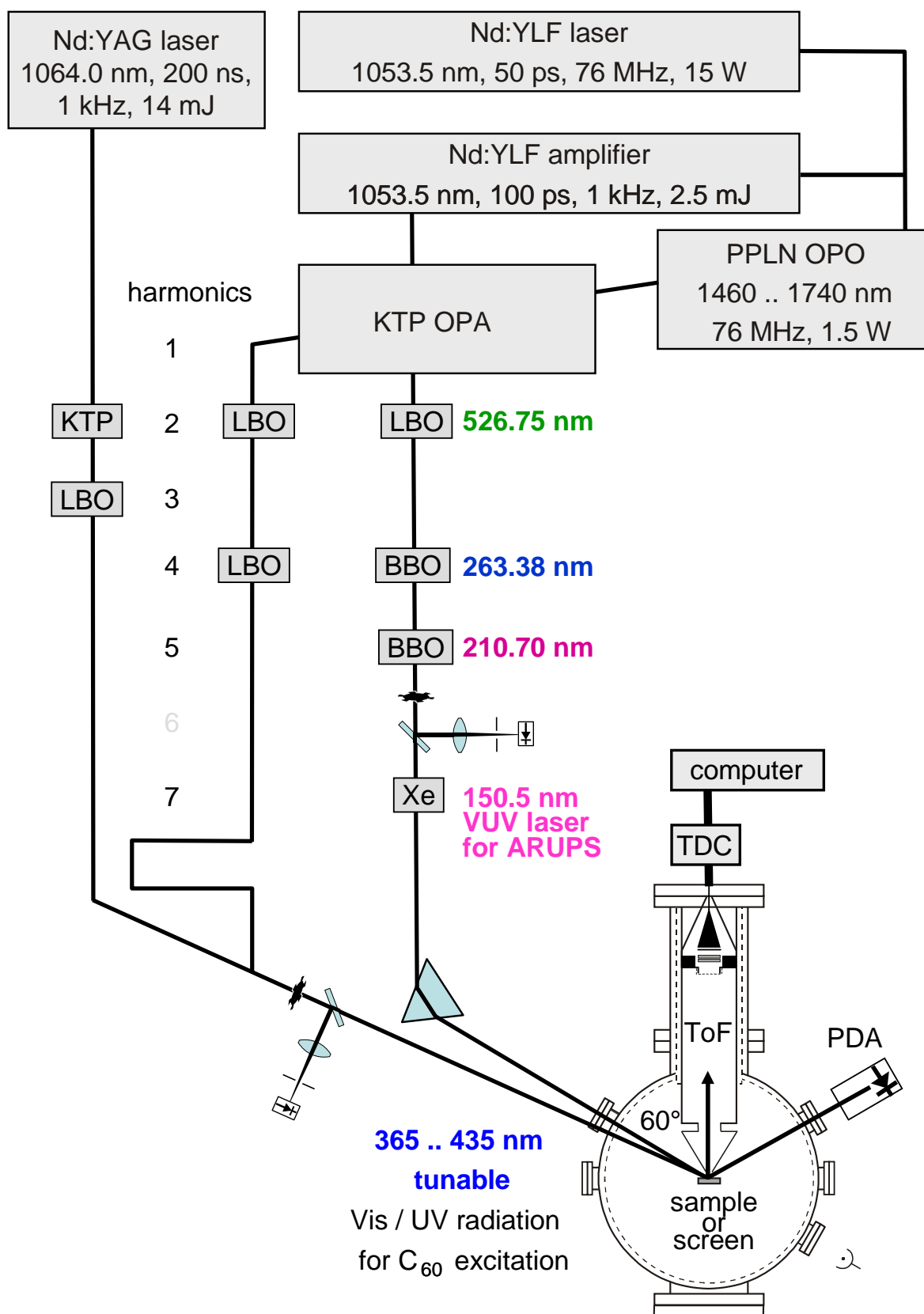


Figure 2.1: The lower part of the UHV chamber and a schematic layout of the laser system.

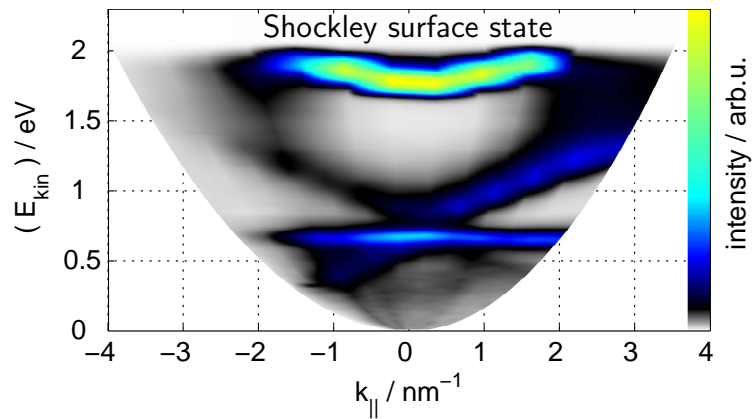


Figure 2.2: ARUPS on Cu(111).

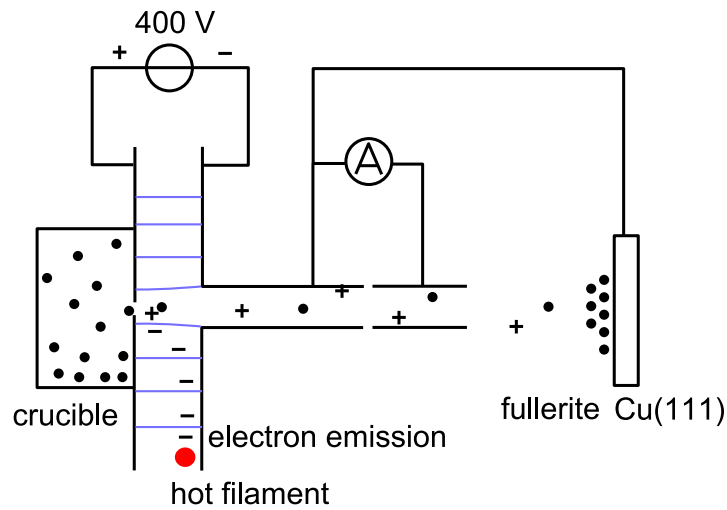


Figure 2.3: The design of the evaporation does not in principle prevent ions being generated near the crucible and accelerated to 400 eV from hitting the film. The light blue lines are field lines.

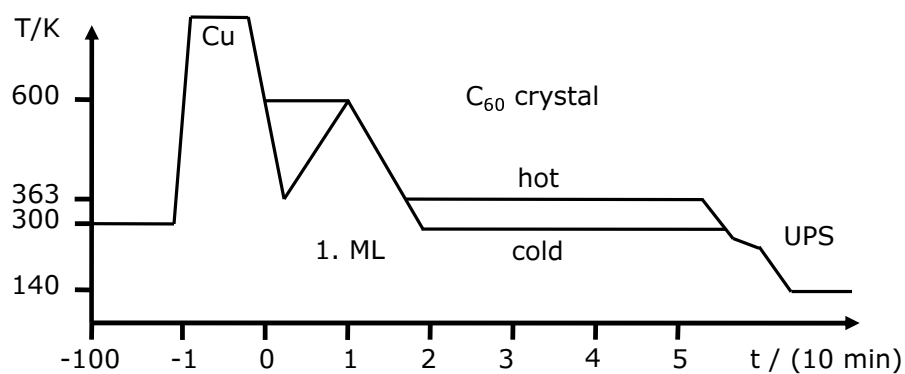


Figure 2.4: Temperature of the copper substrate as a function of time.

2 Experiment

residual gases in the chamber for 2 hours, the sample is placed in front of the evaporator, flashed to a temperature of 1000 K, and cooled down to 600 K as shown in figure 2.4.

Repp and coworkers [108] showed that on Cu(111) at a temperature of 5 K C_{60} chemisorbs with a six-membered ring parallel to the surface at two different binding sites. Two C_{60} molecules adsorbed at these different sites are rotated by 60° with respect to each other. Above 100 K C_{60} forms islands and decorates step edges on Cu(111) [108, 109]. Tang and coworkers [110] showed that the 4x4 super structure created by annealing at higher temperatures than 300 K generates new step edges in the Cu(111) substrate. As shown in figure 2.5 the UPS of one ML fullerite adsorbed at 300 K changes after annealing to 600 K.

Both spectra are in agreement with a calculation by Wang and Cheng [73] for the (4x4) superstructure. In agreement with Tsuei and coworkers [70, 71] the Shockley surface state shows dispersion, but in the present investigation appears enhanced compared to the Cu 3d bands at lower energies, which might be due to the different probe photon energies. In both measurements the structures around 1 eV are enhanced by annealing and are only visible in normal emission.

In the present investigation the first ML grows in the 4x4 super structure and thus exhibits domains, which have about 30 nm lateral extent on copper [11]. This extent may be determined by the residual 4% lattice mismatch and not by the mobility of the C_{60} molecules. The domain boundaries contain defects, so called X-traps [111]. Therefore, Eklund, Dresselhaus and coworkers [44] compared their measurement on thin films with measurement on single crystals by Guss and coworkers [50]. Other defects may be due to impurities like metal atoms or higher Fullerenes. Due to the higher Hubbard U on the surface the excitons would be pushed into the bulk if it was not for surface state like defects. Optionally, the temperature is then reduced from 600 K to 360 K in order to allow molecules to land on the first ML and diffuse to vacancies and increased back to 600 K to anneal the ML and desorb residual gas. The temperature is reduced to 360 K, which will be called “warm” in the following. Fartash [112] found that with a grow rate of one ML every 20s the quality of the film increases as the temperature was increased from 393 K to 548 K and observed that the flux out of the crucible decreased due to powder deterioration (possibly a reduction of the internal surface). Up to 20 MLs are adsorbed onto the substrate. To prevent photopolymerization all viewports are blocked and all internal light sources are turned off.

Eventually the temperature is reduced. At 260 K fullerite undergoes a phase transition which needs to be passed at a speed of less than $1 K/60 s$ to relax stress in the fullerite. Finally the sample is cooled down to 140 K for the measurement to reduce photopolymerization.

Alternatively, evaporating the MLs onto a cold substrate with a temperature of 300 K leads to clearly different results which are presented in section 3.4.

When not used, the fullerite in the crucible is protected by a shutter from the hard

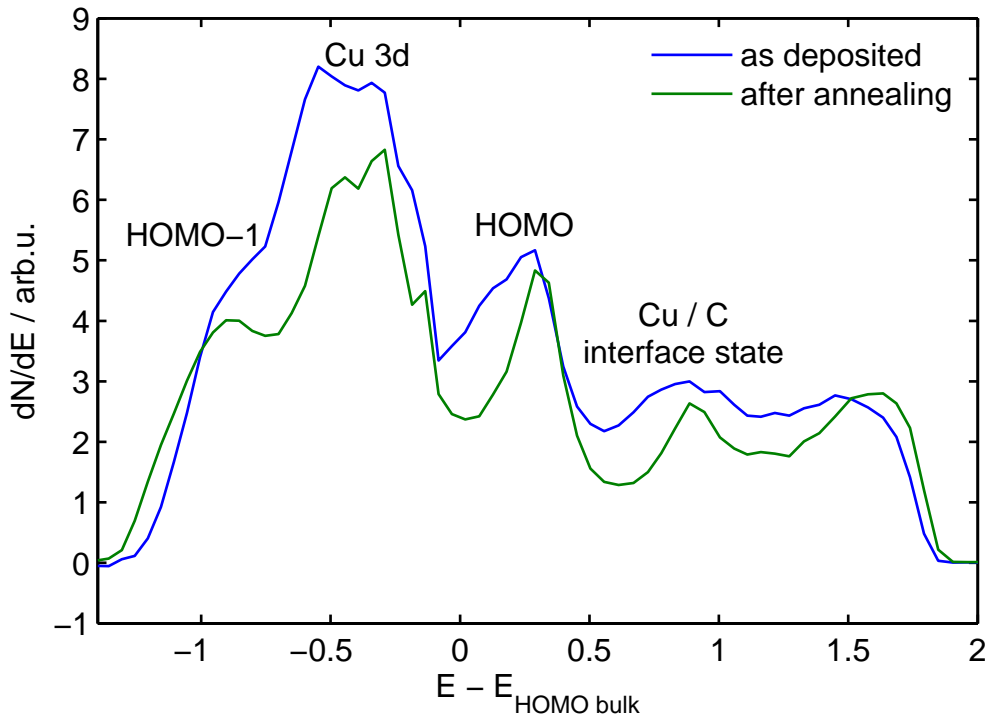


Figure 2.5: 1 ML fullerite before and after annealing measured in normal emission. Photon energy: 8.24 eV. Sample temperature: 140 K.

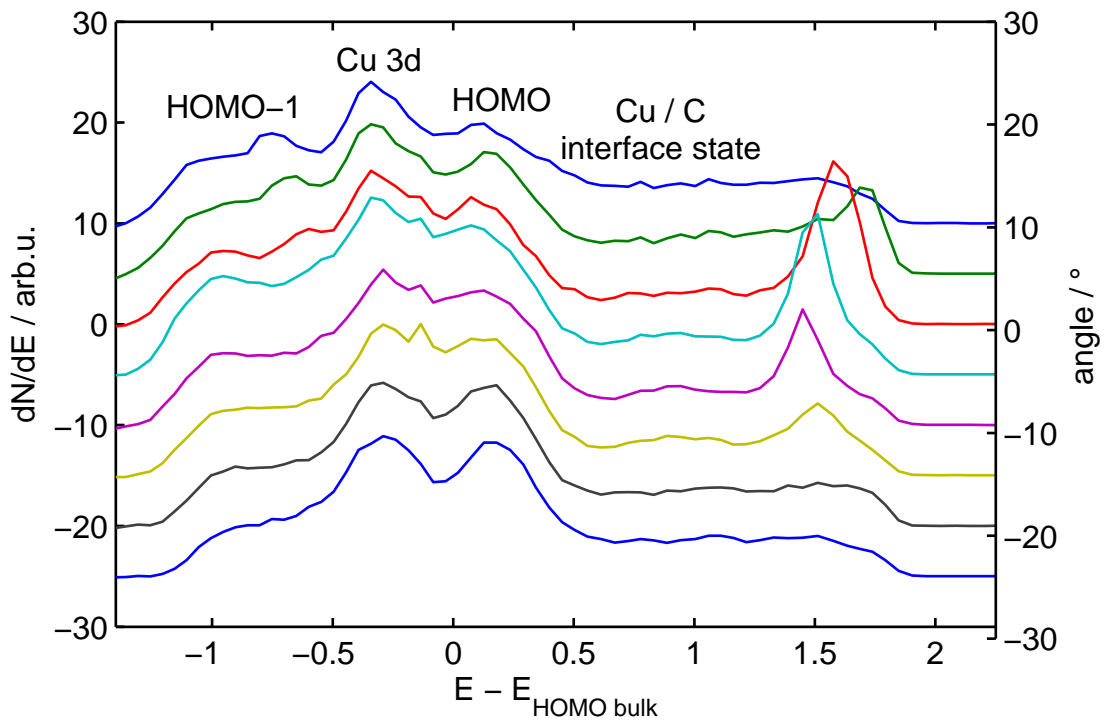


Figure 2.6: <1 ML ARUPS adsorbed at 400 K. Photon energy: 8.24 eV. Sample temperature: 140 K.

2 Experiment

radiation generated by the ion gauge or the sputter gun. The preparation quality is better for a crucible made of molybdenum than one made of copper. Fullerite from another source of supply with nominal the same purity, but with a different colour, yielded more defects.

2.1.1 Calibration of the film thickness

Since dependence of the spectra on film thickness is expected even for more than 10 ML, this parameter has to be controlled to a precision of 1 ML.

As shown in figure 2.3, the growth rate is always controlled and recorded indirectly by measuring the ion current, which is regulated to 0.5 nA. The ratio of growth rate and current is determined by evaporating in small steps and interlacing this with photoelectron spectroscopy, the result is shown in figure 2.7. The spectra are compared to the spectrum obtained by annealing the first ML and the sticking coefficient is assumed to be 1.

Since the thickness of the film is very important for the present investigation, ellipsometry using 532 nm is employed as a complementary measurement method. Dresselhaus and coworkers [58] determined the thickness of one ML to be 0.82 nm using X-ray diffraction on thick samples. This is used to calibrate the ellipsometry.

The set-up is shown in figure 2.8. The analysing polarizer is rotated a full circle and the power on the photodiode on the right of the set-up is recorded. The resulting graph is fitted by a theoretical curve given by the Jones calculus. From this curve the values at the analysing polarizer positions depicted in the figure 2.8 (S, P, dia) are used for the following analysis.

In 1887 Drude introduced ellipsometry and stated the relationship between thickness of the film and the optical constants of the surface (or substrate) upon which the film is deposited.

$$a_3 = \left(\frac{r_{01} + r_{12}P^2}{1 + r_{12}r_{01}P^2} \right) \cdot a_0 \quad , \quad (2.1)$$

with a_3 being the amplitude of the light in front of the analyser, a_0 being the amplitude of the incoming light beam, $P = \exp(ik_{\perp}z)$ with z being the fullerite thickness, and r being the Fresnel reflection coefficients. This is described in detail in [113] and in appendix A.

Behind the rotatable analyser these intensities are measured:

$$\begin{aligned} I_p &= \|a_{p3}\|^2 \\ I_s &= \|a_{s3}\|^2 \\ I_{dia} &= \|a_{p3} + a_{s3}\|^2 \end{aligned}$$

The calculation is carried out for different thicknesses to generate a look-up table.

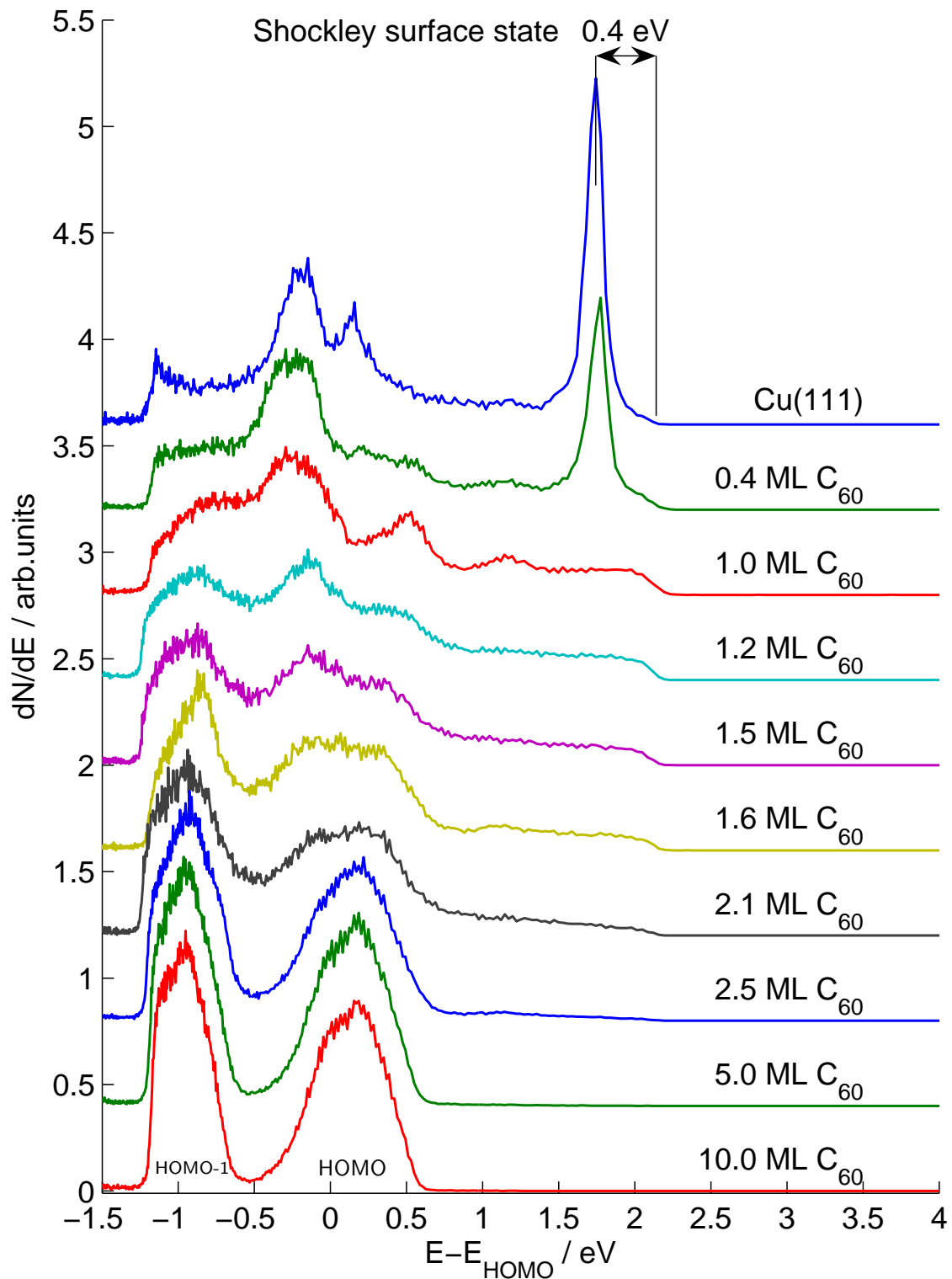


Figure 2.7: Photoemission measurements with a photon energy of 8.24 eV on fullerite films at 140 K and of different thickness. Prepared without annealing.

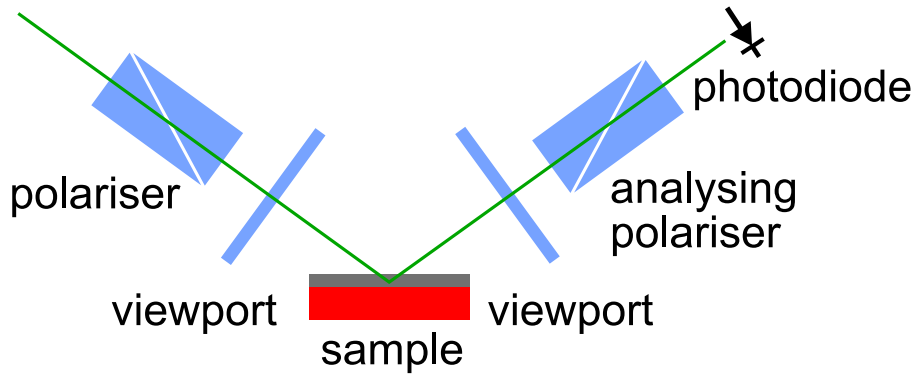


Figure 2.8: Ellipsometry set-up. The analysing polariser is rotated around the laser beam axis, and measurements are taken in three positions: in plane of incidence (p), vertical to the plane of incidence (s), diagonal (d).

Furthermore, the viewports are included in the calculation by means of the Jones calculus.

Theory depicts a change in the relative intensities in the order of 10%. Thus, it should be a valid technique for measuring the film thickness, especially considering that even thicker films are interesting to investigate. Figure 2.10 compares ellipsometry with flux integration. Both are in the same order of magnitude. Ellipsometry yields about 5 ML thicker films. Omitting two data points at 4 ML_{flux} it could also be interpreted in the way that ellipsometry predicts 1.5 times more ML. Thus, the sticking coefficient is not less than one. The noise in the ellipsometry may be reduced by classical null ellipsometry [113].

The ellipsometry offers higher ultimate precision, but critically depends on the optical alignment. Thus it is only used as a global check as discussed above, while in the following for individual preparations the thickness derived from the flux measurements is stated.

2.2 Laser system

In the present investigation a laser system is used as a photon source for the photoelectron spectroscopy, see figure 2.1. The laser system is described in detail by Finsterbusch [114–116]. A mode-locked Nd:YLF laser (Quantronix 4216 DL) generates pulses with a wavelength of 1053 nm, a duration of 50 ps and an energy of 190 nJ at a repetition rate of 76 MHz. Each pulse is split into two replicas by a half-reflective mirror. One replica seeds a regenerative amplifier (Quantronix 4417RG), increasing the energy to 2.5 mJ at a reduced repetition rate of 1 kHz and an increased pulse duration of 100 ps. The other replica pumps an optical parametric oscillator (OPO) and generates synchronous pulses tuneable in the wavelength range from 1460 to 1740 nm [115]. An optical parametric amplifier (OPA) is pumped by the regenerative amplifier and seeded by the OPO [114]. The radiation is then

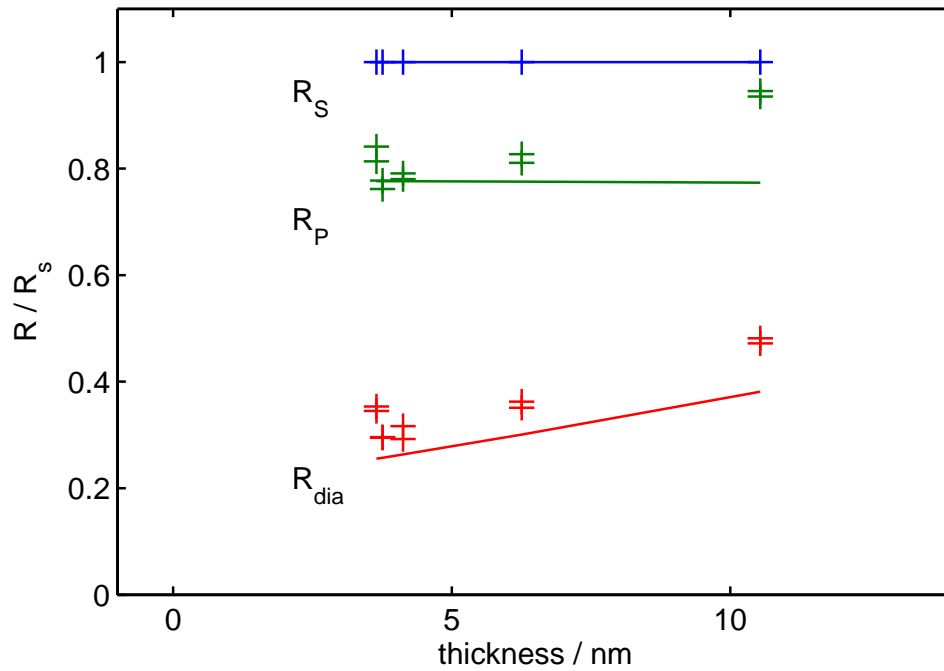


Figure 2.9: Ellipsometry experiment and theoretical prediction using fitted values for the birefringence of the viewports. For the refractive index and the influence of the substrate: see appendix A

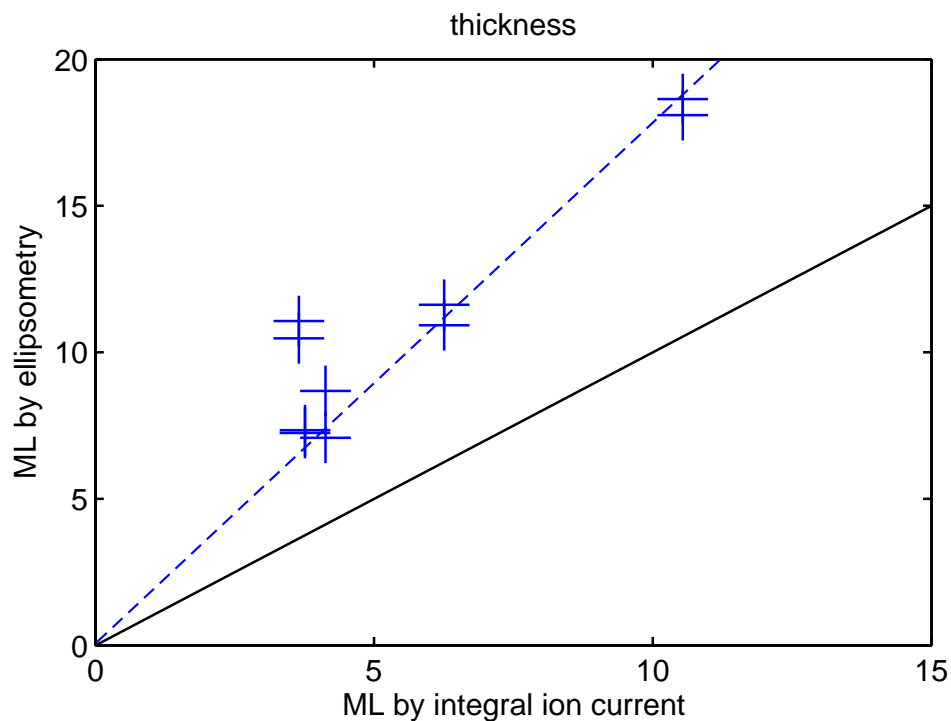


Figure 2.10: Comparison between ellipsometry and integrated ion current. The dashed blue line is a guide to the eye and the black line is the main diagonal of the coordinate system.

2 Experiment

quadrupled into the range from 365 to 435 nm (from 3.40 to 2.85 eV, 50 ps, 21 μ J) and used as the pump pulse for the C₆₀. From the partly depleted pump pulse the second (2.35 eV, 527 nm, 1.2 mJ), third, fourth (4.71 eV, 263 nm, 120 μ J), fifth (5.88 eV, 211 nm, 23 μ J), and the seventh harmonic (8.27 eV, 150 nm) are generated. Here the seventh harmonic is generated by non-resonant four-wave mixing in a Xe gas cell using the fundamental and the fourth harmonic [117].

To generate the μ s delays the pump pulse from the Nd:YLF laser is replaced by a pulse from a second laser, and an electronic delay between both lasers is employed. This second laser is a Q-switched Nd:YAG laser from Laser Design. The laser wavelength is 1064 nm (1.16 eV), and the pulse energy is set to 14 mJ. Then the pulse duration is 200 ns, and the jitter between the trigger pulse and the laser pulse is 20 ns, and the relative pulse-to-pulse energy variation is 0.1, which is comparable to the variation of the regenerative amplifier of the Nd:YLF laser system. The second (140 ns, 532 nm, 2.33 eV, 1.6 mJ) and third harmonics (120 ns, 355 nm, 3.49 eV, 9 μ J) are used in the experiment.

2.2.1 Optical parametric oscillator

The OPO is pumped synchronously and uses a periodically poled lithium niobate crystal (PPLN) as nonlinear medium. This allows for quasi phase-matching (QPM) which avoids walk-off over a large range of frequencies and allows to use the largest nonlinear coefficients of the material. The damage threshold of lithium niobate is relatively low with bulk damage occurring at 1.2 GW/cm² for 30 ns pulses at 1064 nm. This is mostly due to the photorefractive effect [116]. One countermeasure is to heat the crystal, another one is to dope lithium niobate intentionally with MgO. Therefore this OPO employs MgO:PPLN (GWU).

The OPO is tuned stepwise by changing the period length (Λ in figure 2.11) and fine tuned by changing the temperature. Large spatial temperature gradients break the crystal, thus the temperature is distributed evenly around the crystal by a massive copper piece. A comparably small electrical heater and high oven insulation prevent fast temperature changes. The insulation cannot prevent that the temperature of the optical table below the oven rises by 5 K.

The crystal features six period lengths of $28.5 < \Lambda < 31.0 \mu\text{m}$. The plus signs in figure 2.11 show measurements within the temperature range $T = 373$ to 443 K. Measurements are limited by the cavity mirrors to wavelengths in the range from 1460 to 1740 nm.

Jundt [118] published the temperature expansion of PPLN to be

$$T_E(T) = 1 + 1.54 \cdot 10^{-5}(T - 293.15) + 5.3 \cdot 10^{-9} (T - 293.15)^2 \quad ,$$

and a Sellmeier equation

$$n_z = \sqrt{a_1 + a_2 f(T) + \frac{a_3 + a_4 f(T)}{\lambda^2 - (a_5 - a_6 f(T))^2} + \frac{a_7 + a_8 f(T)}{\lambda^2 - a_9^2} - a_{10} \lambda^2}$$

with a temperature parameter $f(T)(T - 298.65)(T + 643.97)$.

The published values are used as start values for a fit to the measurements in this investigation and listed in table 2.1. The coefficients which are multiplied with the temperature parameter change completely, while the residual coefficients stay within 15% of the original value. Note that lithium niobate is birefringent and only the refractive index of the z-axis ($n_z = n_e$) is considered.

The cavity is almost confocal. To operate it within the stability region the set-up is slightly asymmetric. If a temperature ramp is applied to the crystal, the instantaneous frequency hops due to loss ripples, therefore, a birefringent filter is added [116].

The output mirror transmits 0.2 of the energy. The OPO can be pumped with up to 5 W. Then it delivers 1.5 W signal power corresponding to 30 nJ pulse energy at the repetition rate of 76 MHz. The OPO operates more efficiently if pump pulses are shortened from 50 ps to 40 ps.

2.2.2 Optical parametric amplifier

The OPO pulses are amplified by an OPA using two potassium-titanyl-phosphate (KTP) crystals as nonlinear medium. The pump pulses are derived from the Nd:YLF regenerative amplifier. At a pump energy of 2.5 mJ the signal pulses from the OPO are amplified up to a signal pulse energy of 500 μ J which corresponds to a quantum efficiency of 0.45 [116]. At the repetition rate of 1 kHz this corresponds to 500 mW average power.

The signal is polarized extraordinarily, the pump and the idler are polarized ordinary. Phase matching is achieved by rotating the KTP crystals around the direction of the ordinary polarization thus changing the extraordinary refractive index. The total length in KTP of 50 mm leads to an angular acceptance of 1°.

| | a_1 | a_2 | a_3 | a_4 | a_5 |
|-------|-----------------------|-------------------------|------------------------|--------------------------|-------------------------|
| Jundt | $0.535583 \cdot 10^1$ | $0.4629 \cdot 10^{-6}$ | 0.100473 | $0.3862 \cdot 10^{-7}$ | 0.20692 |
| MgO | $0.536874 \cdot 10^1$ | $-0.4055 \cdot 10^{-5}$ | 0.090604 | $-0.6909 \cdot 10^{-10}$ | 0.38728 |
| | a_6 | a_7 | a_8 | a_9 | a_{10} |
| Jundt | $0.89 \cdot 10^{-8}$ | 100 | $0.2657 \cdot 10^{-4}$ | 11 | $0.15334 \cdot 10^{-1}$ |
| MgO | $0.88 \cdot 10^{-6}$ | 89 | $0.1296 \cdot 10^{-4}$ | 13 | $0.17902 \cdot 10^{-1}$ |

Table 2.1: MgO-PPLN dispersion measured in the present work compared to PPLN measured by Jundt [118].

2 Experiment

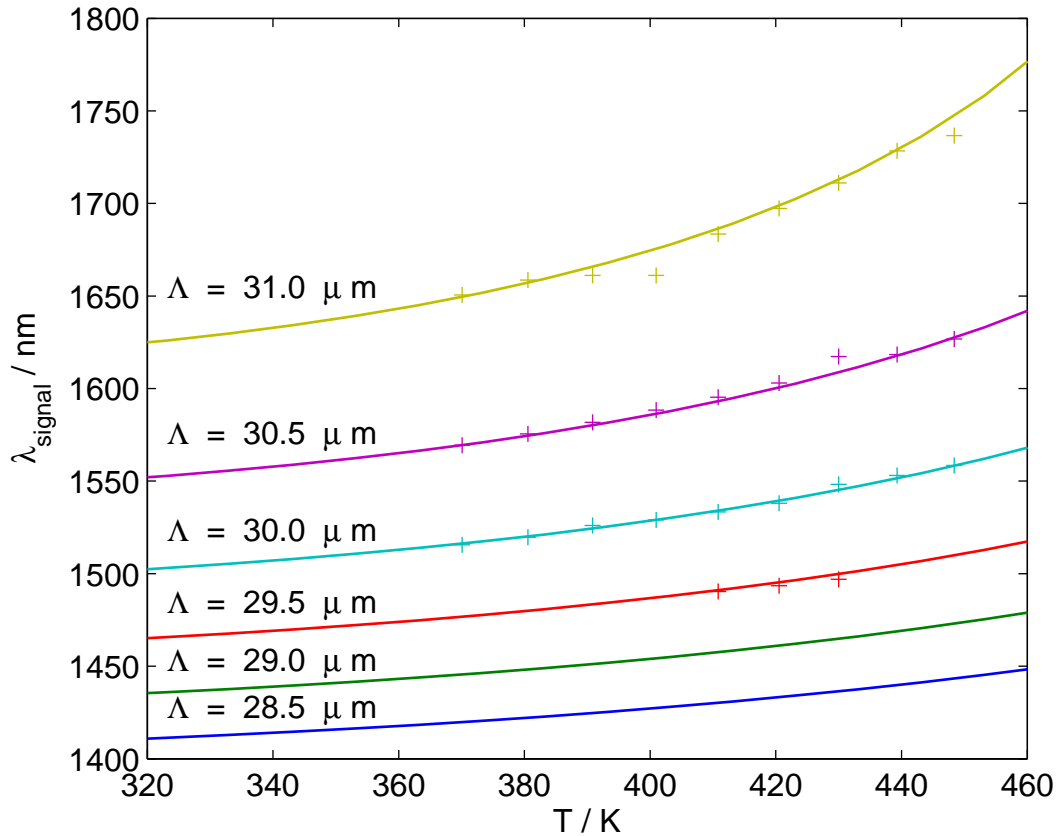


Figure 2.11: Tuning of the OPO. Λ = grating constant, curves = theory, plus signs = experiment. Note that the cavity mirrors limit the wavelengths.

The second crystal is rotated by 180° around the direction of the extraordinary polarization relative to the first crystal to compensate the walk-off² of the extraordinary polarized signal and refraction on the surfaces. As shown in figure

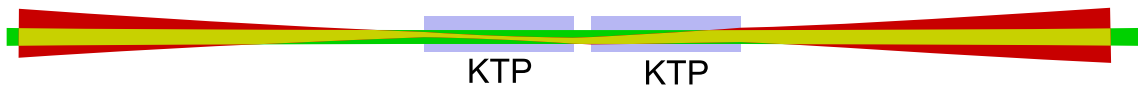


Figure 2.12: KTP walk-off compensation.

2.12, the seed pulse enters the first crystal displaced relative to the pump beam [119]. It then walks across the whole pump beam profile, which has a diameter of 0.5 mm, producing an elliptic idler profile. In the second crystal the seed pulse walks back across the whole pump beam profile.

In the first crystal the signal is focussed as much as permitted by the angle acceptance so that the complete signal profile is evenly and strongly amplified near (limited by walk-off) the centre of the pump profile.

In the second crystal the signal beam diameter is comparable to the pump beam diameter so that the pump can be depleted. The idler is not removed between the

²walk-off means that the phase fronts are not orthogonal to the Poynting vector

two crystals and can interact with the pump and the signal. In the 50 mm air gap between the two crystals the idler phase theoretically shifts by 20° relative to signal and pump. The air space can be reduced as depicted in figure 2.12. Depending on the relative orientation and twinning [120]³ of the two crystals the signal beam can shift the phase by 180° [121].

Starting with angle phase-matched crystals and then rotating both crystals at once and monitoring the signal power the phase shift leads to two angles being equally efficient and separated by a less efficient angle. At this less efficient angle in the far field the signal beam profile is divided into two halves by a horizontal gap, which has been observed.

The Gaussian temporal shape of the pump pulse leads to low amplification in the tails of the Gaussian. This has no influence on the signal because the OPO pulses are shorter by a factor of two. As a side effect a hole is burned into the temporal shape of the pump pulse. Since the pump pulse is then used to generate the probe pulse for the 2PPE experiment, a pronounced hole must be avoided and the OPA must not to be aligned to the highest quantum efficiency.

For every new wavelength the OPO, OPA, and the fourth harmonic generator (figure 2.1 in the middle column) are realigned. The transfer optic between laser system and vacuum chamber is adjusted to correct for the chromatic error of the lenses. Between parameter changes the laser system is controlled and readjusted if necessary. Warming up of the laser system takes about 3 hours, mainly due to the temperature stabilisation of the environment, which influences the temperature distribution in the air conditioned laboratory.

2.3 Photoemission

In this section the 1PPE, the 2PPE, and the time-resolved 2PPE experiment are described. The set-up, the data-acquisition approach and data-acquisition software, and the analysis methods are covered.

2.3.1 Approach

Time-resolved 2PPE experiments require a defined delay between the pump and the probe pulse. Eberhardt and coworkers [39] used a list of delays suited for a logarithmic scale. The mechanical delay steps are chosen slightly shorter than the laser pulse duration to reduce the width of the Poisson distribution.

Photon energies are covered in the range from 2.35 eV to 8.27 eV, and the flexible optical set-up allows to employ the following, different variations of photon energies:

- The 8.27 eV (151 nm) photon energy is used to check the preparation for low defect density and thickness, see figure 3.1.

³ Twinning is an abbreviation for a crystal showing twin domains. In the parametric oscillator twin domains were introduced deliberately to shift the phase by 180°

2 Experiment

- 4.71 eV (263 nm) and 5.88 eV (211 nm) photon energies are used to probe excited states. See figure 3.21 and 3.5.
- 2.35 eV (527 nm) and 3.50 eV (355 nm) photon energies are used for time-resolved 2PPE, see figure 3.5 and 3.6.
- The tunable radiation from the OPO is used to get a dynamic spectrum of the transitions from the ground state to an excited state. See figure 3.21 and figure 3.22.

The probe beam spot is adjusted to be within the pump beam spot by means of a camera directed at a fluorescence screen (zinc silicate) replacing the sample. In the initial experimental layout (prior to 2005) the adjustment of the pump-and-probe overlap on the sample was achieved by positioning the pump beam profile (area: 2 mm^2) laterally in a 5 by 5 grid relative to the probe (area: 1 mm^2) profile. The grid covered an area of 5 mm by 10 mm on the sample. Therefore in this initial experiment a spot size larger than 1 mm^2 was chosen.

2.3.2 Set-up

The set-up has already been sketched in figure 2.1 and the major features important for the 2PPE in particular are described in the following. The delay between pump and probe pulses is adjusted by opto-mechanical or electronic means. The opto-mechanical delay line spans 600 ps with a step size of 12 fs and is employed for the pulses with a duration of 50 ps from the YLF laser system. The electronic delay generator is part of the data acquisition board (Meilhaus Electronic ME-4610 1.2D Typ ME-Jekyll) in the computer. It spans 6.5 ms with a step size of 100 ns, and is employed for the pulses with a duration of 120 ns from the YAG laser system. Laser synchronous choppers are employed in the pump and the probe beam. The photodiodes are mounted besides the laser beam. A reflex of the laser pulses from the viewport is directed onto the photodiodes (see figure 2.1). Each laser pulse intensity is recorded by photodiodes (PD0 and PD1 in figure 2.1) and converted to an integer by an analog-to-digital converter (ADC, Meilhaus Electronic ME-4610 1.2D Typ ME-Jekyll).

The laser pulses are p-polarised with respect to the sample surface. A lens weakly focuses the pump beam to a 0.25 mm^2 spot on the sample. This spot is elliptic due to the 60° off-normal incidence. Photoelectrons emitted from the sample in normal direction fly through a ToF tube and are detected after a distance of 405 mm. The ToF tube is aligned along the horizontal component of the earth magnetic field in the laboratory, which amounts to $20 \mu\text{T}$. The vertical component of the earth magnetic field amounts to $40 \mu\text{T}$. The magnetic field acting on the emitted electrons is reduced by a μ -metal cylinder (thickness: 0.5 mm [122], inner radius: 196 mm) in the sample chamber and a another μ -metal cylinder (thickness: 0.2 mm, inner radius: 76.5 mm) around the ToF tube. Using a fluxgate magnetometer the residual vertical internal

magnetic field was determined to be below $2\mu\text{T}$. Considering as a worst case the Lorentz force on an electron and the centripetal force needed to bring an electron onto a circular path

$$m_e v^2 / r = e_0 v \times B$$

with m_e being the electron mass, v being the velocity of the electron, e_0 being the charge of the electron, and B being the above mentioned hypothetical magnetic field of $2\mu\text{T}$, an electron with the typical kinetic energy of 1 eV travels on a circular path with a radius of about 2 m. Since the distance between the sample and the micro channel plates (MCP) is only 405 mm, the electrons emitted in normal direction deviate less than 41 mm from the centre of the ToF tube, the angles in ARUPS are shifting less than 11° , and the electron path length variation to the MCP, which has an active diameter of 40 mm, is less than 8 mm. The slowest electrons need about 405 ns to pass the ToF distance. For these electrons the variation of their ToF is in the order of the time resolution of the TDC (see below), and thus it can be concluded that the shielding is sufficient.

Between the sample and the ToF tube a voltage is applied to extract the electrons. The ToF tube starts with an inverted cone to achieve a fast reduction of this electric field, and the ToF tube ends with a grid to shield it against electric fields in the MCP assembly.

After the ToF tube each electron is multiplied in two MCPs operated at a voltage of 850 V each. The resulting electron cloud hits a 50Ω anode leading to electrical pulses with 10 mV pulse height. A cascade of 4 InGaP heterojunction bipolar transistors (MAR by minicircuits with 1 mV equivalent input noise) amplifies these pulses to 3 V pulse height. Jabs [103] measured the frequency response of 4 transistors of this type and determined a bandwidth of up to 2 GHz.

A time-to-digital converter (TDC) with a quartz stabilized resolution of 125 ps (ACAM AM-GP1) converts the delay between this pulse and an electrical pulse supplied by the laser electronics into a 16-bit integer number. After a dead time of 20 ns the next delay can be determined. To reduce the chance that a second electron reaches the detector within this time interval the average count rate is adjusted to less than 0.5 electrons per laser pulse. The combined time resolution of the ToF tube and the TDC is 4.7 ns leading to an energy resolution of 40 meV [122]. In the current investigation in figure 2.7 a FWHM of 133 meV is measured on the Cu(111) Shockley surface state, while A. Goldmann and coworkers [123] have measured a better FWHM of about 40 meV using a photon energy of 21 eV due to their better angular resolution. The time resolution of the delay is given by the cross correlation of the laser pulses, which can be determined to be 80 ps by means of the 2PPE signal in the energy range of the LUMO+1. The measurements prior to 2005 were recorded with a computer equipped with a Motorola CPU with 68000 architecture, a VME bus, a LeCroy TDC, and a SCSI hard disk. The measurements since 2005 employ a standard PC with a 400 MHz 586 CPU.

2.3.3 Measurement software

The measurement program reads out and stores the TDC and the ADC values for each laser pulse. The ACAM TDC software allows precise timing by low-level programming. The Meilhaus ADC driver uses an internal buffer. For performance reasons the measurement program is written in C++, and inside the inner loop exclusively 32-bit integers are used. Data array structures are accessed without boundary checks and are programmed at a low level with bit operations and unitary operators.

Prior to beginning the measurement a list of pump-probe delays with a fixed interval is generated by the software and shuffled to quasi-random order. For the measurement the software iterates repeatedly through this list.

2.3.4 Analysis

For each electron the time-of-flight (ToF) is measured, but for physical interpretation the kinetic energy at the time of emission needs to be known and is calculated to various degrees of accuracy as discussed by Göhler, Pauksch and Jabs [103, 104, 122]. To compare spectra taken with different photon energy, the photon energy is subtracted from each spectrum. From a spectrum with a clearly visible fullerite HOMO the energetic position of the HOMO peak is taken and subtracted from all spectra [38].

To generate a spectrum of the kinetic energies of the electrons a histogram is generated and drawn as a bar chart where the area of each bar is proportional to the number of electrons in this energy range. Since in this investigation the bars of a single histogram have variable widths, the height of the histogram is proportional to the number of electrons in this energy range divided by the width of the energy range. In the current investigation only the height of the bars is plotted and connected by a line as a guide to the eye. Figure 2.6 is an example of histograms with constant widths. Since kinetic energy cannot be negative, and due to the extraction voltage between the sample and the ToF tube, the slowest electrons have a finite ToF. This leads to a low energy cut-off [38, 124] in the histograms. For large delays dynamic spectra measured at multiple delays are summed up before further processing to reduce the width of the Poisson distribution even more as is visible for example in figure 3.8 to 3.17. Dynamic spectra for different delays are composed into one time-delay spectrum, which is a scalar valued function of a two dimensional vector. Colour coding enables a 2-dimensional depiction (see figure 3.5).

2.3.4.1 Photodiode signals

The photodiode signals represent the laser pulse energies and are used for monitoring choppers, the laser stability, compensation of laser fluctuation, and, after calibration, determining the signal dependence on fluence.

In the following sections the “pump-pulse only” dynamic spectrum and the “probe-pulse only” dynamic spectrum are called figuratively mono-colour dynamic spectra and the pump-probe dynamic spectrum is called the bi-colour dynamic spectrum. Their respective integral amount of photoelectrons is in the same order of magnitude. The switching between the three kinds of measurement is done by choppers in the pump and the probe beam. To retrieve the pump-probe signal only, the mono-colour spectra are subtracted from the bi-colour spectrum, sometimes leading to negative values because of the still to be applied dead-time (see section 2.3.2) correction [125].

Histograms of the energy of the pump and the probe pulses are derived. From the histogram ranges for the cases “laser pulse passed chopper” (for example “ $0.030 < \text{fluence} / (\text{mJ}/\text{cm}^2) < 0.065$ ” in figure 3.8) and “laser pulse was blocked by the chopper” are derived automatically⁴ to retrieve the mono-colour dynamic spectra and the bi-colour dynamic spectrum. Extreme pulse energies are rejected to avoid detrimental effects. For measurements showing low noise after background subtraction the data is additionally sorted into low and high pulse fluence.

For every group of 100 000 laser pulses belonging to the same pump frequency and the same delay the pump-only, probe-only, and pump-probe dynamic spectra are normalized relative to photodiode values. The bi-colour signal is normalized by the product of the signals from both photodiodes and the mono-colour signal is normalized in different ways, depending on the photon energy. If the probe pulse photon energy is 4.7 eV (263 nm) (see for example in figure 3.21), the square of the photodiode PD0 signal is used. If the probe pulse photon energy is 5.9 eV (211 nm) as in all other time-resolved measurements, the photodiode PD0 signal is used directly. The pump pulse is always normalized by the square of the photodiode signal because either the photon energy is high enough for 2PPE as in the triplet measurements or in the singlet measurements with more than 3.0 eV (413 nm) photon energy or the signal is so weak that a small error in the norm gets even smaller after error propagation. More details are presented by Göhler [104].

Due to the large amount of subtracted mono-colour background the dynamic spectra are noisier near the low energy cut-off than at high energies. In order to achieve a levelled noise distribution across all slots, the dynamic spectra are weighted appropriately and this is done in dialogue on the computer.

2.3.4.2 Separation of time-delay spectra into states

The experimental literature describes the electronic structure of C_{60} as a collection of discrete excited states, each with their individual dynamic spectra (examples of dynamic spectra are shown in some figures 3.7–3.16) and time state dynamics (some examples of state dynamics are shown in some figures 3.8–3.17).

⁴because of laser drift no fixed ranges can be used

2 Experiment

A cut through a time-delay spectrum along a fixed delay renders a good dynamic spectrum for the lowest triplet exciton, but a bad dynamic spectrum for a short living state due to temporal overlap, see for example in figure 3.5. A cut through a time-delay spectrum along a fixed energy renders a good state dynamics for the LUMO+1 exciton, but cannot separate the state dynamics of the lowest singlet exciton from the excited singlet excitons due to spectral overlap. Though later a computationally expensive method will be discussed which can fit two lifetimes to a single cut, it is desirable to fully exploit the already stated properties of the electronic structure of C₆₀ before adding new assumptions. Eberhardt and coworkers [39] and Kabler and coworkers [40] also did not rely on cuts alone and fitted a superposition of dynamic spectra, Gaussians in Eberhardts case, to the time-delay spectrum. Since no Gaussians are obvious in the present investigation and to ease the fitting procedure, the dynamic spectra and state dynamics are expressed as matrices much like in a cut. An artificial case with clearly separated spectral lines or events at separated points in time may serve as a first test for the fit. A human would look for spots in the time-delay spectrum and then cut through them. A human would limit the cut length to only cut through one spot. To make the program robust against noise and overlap, it does not scan through the time-delay spectrum value by value, but the program is based on inversion of the superposition of states:

$$I(E_{e^-}, t_{\Delta}) = \sum_{n=0}^m I_n(E_{e^-}) \cdot I_n(t_{\Delta})$$

The symbols are defined as follows: I = intensity, E = energy, e^- = electron, t = time, Δ = difference, t_{Δ} = delay.

- The graph of a typical function $I(E_{e^-}, t_{\Delta})$ called a time-delay spectrum is plotted in figure 3.5. It will be abbreviated by I being a matrix.
- The corresponding functions $I_n(E_{e^-})$ called dynamic spectra are plotted in figure 3.16. It will be abbreviated by E being a matrix whose number of rows corresponds to the number of states.
- The corresponding functions $I_n(t_{\Delta})$ called the state dynamics are plotted in figure 3.17. It will be abbreviated by Δ being a matrix whose number of columns corresponds to the number of states. This experimental result corresponds to the theoretical curves $I(t_1)$ in section 1.2.2.3 and will be plotted together for example in figure 3.15.

This leads to:

$$I = E \bullet \Delta \tag{2.2}$$

Here \bullet denotes the matrix multiplication. The goal is now to extract E and Δ from the given I . The singular value decomposition (SVD) appears to be quite

suitable to this task. Okamoto and Sakurai [126] applied it to time-resolved X-ray scattering and were able to determine the number of significant basic scattering functions contained in the data set. Moffatt and coworkers [127] mentioned that the SVD is commonly used in the analysis of time-resolved measurements and that truncating the SVD result allows for an unbiased differentiation between signal and noise.

The SVD is usually expressed as

$$A = U \bullet S \bullet V^T \quad .$$

Here A is a generic matrix, U is an orthonormal matrix, V is an orthonormal matrix, S is a diagonal matrix (in this section: not source), and T denotes taking the transpose. The two products of this equation are reduced to one product by substituting $\sqrt{S} \bullet \sqrt{S} = S$ leading to $A = U \bullet \sqrt{S} \bullet \sqrt{S} \bullet V^T$. Using the associativity of the matrix product this is rewritten as

$$A = (U \bullet \sqrt{S}) \bullet (\sqrt{S} \bullet V^T) \quad . \quad (2.3)$$

By substituting $I = A$, $E = (U \bullet \sqrt{S})$, $\Delta = (\sqrt{S} \bullet V^T)$ equation 2.2 is formally reproduced, with different dimensions of E and $(U \bullet \sqrt{S})$ though. The rear rows of $(U \bullet \sqrt{S})$ contain only zeros (except for noise). This is a test for the quality of the data, the assumption on the number of states, and the general validity of describing the system by a small number of states [127]. The zeros are cut off to match the dimensions to I . The different energies in the time-delay spectrum need to be weighted before the SVD. The weighting function is a compromise between equalized noise across the spectrum and emphasis on already known state energies. It is related to taking cuts in the sense that cutting means to put the full weight on one energy and zero weight on all other energies. After the SVD the weighting is undone to the dynamic spectra.

The SVD is computed using standard linear algebra algorithms, of which only the outermost routine is of iterative nature [128]. For the low resolution data on a 2006 personal computer the iteration takes only some seconds and no numerical instabilities or excessive rounding errors occur.

2.3.4.3 Positive populations

As was mentioned before in section 1.2.2.2, the data in the current investigation represent probabilities and populations, which are positive.

SVD is likely to create negative and positive numbers. Therefore, one usually applies the SVD, truncates the result, reverses the SVD, and proceeds with cutting through the time-delay spectrum at a specific delay or energy [126, 127]. In the current investigation the SVD is not reversed. Instead a 1 (unity matrix) is formally inserted into equation 2.3:

2 Experiment

$$\begin{aligned}
 A &= (U \bullet \sqrt{S}) \bullet 1 \bullet (\sqrt{S} \bullet V^T) \\
 A &= (U \bullet \sqrt{S}) \bullet B \bullet B^{-1} \bullet (\sqrt{S} \bullet V^T) \\
 A &= (U \bullet \sqrt{S} \bullet B) \bullet (B^{-1} \bullet \sqrt{S} \bullet V^T)
 \end{aligned} \tag{2.4}$$

By substituting $I = A$, $E = (U \bullet \sqrt{S} \bullet B)$, and $\Delta = (B^{-1} \bullet \sqrt{S} \bullet V^T)$, equation 2.2 is reproduced.

The matrix B is then varied to make E and Δ as positive as possible, which is expressed as minimization of an exponential penalty function f_p :

$$f_p(E) = \sum_{j=1}^{j \leq j_E} e^{-E(j)} + \sum_{j=1}^{j \leq j_\Delta} e^{-\Delta(j)}$$

Since mono-colour and dark noise background subtraction already may lead to negative population, perfectly positive functions are rarely to be gained. Rigorously adhering to positive populations definitely limits the number of analysis methods.

Considering again the test case of clearly separated states and low noise, the penalty function has as many symmetric global minima as there are permutations of the states. After the minimizing fit converged into one of these minima the arbitrary permutation is removed by sorting the states by their mean energy. Thus for the test case this is an automated replacement for the manual cutting procedure. Like for the cut it is possible to fit two lifetimes to each state dynamics. In a test with two extracted states the fits yielded four lifetimes which were within the uncertainties of the already known two lifetimes.

Unfortunately for many measured time-delay spectra the minimization needs to be stabilized by blending it with a fit of the state dynamics and dynamic spectra to the cuts. The lifetimes computed using the cut and the lifetimes computed using the SVD based-analysis differ, sometimes by a factor of 10. Thus in the present investigation both results are shown and compared with each other. The reason is that the time-delay spectra contain three states and the minimization is often only stable if separating into two states. To stabilize a fit of three states, it is likely necessary to manually average over energy ranges. Then the dynamic spectra would only contain about 5 data points. Still the SVD-based analysis is an improvement over a simple cut because the SVD automatically counts the numbers of states, only the SVD-based analysis separates overlapping states, and the stability of the minimization gives additional feedback about the quality of the data and the assumptions.

2.3.4.4 Minimum of a function

The optimization is based on finding the absolute minimum of a function ($\mathbf{R}^n \rightarrow \mathbf{R}$), see, for example, section 2.3.4.5. A large number of algorithms is documented in the

literature, and the current investigation employs these four rather simple ones:

- sampling values on a regular grid
- the simplex method
- steepest descent
- the Gauss-Newton method

If the first and second derivative of the function is readily available, the steepest descent and Gauss-Newton methods are combined into the Levenberg-Marquardt method [129], and this combination is used, resulting in a fit parameter and its uncertainty. Otherwise the grid search is used and the result is refined using the simplex method. No uncertainty is available in this case.

To finish a minimization under one hour within Matlab it is necessary to use a function which is quadratic with respect to some of its arguments. Then only a small number of parameters need to be found by iteration. One needs to pass over local minima along the nonlinear parameters. To find the optimal matrix B (from equation 2.4) automatically, typically the values -1.5, -0.5, +0.5, +1.5 are tried out for every element of B . This procedure is called sampling on a regular grid. In contrast, the simulation is fitted manually to the state dynamics, and the result is then refined by the simplex method.

2.3.4.5 Fitting the simulation to the measured state dynamics

In mathematics fitting is defined as minimizing the squared difference between the simulation and the data by changing the parameters.

In case of the state dynamics, this is the function:

$$\|\Psi(R_0) - \Delta\|^2 \leq \|\Psi(R) - \Delta\|^2 \quad \forall R$$

The parameters of the simulation (section 1.2.2.3) are the source S and rate R . In this investigation a one-to-one relation between the simulated states and the states extracted from the time-delay spectrum is implied. About half of the resulting state dynamics show a bi-exponential decay. This applies to measurements done by means of the mechanical and the electronic delay. For these cases multiple simulated states are superimposed and then fitted to one state dynamics. A typical result is shown in figure 3.11.

The state dynamics measured by means of the electronic delay are fitted to a single exponential decay because the pulse duration is much shorter than the measured delay range and multiple states with transitions between them are not expected, see for example figure 3.28. The Levenberg-Marquardt method is used in this case and errors for the fit parameters are available.

2 Experiment

The state dynamics measured by means of the opto-mechanic delay is fitted to a rate equation because transitions between multiple states are reported in the literature. Since the opto-mechanic delay steps are smaller (30 ps) than the laser pump probe pulse correlation duration ($\sqrt{w^2 + w_p^2} = 80$ ps), the impulse response of the sample has to be convoluted with the Gaussian shape of the laser pulses. A typical case is shown in figure 3.15. For convergence the baseline and the rate from a lower state into a higher state have to be fixed at zero, the lower states have no influence on higher states. The simplex method is used in this case and no errors for the fit parameters are available. Kabler and coworkers [40] and Eberhardt and coworkers [39] employed theories about the dynamic spectral shape of the emission. In the present investigation this could be applied successfully to the dynamic spectra in figure 3.16. In principle this allows to fit the simulation directly to the datasets of individual electron ToFs.

The dependence of the fitted parameters on other parameters (than delay) like film thickness, temperature, photon energy, or laser pulse fluence, are listed or plotted, for example in figure 3.20. The spectra and the dynamics are manually inspected to ensure that no characteristic is left out.

3 Two-photon photoemission on fullerite films

3.1 Spectroscopic results

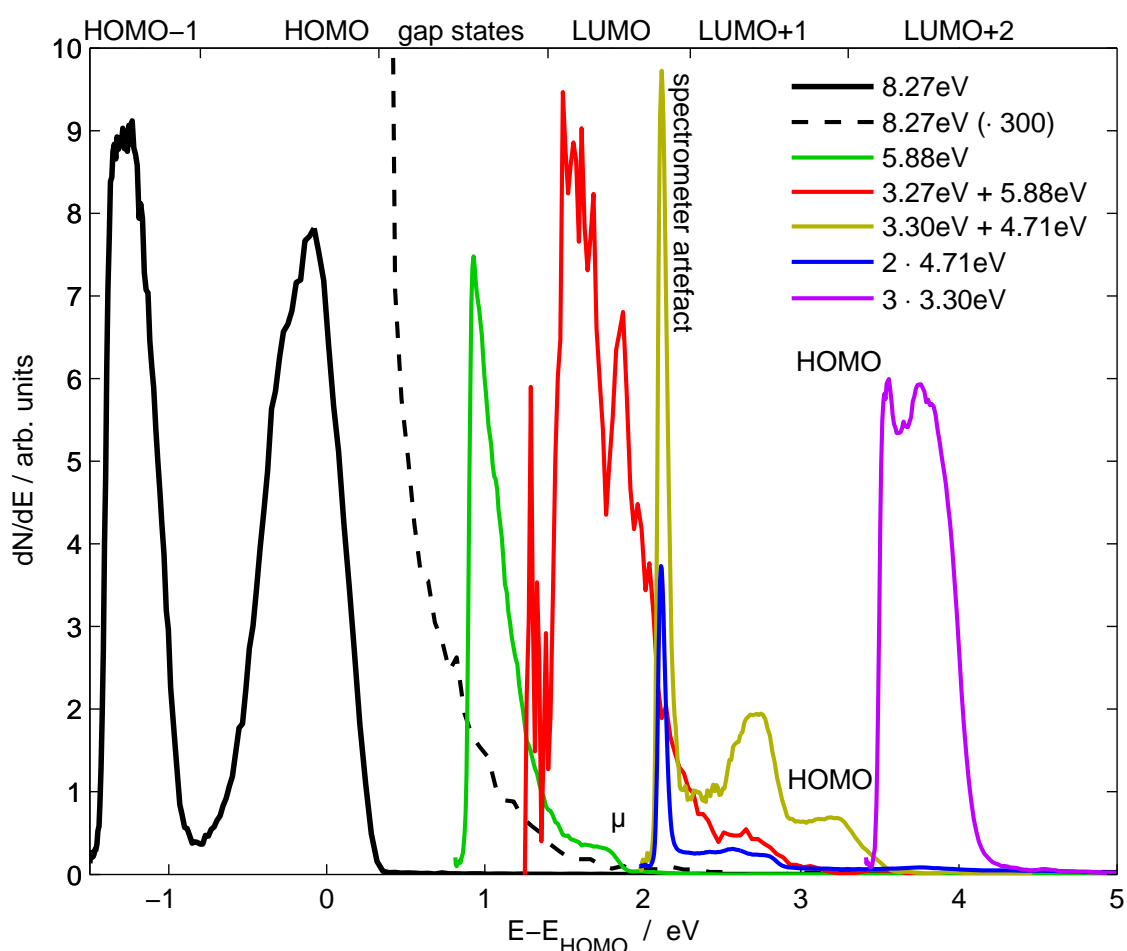


Figure 3.1: Photoemission spectra of fullerite using various photon energies. The spectra 3.27 eV + 5.88 eV and 3.30 eV + 4.71 eV are background-subtracted pump-probe spectra taken at zero delay. E is the kinetic energy of the emitted electrons. μ is the chemical potential. The energy ranges marked as LUMO+x belong to excitons with an electron in the respective state and a hole in the HOMO.

Figure 3.1 shows a combination of typical spectra, as measured, and two-colour

3 Two-photon photoemission on fullerite films

photo-emissions dynamic spectra from which the mono-colour background is subtracted. In the current 80-ps 2PPE investigation and in 120-fs 2PPE measurements the LUMO+2 exciton appears at 4.0 eV and the LUMO+1 excitons appears at 2.8 eV. The singlet exciton energies are in overall agreement. Furthermore, in the triplet dynamic spectrum in figure 3.27 4% of the electrons have energies in the range from 1.7 to 2.7 eV. These probably originate close to the metal substrate and thus have 0.8 eV higher energy (see section 1.2.4). The difference between the warm (section 3.3) and the cold preparation (section 3.4.1) is more significant than the difference between different film thicknesses, and therefore traps are needed as a second source of these electrons. Trapping implies that for the exciton the energy is lowered in the trap. Generally this could either mean a lower energy for the electron, which would lead to lower kinetic energies in the spectrum, or it could mean a lower energy for the hole maybe in combination with a slightly higher energy for the electron, which would lead to higher kinetic energies in the spectrum. The latter case is visible in the spectra. Also an improved polarizability of the trap and its surrounding would lower the Hubbard U and lead to a higher kinetic energy of the emitted electron. In the cold preparation both dynamic spectra, from the excited exciton and from the lowest singlet exciton, have peak with a 0.8 eV long high energy tail. The peak in the dynamic spectrum of the lowest triplet exciton also has such a tail, which is visible in figure 3.33.

Though the appearance of a delay-dependent signal in two-pulse experiments is sufficient to prove nonlinear effects, the pulse fluence is varied over one order of magnitude to separate two-photon photoemission from third or even higher order effects in a time integrated, mono-colour experiment. The corresponding result is shown in figure 3.2. At low fluence gap states lead to one-photon photoemission below 2.5 eV. The mean value above 2.9 eV is taken and plotted in figure 3.3, it can be fitted to a parabola implying two-photon absorption. The dynamic spectra normalized by this value are shown in figure 3.4. The high energy tail of the LUMO+1 in the intermediate step, the peak of the LUMO+2 in the intermediate step and the peak of the HOMO in the initial state are all probed by two-photon photoemission. The low energy part of the LUMO+1 dynamic spectrum is assumed to behave in the same way, but it overlaps with the one-photon background and thus is not directly visible. The complete LUMO dynamic spectrum is hidden in this one-photon background in this cold preparation (section 3.4). This background cannot be a (pure) two-photon signal, because in figure 3.4 the spectra show a large variance in the electron energy range between low energy cut-off and 2.5 eV.

At a fluence of 0.5 mJ/cm² the 20 ns dead time of the TDC leads to a saturation of the signal. Note that low energies correspond to large delays. At higher fluence the saturation evolves into a dip and grows to larger kinetic electron energies.

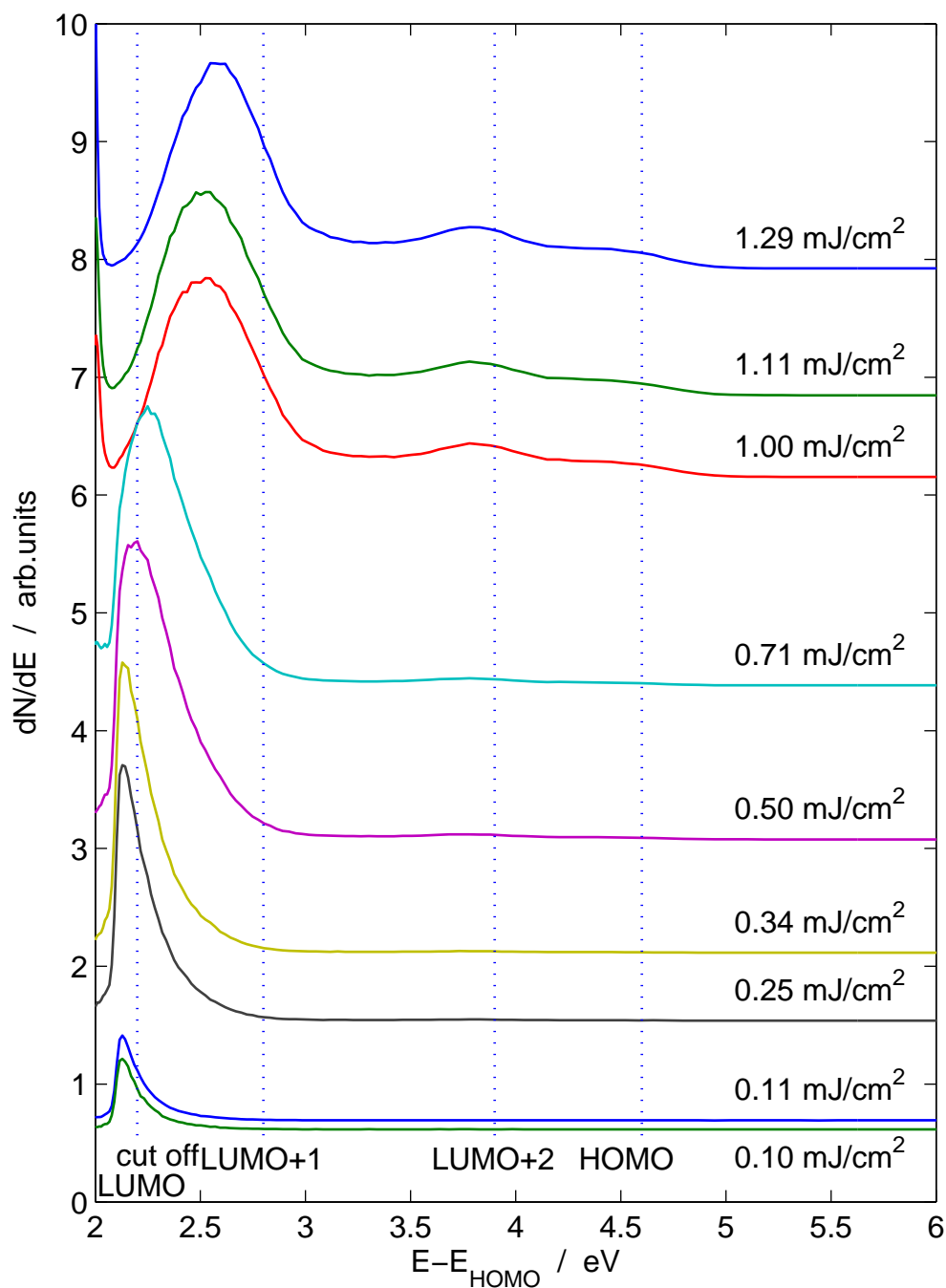


Figure 3.2: UPS as a function of the intensity at the photon energy of 4.7 eV (263 nm).

3 Two-photon photoemission on fullerite films

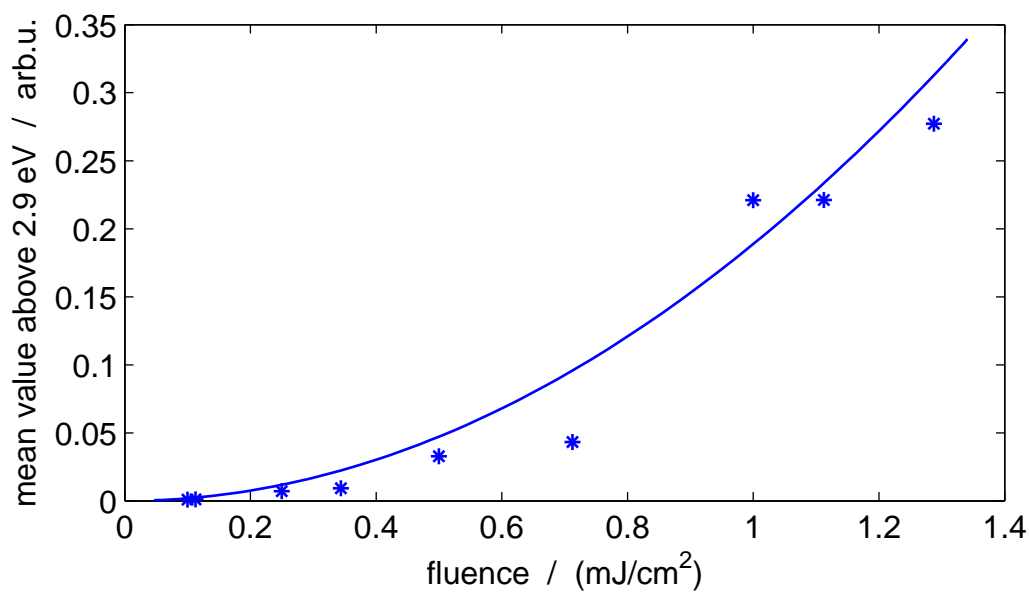


Figure 3.3: Mean value above 2.9 eV in figure 3.2 as a function of the intensity at a photon energy of 4.7 eV ($\lambda = 263$ nm). The curve is a parabola centred around zero fluence.

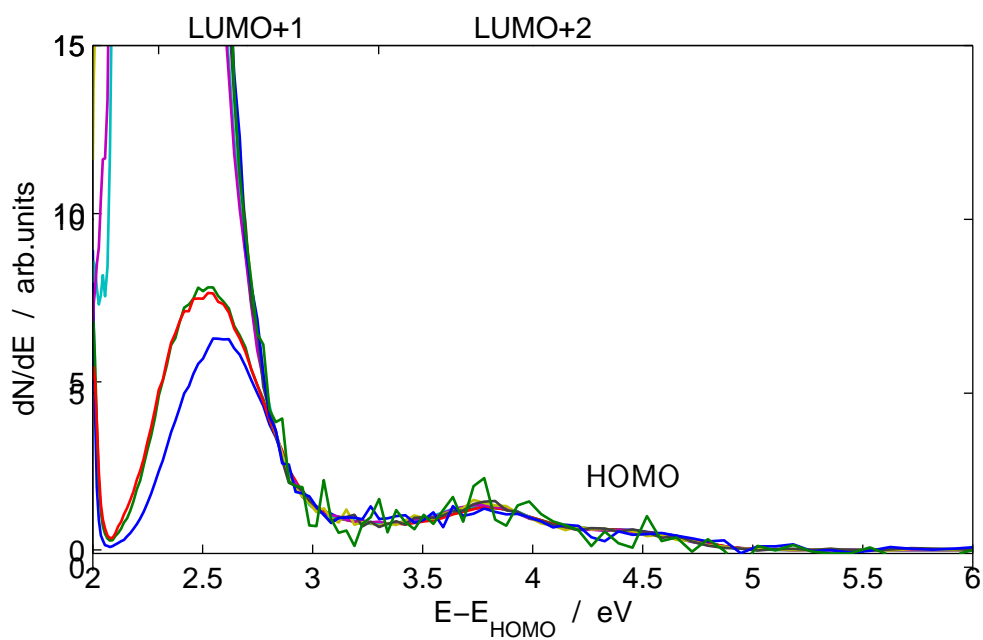


Figure 3.4: UPS shown in figure 3.2 normalized by the mean value above 2.9 eV as a function of the fluence at a photon energy of 4.7 eV ($\lambda = 263$ nm).

The extraction voltage allows electrons to fly through the ToF tube which have barely left the sample. Space charge within the ToF further reduces the speed of the electrons in the tail of the electron pulse and these electrons appear below the low energy cut-off (see section 2.3.4). In figure 3.4 the normalised signal below the low energy cut-off is the same for all pulse energies. This implies that the normalised signal increases quadratically, which is a typical space charge effect and does not relate to spurious reflections within the ToF electronics, which would be linear, or dark noise, which would be constant.

3.2 Time-resolved results

Figure 3.5 shows a time-delay spectrum taken with a pump photon energy of 2.36 eV (527 nm) and a probe photon energy of 5.88 eV (211 nm). It incorporates delays of up to 100 ns. At zero delay the dynamic spectrum extends from the low energy cut-off at 1.3 eV to 2.3 eV, which is the pump photon energy. Above 1.7 eV the dynamic spectrum is more intense by a factor of 8 (deducible from the colour scale) when the laser pulses overlap. This is an indication that most of this signal is generated by two-photon absorption without populating an intermediate state. As mentioned in section 1.2.2, photons with an energy of 2.36 eV lead to a polarization in the extreme tail of the lineshape of the first dipole-allowed transition, which in combination with a probe photon excites an electron. Without population there is no decay and like in figure 3.1 a replica of the spectrum of the HOMO appears shifted to higher energies. Additionally the spectrum may be influenced by a larger dipole moment of transitions out of the larger Wannier-Mott excitons. This is in agreement with Kabler and coworkers [40], who strode to reveal the dependency of the lifetime on excitation density. They used 75 ps long pulses in one set-up and 5 ns pulses in another, but did not report any differences of pump efficacy and they only present results for the 5 ns laser pulses.

A further indication for this mechanism is that pumping is not as efficacious using pulses with 100 ps duration and 2.33 eV photon energy at the same fluence. It is unlikely that the small difference in photon energy is responsible for this effect. The very weak signal above 2.33 eV confirms that the absorption of two pump photons and one probe photon is unimportant at this intensity. This is in agreement with the observation of Eklund and coworkers [44] that 2.33 eV photons are 8 times less readily absorbed than 3.49 eV photons at such low intensities as offered by a thermal tungsten light source.

A smaller part of the signal in 3.5 is generated by populated higher excitons which decay into the lowest singlet exciton at 1.7 eV. This is indicated by the fact that the

3 Two-photon photoemission on fullerite films

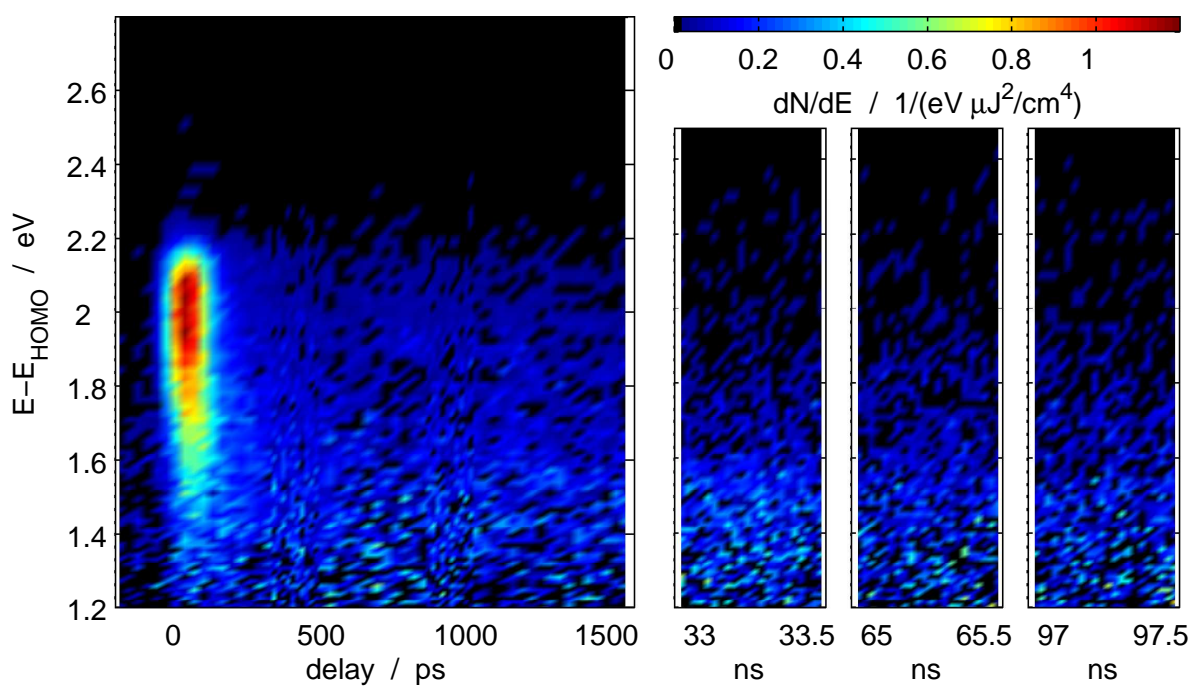


Figure 3.5: Pump pulse duration: 100 ps, pump photon energy: 2.35 eV (λ : 527 nm), probe photon energy: 5.88 eV (λ : 211 nm).

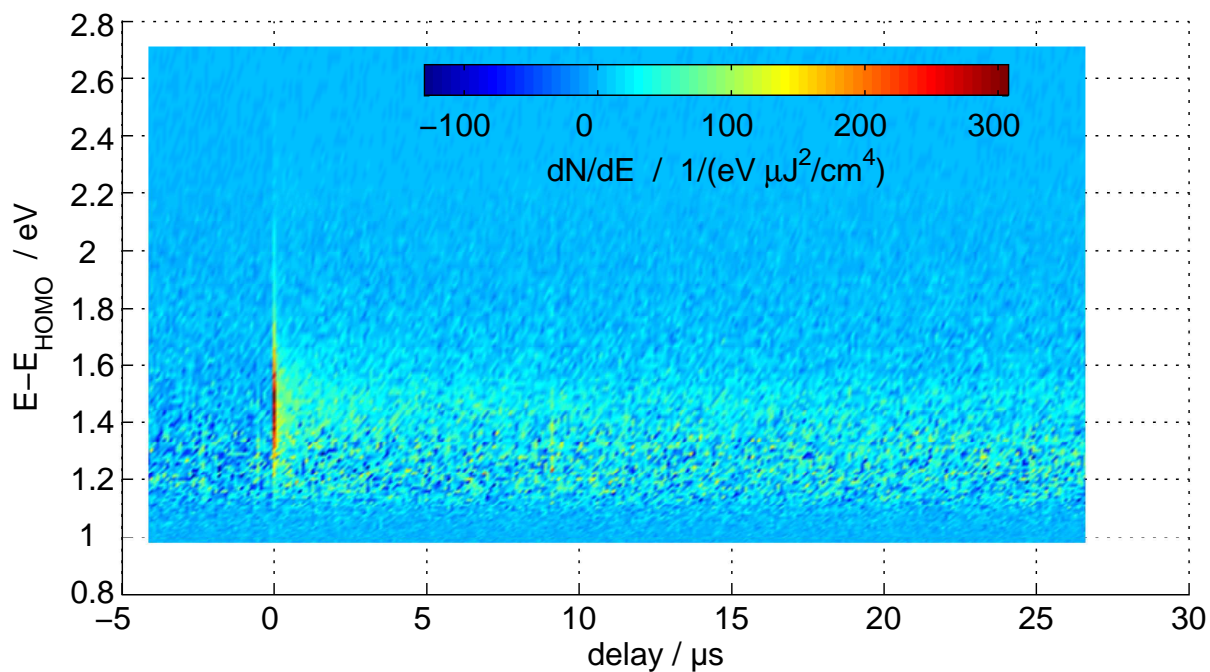


Figure 3.6: Pump pulse duration: 100 ns , pump photon energy: 3.50 eV (λ = 355 nm) , probe photon energy: 5.88 eV (λ = 211 nm).

maximum of the signal at that energy is delayed 30 ps with respect to the signal at an energy of 2.1 eV. This exciton has a lifetime of 500 ps. That some of the radiation has to be absorbed linearly is obvious because absorption was already measured by means of thermal radiation [44], and the linear nature holds for all pulse energies used in the present investigation as verified by Kabler and coworkers [40].

However, even 97.5 ns after pumping a dynamic spectrum is measured. A very low background appears in the dynamic spectra taken before the pump pulse which shows that the background subtraction works fine and that there are no excitation pathways where the role of the pump and the probe are interchanged.

Figure 3.6 shows a time-delay spectrum taken with a pump photon energy of 3.49 eV and a probe photon energy of 5.88 eV. The pump pulse lasts 100 ns, which is as long as the complete range of delays in figure 3.5. It shows delays up to 25 μ s. At zero delay the spectrum extends from 1.1 eV to 2.5 eV. A state at delays up to 4 μ s and an initial electron energy of 1.5 eV is interpreted as the triplet exciton. Additionally a non-decaying signal extends from 1.1 eV to 1.4 eV. This is further analysed in figure 3.28 and in figure 3.17.

An alternative explanation [11] based on measurements which show no energetic shift is that this state decays by exciton-exciton reaction, which leads to hyperbolic state dynamics. A bi-exponential decay is observable in some measurements in the present investigation, but hyperbolic state dynamics is never observable. Thus, this alternative explanation can be discarded for the present investigation.

3.3 Warm preparation

3.3.1 Singlet exciton

The singlet exciton is investigated using the opto-mechanical delay and varying the photon energy. For each measurement a fluence histogram across all pump fluences is derived and the signals are sorted according to the laser fluences into above, below, and median pump fluences.

Typical results are shown in figures 3.7– 3.10. The photon energy $h\nu$ is 3.06 eV ($\lambda = 405.0$ nm) and the temperature T is 140 K. Two states, the lowest triplet exciton (3E), and the singlet exciton (1E) can readily be observed.

In figure 3.7 the dynamic spectra of the lowest triplet exciton are smooth, at least above 1.4 eV. The upper tenth-maximum (TM) of the peak of the lowest triplet exciton is at 2.6 eV while in the other measurements of this series the upper TM

3 Two-photon photoemission on fullerite films

is at 2.3 eV. In figure 3.8 the fit to the state dynamics results in lifetimes above 3 ns. Since the maximum measured delay is 0.45 ns, no upper limit for the lifetime uncertainty can be given. A low population data point in the low energy data corresponds to a high population data point in the high energy data and *vice versa*.

In figure 3.9 the dynamic spectrum of the singlet exciton has its upper TM at 2.1 eV, which is typical in this series. It extends down to the low energy cut-off of the time-delay spectrum. In figure 3.10 the state dynamics exhibits a lifetime shorter than the laser pulse length by more than a factor of ten, and no lower limit of the lifetime uncertainty can be given.

In the dynamic spectrum in figure 3.12 the lowest triplet exciton peaks at 1.4 eV and the singlet exciton exhibits a plateau extending from the low energy cut-off to 1.8 eV. In the state dynamics in figure 3.14 the singlet exciton has a lifetime shorter than the laser pulse duration and the lowest triplet exciton has a lifetime longer than the maximum delay.

In figure 3.13 the dynamic spectra of the lowest triplet exciton and the lowest singlet exciton increases monotonously towards lower energies. The excited singlet exciton peaks at 1.8 eV. In figure 3.15 the lifetime of the lowest triplet exciton is much longer than the maximum delay. The lowest singlet exciton has a lifetime of 210 ps. The lifetime of the excited singlet exciton is much shorter than the laser pulse duration.

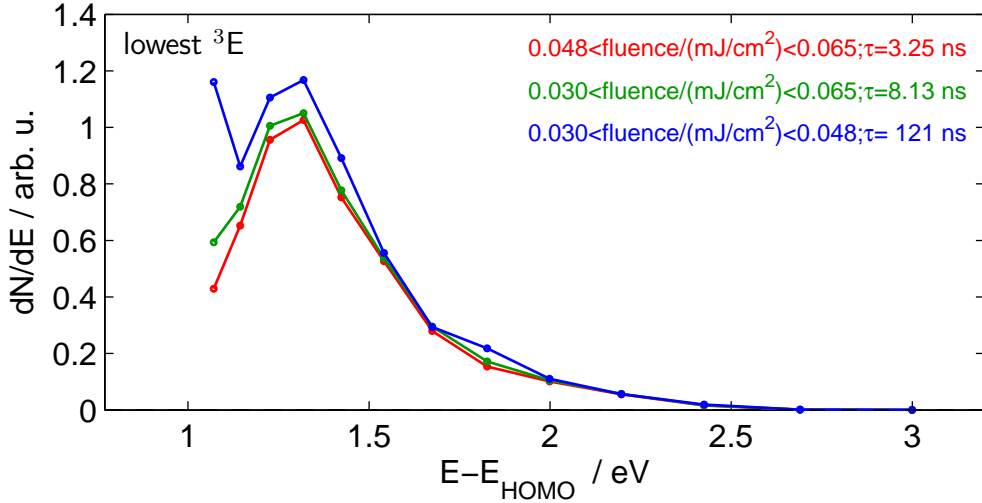


Figure 3.7: Typical dynamic spectra for the lowest triplet exciton. Pump photon energy: 3.06 eV ($\lambda = 405 \text{ nm}$). Probe photon energy: 5.88 eV ($\lambda = 211 \text{ nm}$).

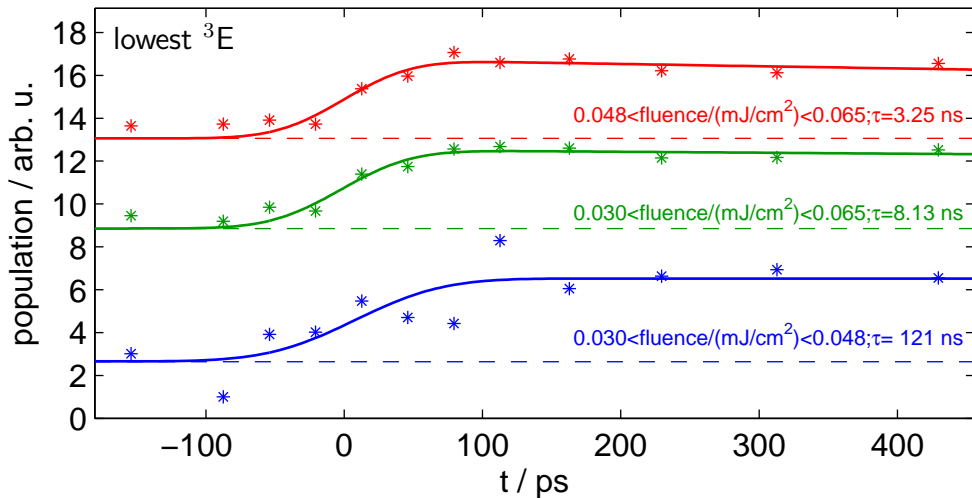


Figure 3.8: Typical state dynamics for the lowest triplet exciton. Pump photon energy: 3.06 eV ($\lambda = 405 \text{ nm}$). Probe photon energy: 5.88 eV ($\lambda = 211 \text{ nm}$).

3 Two-photon photoemission on fullerite films

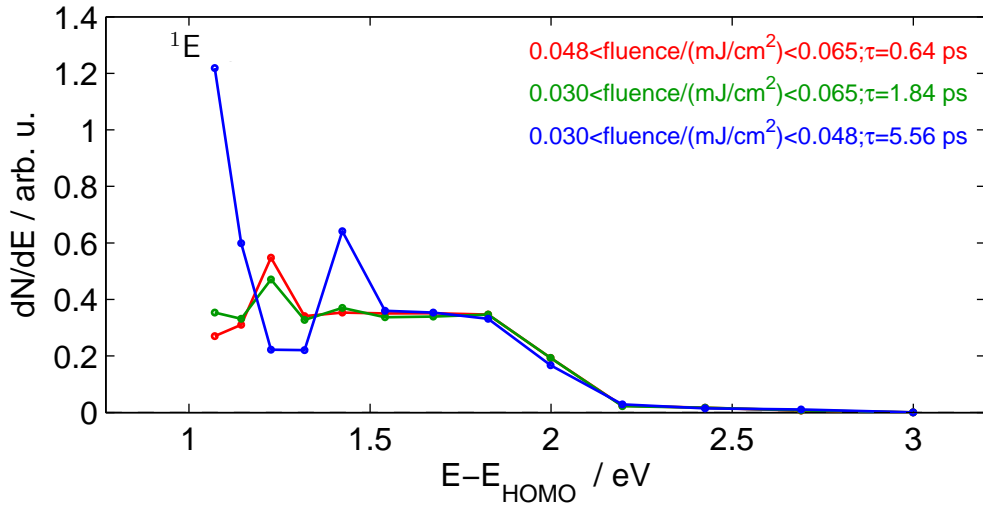


Figure 3.9: Typical dynamic spectra for the singlet exciton. It does not resolve between the lowest singlet exciton and the excited singlet excitons. Pump photon energy: 3.06 eV ($\lambda = 405$ nm). Probe photon energy: 5.88 eV ($\lambda = 211$ nm).

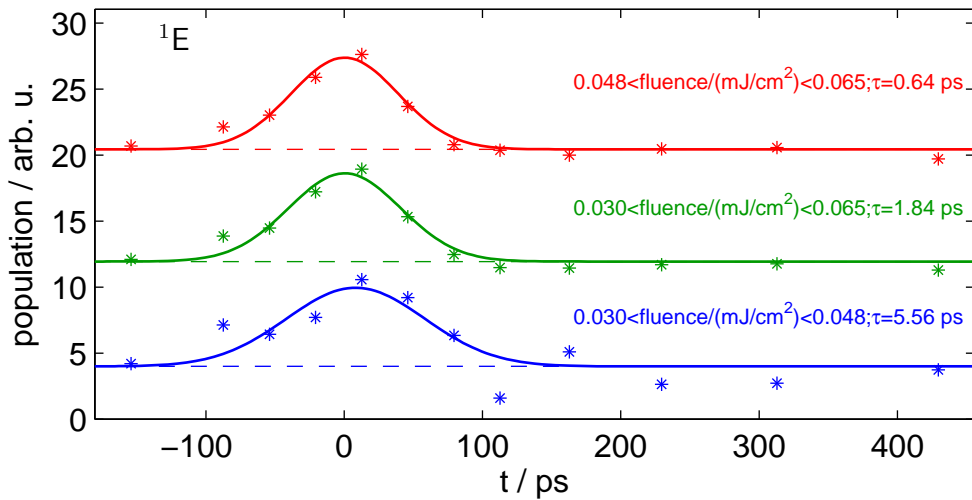


Figure 3.10: Typical state dynamics for the singlet exciton. It does not resolve between the lowest singlet exciton and the excited singlet excitons. Pump photon energy: 3.06 eV ($\lambda = 405$ nm). Probe photon energy: 5.88 eV ($\lambda = 211$ nm).

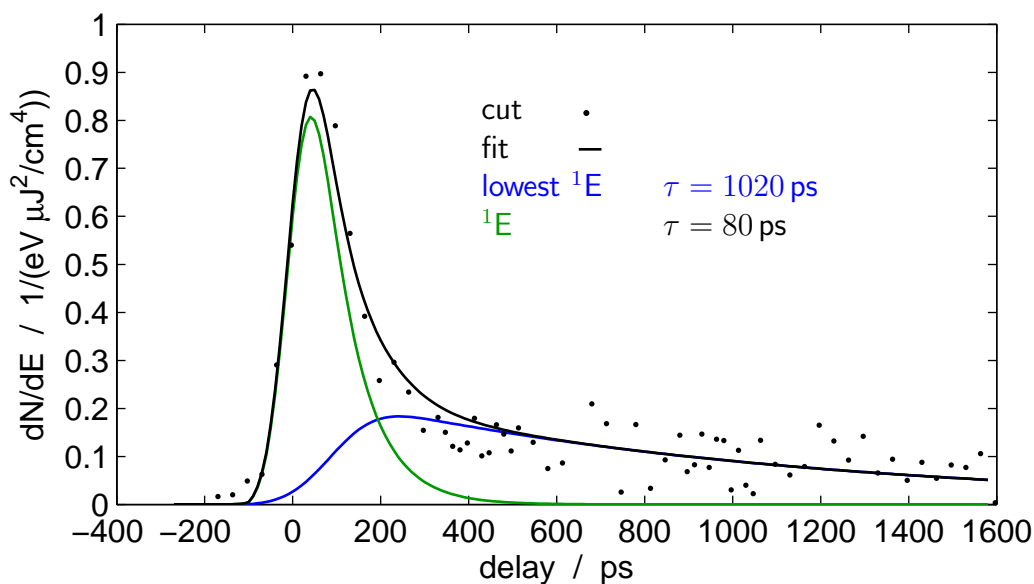


Figure 3.11: The 2PPE signal at 1.9 eV above HOMO in figure 3.5 (black dots) is fitted by a rate equation (black curve) with two states (blue and green), but without interstate rates. Pump photon energy: 2.35 eV ($\lambda = 527$ nm). Probe photon energy: 5.88 eV ($\lambda = 211$ nm).

In figure 3.11 the 2PPE signal at 1.9 eV above HOMO is fitted by a rate equation (marked as a black curve) with two states (marked as blue and green), but without interstate rates [104]. The lowest singlet exciton has a lifetime of 1020 ps. The excited singlet exciton has a lifetime of 80 ps.

From the time-delay spectrum in figure 3.5 dynamic spectra are extracted. They are shown in figure 3.16 and exhibit clearly separated peaks with a FWHM of 0.5 eV. The lowest triplet exciton is centred at 1.4 eV. The lowest singlet exciton is centred at 1.7 eV, which is somewhat lower than reported values for the singlet exciton of around 1.8 eV. The excited singlet exciton peaks at 2.0 eV, which is below reported values for free electrons in the LUMO of 2.2 eV. The dynamic spectrum is cut off at 2.35 eV, which is the pump photon energy used in this measurement.

The corresponding state dynamics in figure 3.17 shows a lifetime of the lowest triplet exciton, which is greater than the maximum delay of 97.5 ns. Any lifetime much longer than the maximum measured delay has a large uncertainty. Therefore, a longer electronic delay will be used in section 3.3.2. The lowest singlet exciton has a lifetime of 399 ps. The excited singlet exciton has a lifetime of 11 ps, which is below the laser pulse duration. In the case of the excited singlet exciton some crosstalk from the lowest singlet exciton is visible.

3 Two-photon photoemission on fullerite films

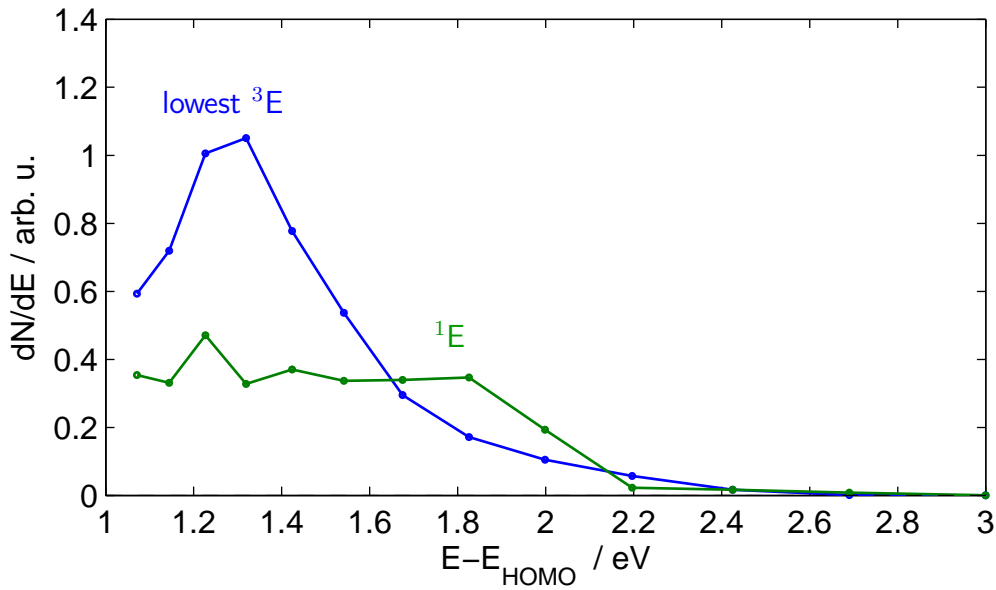


Figure 3.12: Pump pulse fluence integrated dynamic spectra. Pump photon energy: 3.06 eV ($\lambda = 405$ nm). Probe photon energy: 5.88 eV ($\lambda = 211$ nm). The blue curve represents the excitons and the green curve represents the free electrons in the LUMO band.

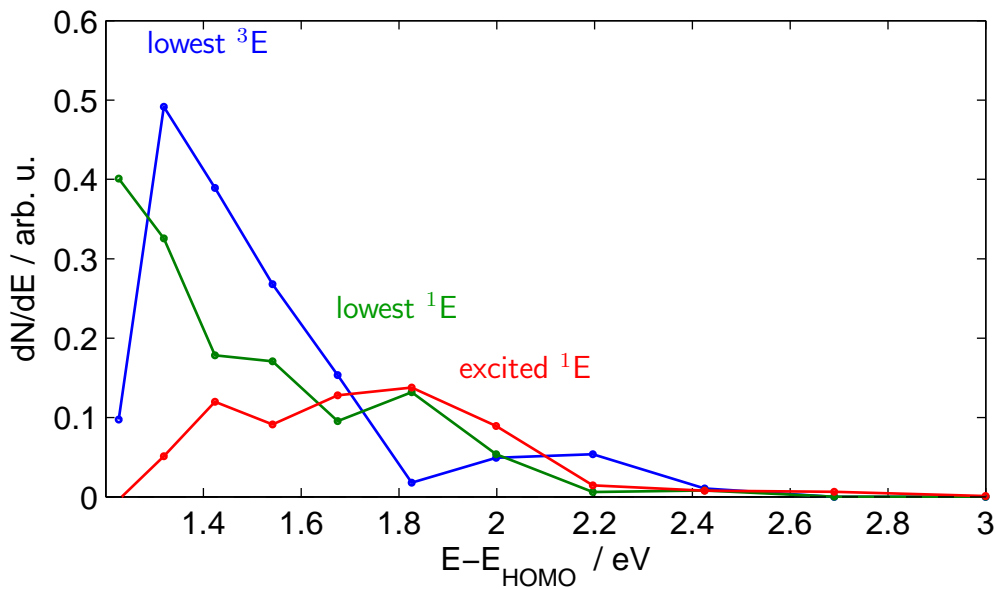


Figure 3.13: Pump pulse fluence integrated dynamic spectra generated from the same data as used for figures from 3.8 to 3.9. Pump photon energy: 3.18 eV ($\lambda = 390$ nm). Probe photon energy: 5.88 eV ($\lambda = 211$ nm). The blue curve represents the excitons and the green curve represents the free electrons in the LUMO band.

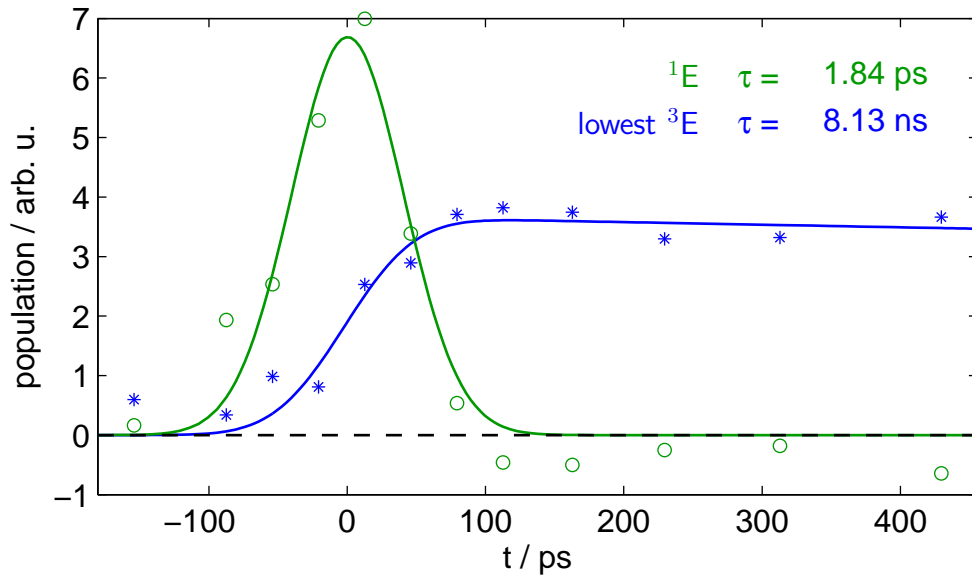


Figure 3.14: Pump pulse fluence integrated state dynamics generated from the same data as used for figures from 3.8 to 3.9 and 3.12. Pump photon energy: 3.06 eV ($\lambda = 405$ nm). Probe photon energy: 5.88 eV ($\lambda = 211$ nm).

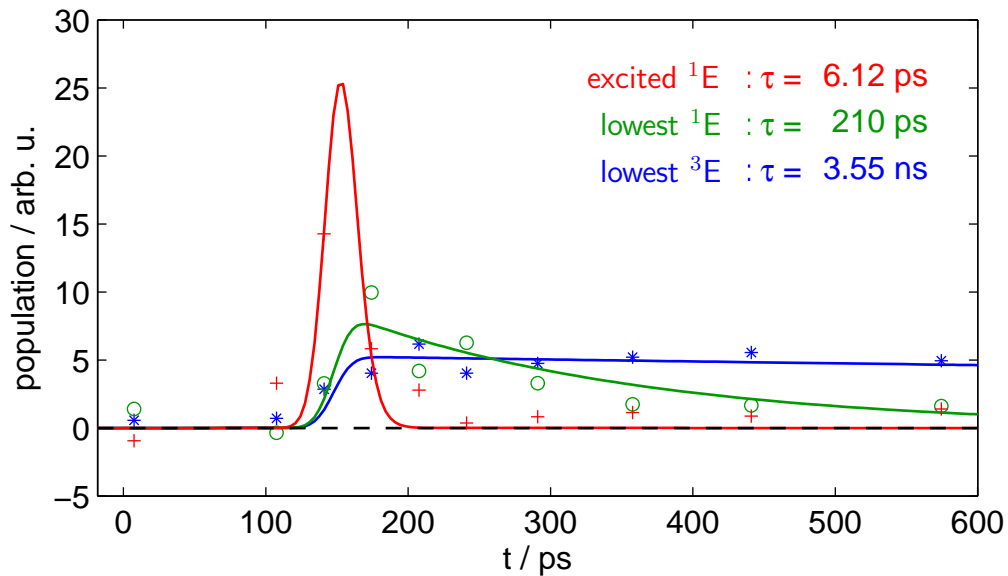


Figure 3.15: Pump pulse fluence integrated state dynamics extracted from the same data as used for figure 3.13. Pump photon energy: 3.18 eV ($\lambda = 390$ nm). Probe photon energy: 5.88 eV ($\lambda = 211$ nm).

3 Two-photon photoemission on fullerite films

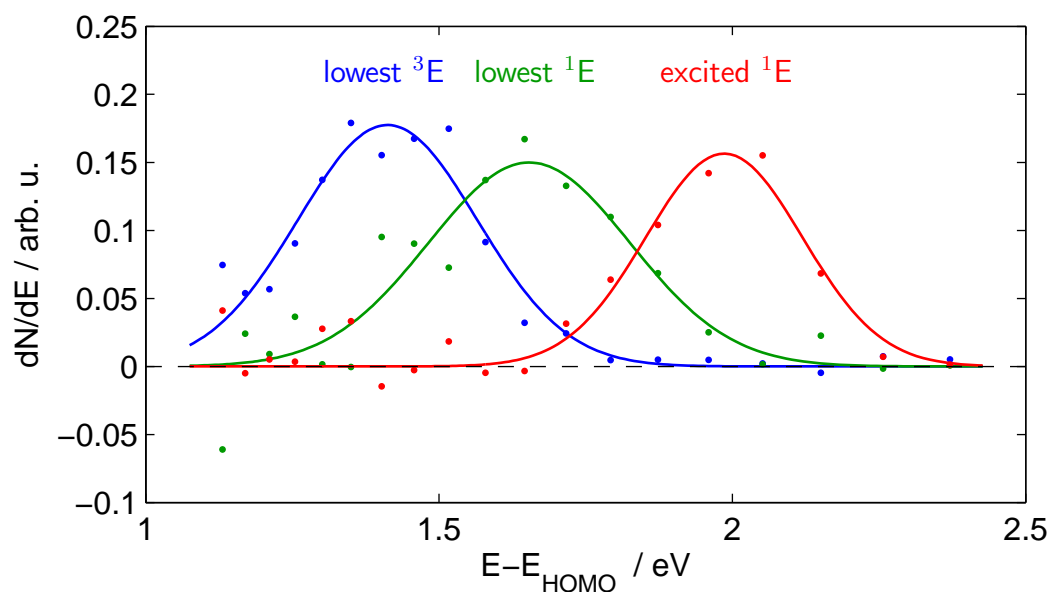


Figure 3.16: Dynamic spectra extracted from the same data as used for figure 3.5. Pump photon energy: 2.35 eV ($\lambda = 527$ nm) and a probe photon energy of 5.88 eV (211 nm). The curves are Gaussian curves fitted to the data.

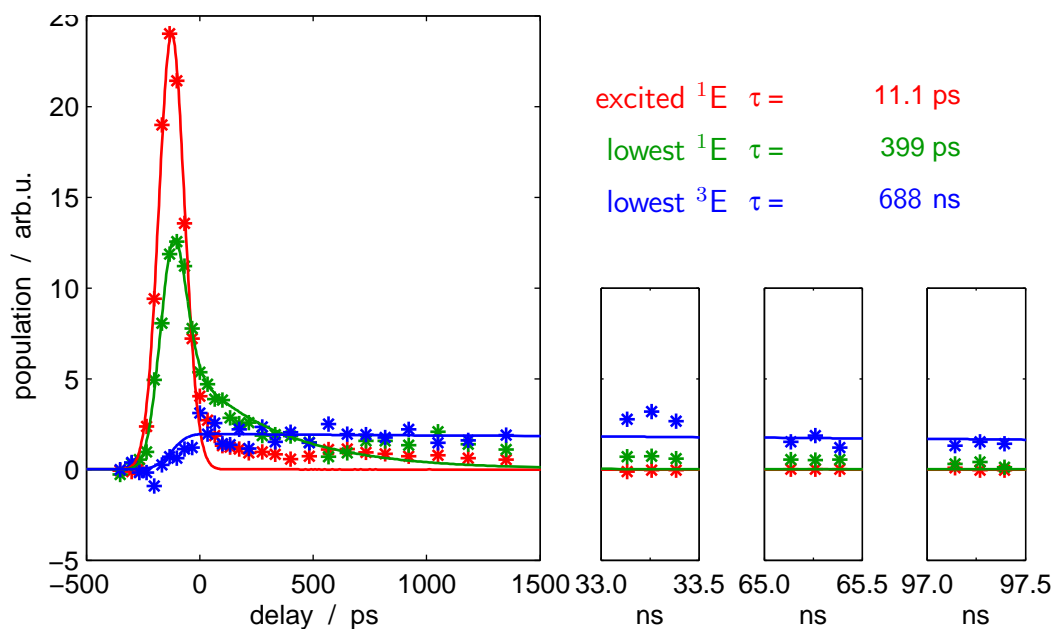


Figure 3.17: State dynamics extracted from the same data as used for figure 3.5. Pump photon energy: 2.35 eV ($\lambda = 527$ nm) and a probe photon energy of 5.88 eV (211 nm).

3.3.1.1 Efficacy and lifetime dependencies

Various time-delay spectra using different pump photon energies are measured. The lifetimes derived from the time-delay spectra are analysed by means of SVD and by means of a cut. Both results are plotted as a function of the pump photon energy in figure 3.19 and 3.20. In case of the SVD the efficacy is the peak height of the curve given by fitted rate equation, while in case of the cut the height at zero delay is used. The dependence of the excitation efficacy on the pump-photon energy is also plotted and saturation effects due to a high pump pulse fluences are analysed. In the measurements by Eberhardt and coworkers [39] the time-resolved 2PPE clearly shows a decay from the LUMO+1 into the LUMO within 1 ps. This is about 100 times faster than the laser pulse duration in this investigation, but might be visible in the time-delay spectra if the signal to noise ratio also exceeds 100.

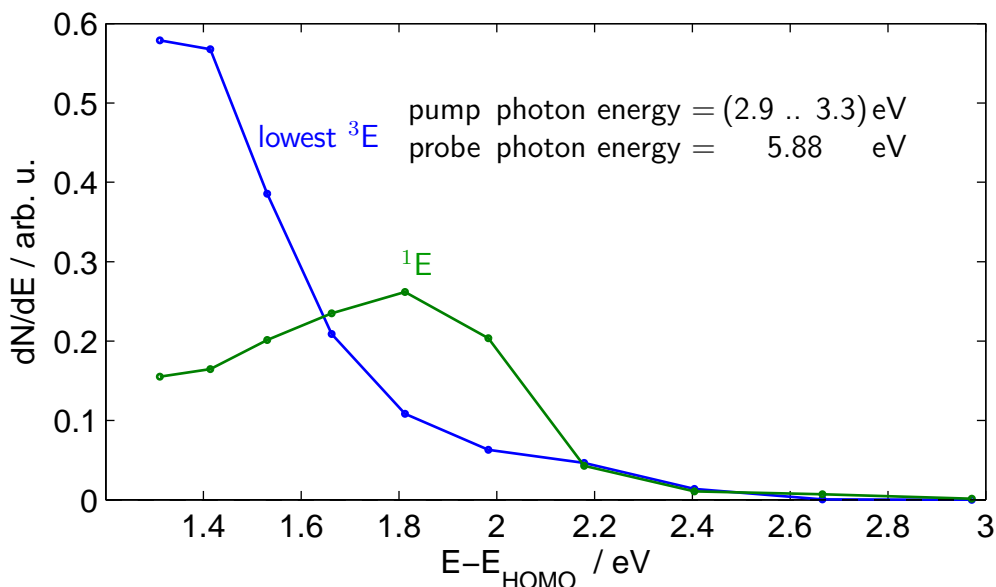


Figure 3.18: Mean dynamic spectra generated by SVD measured with mechanic delay.

The mean dynamic spectra derived from the time-delay spectra from which the values for figure 3.20 are extracted are shown in figure 3.18. The centre of the lowest triplet exciton lies below 1.4 eV and the singlet exciton is centred around 1.8 eV and reaches up to 2.8 eV, where the exciton with an electron in the LUMO+1 is expected. From the lifetimes of figure 3.20 one may conclude that the lowest triplet and the lowest singlet exciton are not separated perfectly.

3 Two-photon photoemission on fullerite films

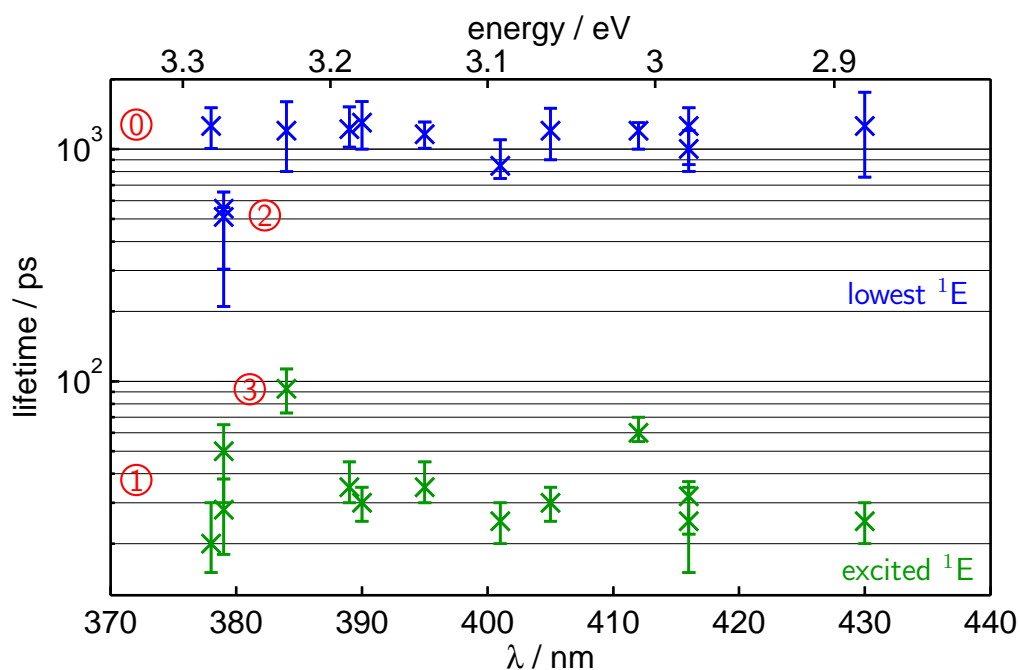


Figure 3.19: The 2PPE signal at 1.9 eV above HOMO fitted by a rate equation with the two states lowest singlet exciton (lowest 1E) and excited singlet exciton (1E), but without interstate rates. The encircled numbers are explained in the text.

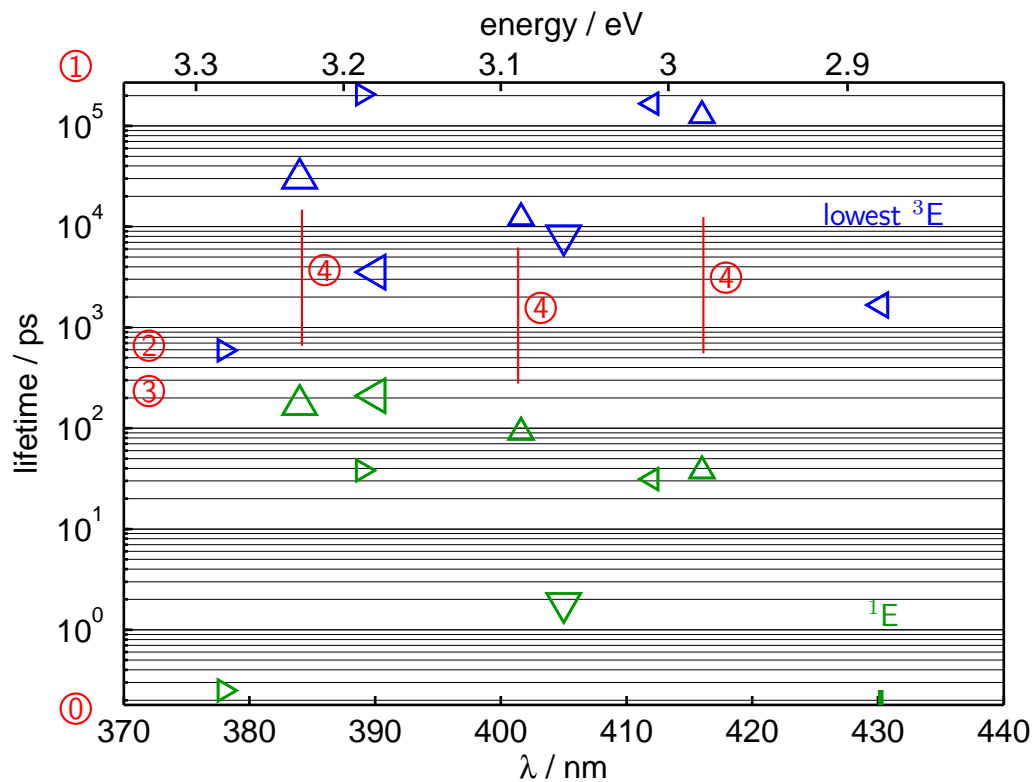


Figure 3.20: The 2PPE signal generated by means of the mechanic delay analysed by SVD and rate equation. The encircled numbers are explained in the text.

Figure 3.18 shows that the spectral overlap between the lowest triplet exciton and the singlet exciton is about 50 % and the SVD still manages to separate these states so clearly that a factor of 10 between the lifetimes of the lowest triplet exciton and the singlet exciton results.

In figure 3.19 for each pump photon energy the 2PPE signal at 1.9 eV above HOMO is fitted by a rate equation with two states (lowest singlet excitation and excited exciton), but without interstate rates. Lifetimes for the lowest singlet exciton are above 0.8 ns and around 1.2 ns ①, and lifetimes for the excited singlet exciton are below 60 ps and around 37 ps ②. As exceptions to this the lowest singlet exciton at 378 nm has a short lifetime of 550 ps ③, and the singlet exciton at 384 nm has a long lifetime of 94 ps ④.

In figure 3.20 the results of the SVD-based analysis of the same data are shown. Lifetimes below 0.18 ps, which is far below the laser pulse duration of 120 ps, are cut off. ①. Lifetimes above 270 ns, which appear as a horizontal line in the state dynamics, are also cut off ②. The lifetimes for the lowest triplet exciton are above 600 ps ③. The lifetimes for the singlet exciton are below 200 ps ④. In each time-delay spectrum the lowest triplet exciton lives at least 10 times longer than the singlet exciton ⑤. Only a very weak correlation to the preparation, which is marked by the direction of the triangle, is observed.

Comparing figure 3.20 to figure 3.19 it can be concluded that the concentration on a small part of the spectrum around 1.9 eV reduces the influence of the short living excited singlet excitons and the influence of the long living trapped excitons on the results. At the same time this means that each time-delay spectrum recorded using the electronic delay always has to be analysed into three states. By coincidence, in section 3.3.2.1 a method is introduced, which is more immune against noise, but also more biased. Three states would be in agreement with Eberhardt and coworkers [39], though they did not clearly separate the triplet exciton and use a different state assignment for the states with lifetimes similar or shorter than the laser pulse duration.

In figure 3.21 the 2PPE signal is integrated over the energy range of LUMO and LUMO+1, respectively, and is plotted against the pump photon energy. The probe photon energy is 4.71 eV ($\lambda = 263$ nm). This data is not used for any other analysis in this investigation, because no time resolution is visible. Different symbols mark different preparation runs. All preparations follow the same recipe. For each preparation run a non-stop series of up to three 2PPE measurements with

3 Two-photon photoemission on fullerite films

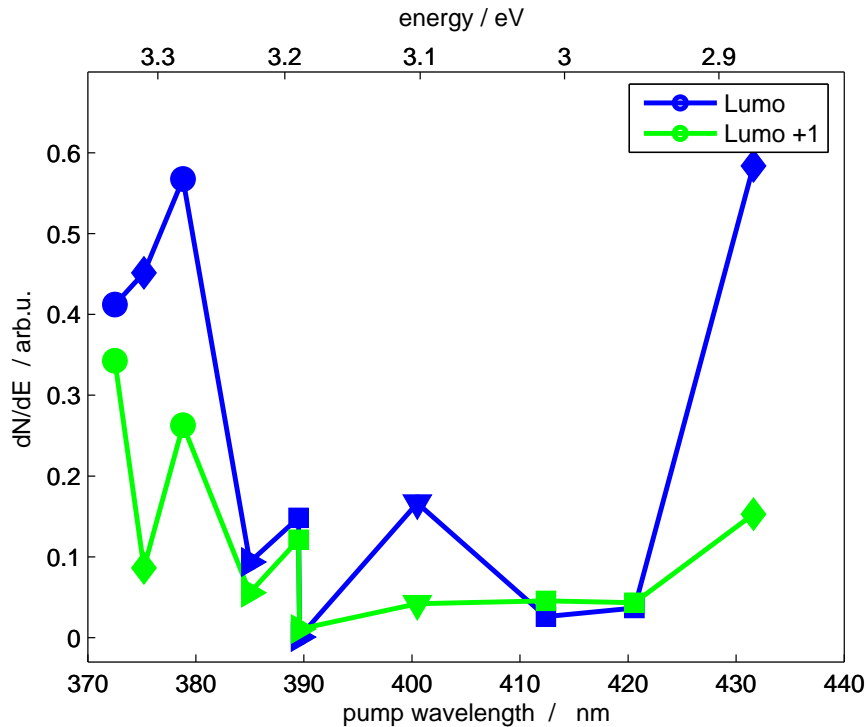


Figure 3.21: The efficacy extracted from the 2PPE signal integrated over the energy range of the excited singlet exciton (1E) and excitons with an electron in the LUMO+1, respectively. The probe photon energy is 4.7 eV ($\lambda = 263$ nm). Different preparations are marked by different symbols.

multiple different pump photon energies is carried out. An increase of the efficacy below 390 nm pump wavelength is visible, which is in agreement with absorption measurements [59].

In figure 3.22 the pump pulse fluence amounts to 0.4 nJ/cm^2 and the probe photon energy amounts to 5.88 eV (211 nm), which is also the case in all remaining figures in this section. The 2PPE signal is again integrated over the energy range of LUMO and LUMO+1, respectively, and is plotted against the pump wavelength. The intensity of the pump laser beam amounts to $50 \mu\text{J/cm}^2$. The large variation in measurements with 5.88 eV probe photon energy were not expected as the variation is small in the 8.24 eV UP spectra used to check each preparation.

The analysis by a cut is shown in figure 3.22 and analysis by SVD is shown in figure 3.23. Considering the rather strong effects due to different preparations the excitation efficacy does not depend on the pump photon energy. Extreme values correlate with low quality raw data.

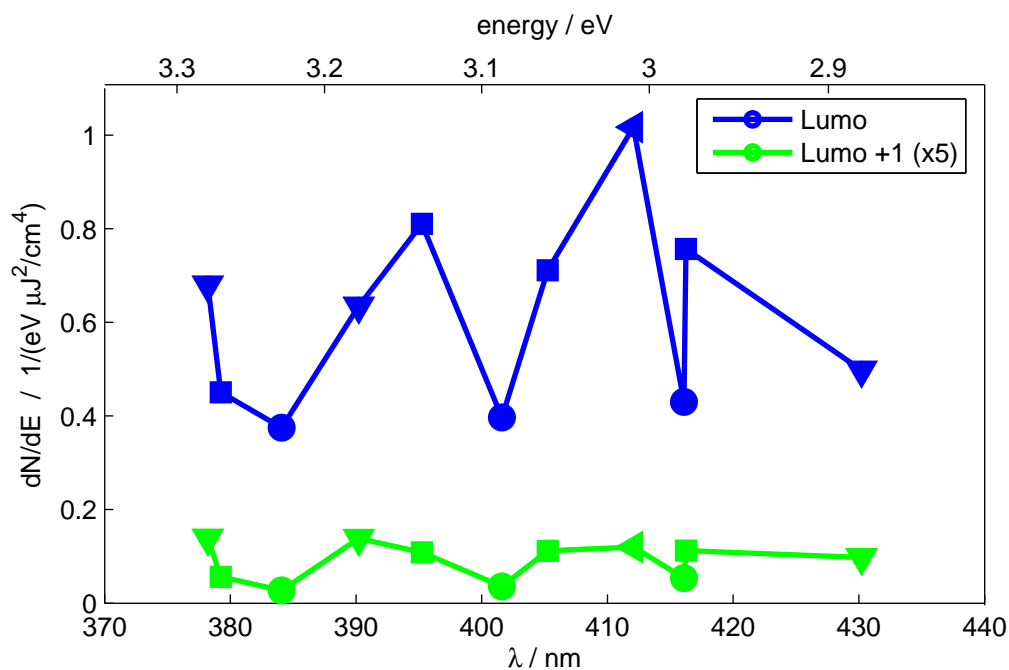


Figure 3.22: The efficacy extracted from the 2PPE signal integrated over the energy range of the excited 1E and excitons with an electron in the LUMO+1, respectively. Probe photon energy: 5.88 eV ($\lambda = 211$ nm). Different symbols mark different preparations.

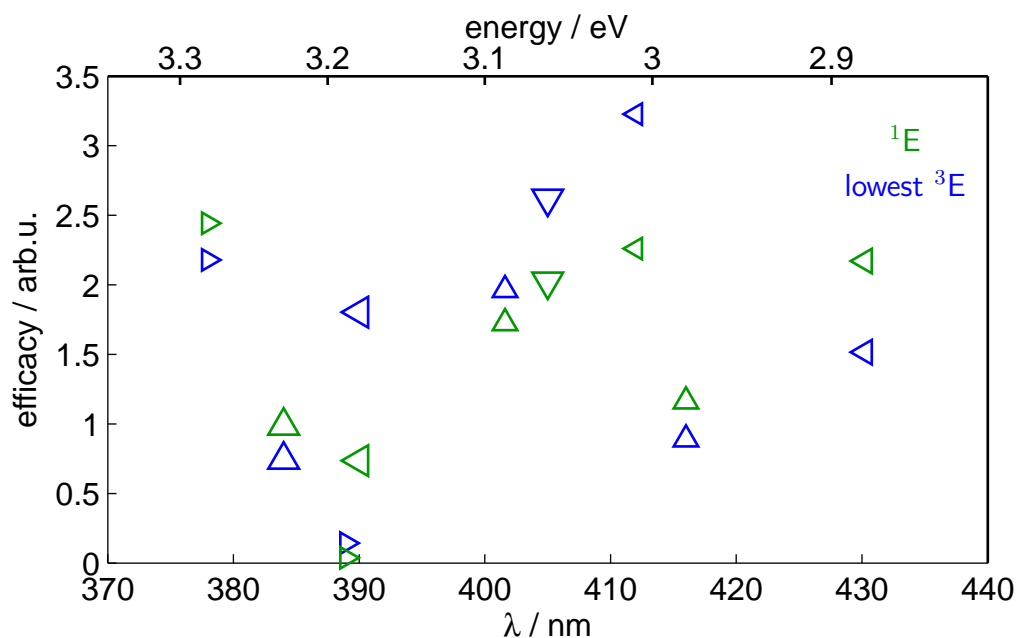


Figure 3.23: Analysis of the efficacy by SVD and rate equation. The probe photon energy is 5.88 eV ($\lambda = 211$ nm). Different symbols mark different preparations..

3 Two-photon photoemission on fullerite films

In figure 3.24, if examining each preparation independently, the lifetime of the singlet exciton decreases with increasing pump pulse fluence for all but one measurement. Within a single adjustment of the laser set-up the relative pump pulse fluence variation amounts to less than 20%. A measurement done at higher fluences supports the decrease of the lifetime of the singlet exciton with increased pump fluence. It can be concluded that already at a fluence of 0.05 mJ/m^2 singlet-singlet annihilation occurs, which is in agreement with Kabler and coworkers [11], where below 0.1 mJ/m^2 already a slight decrease of the lifetime was determined. In figure 3.25, if examining each preparation independently, the efficacy of the singlet exciton decreases with increasing pump pulse fluence for all but two measurements. Since some lifetimes are shorter than the duration of the laser pulse, the efficacy is reduced. This effect would be absent, if the efficacy is defined more theoretically as the rate $r_{1,0}$ in equation 1.1. This effect is almost invisible in the photon energy dependence figures in this section.

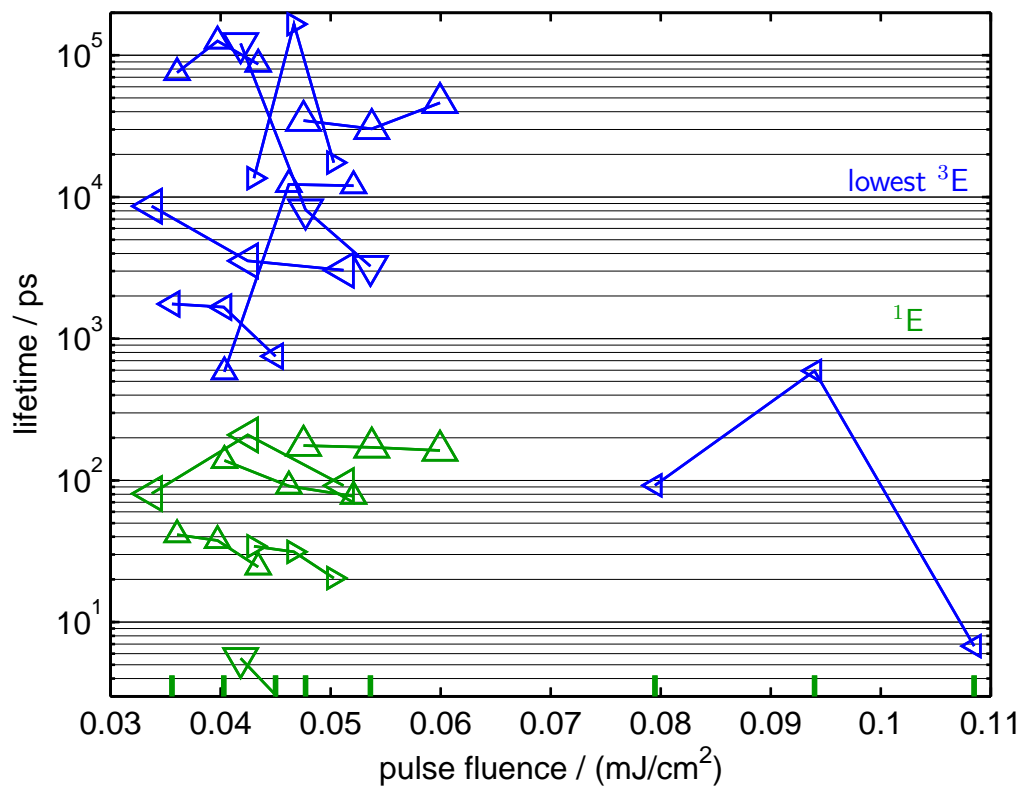


Figure 3.24: Mechanic delay analysed by SVD and rate equation. Different symbols mark different preparations.

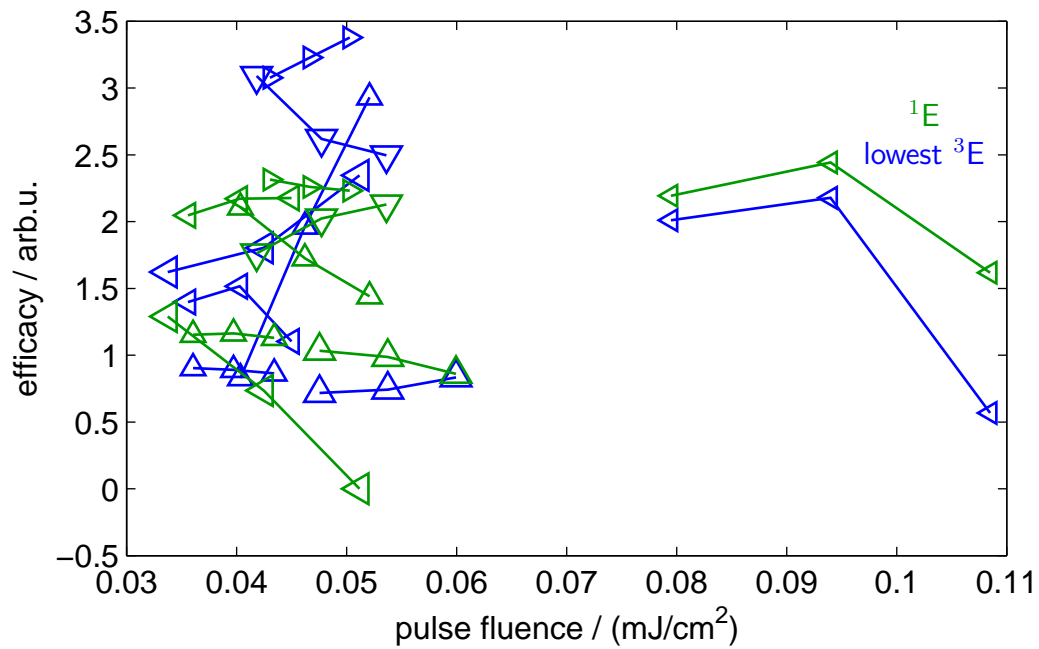


Figure 3.25: Mechanic delay analysed by SVD and rate equation. The signal is normalized by the pulse fluence. Different symbols mark different preparations.

3.3.1.2 Interstate rate

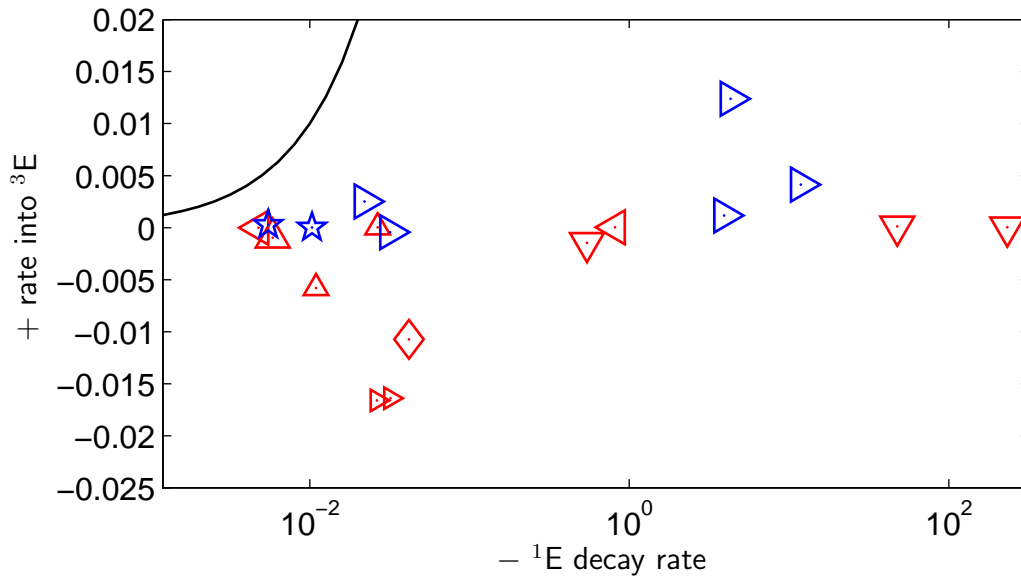


Figure 3.26: The interstate rate (growth rate of ^3E induced by the population in ^1E) obtained from the fit. For comparison the decay rate of ^1E is plotted on the x-axis. Cold preparations are marked blue, warm preparations are marked red. The black line is a theoretical curve based on a simple model, which assumes that ^1E decays into ^3E . This model does not agree with the experiment.

In figure 3.26 the interstate rates from the rate equation ($R_{n,m} \wedge n \neq m$) fits are plotted. Generally the rates do not meet the theoretical curve. This curve is derived from the assumption that the lowest singlet exciton decays exclusively into the lowest triplet exciton. The fitted interstate rates are too small to account for the decay in the lowest triplet exciton going so far that some interstate rates are negative. Consulting equation 1.1 this does not imply that the electron population flows upwards in energy. Instead it may be interpreted as an induced decay by a scattering of free particles in fullerite as introduced in section 1.1.3. Small rates with the right sign can be explained by a different efficacy of the photoemission from both states, especially because one state is partly cut off. In this case the real interstate rates are larger. Due to the preparation it could be that the underlying copper shortens the lifetime of almost every state except triplet excitons trapped on the surface and thus only two types of states are visible: trapped and free. This would also explain the spectral width of the singlet exciton in many time-delay spectra.

3.3.1.3 Comparison with the literature and conclusions

The results of the current investigation are now compared to the measurements by Eberhardt and coworkers [39], who used pump pulses with a duration of 150 fs and a photon energy of 3 eV. In their dynamic spectra Gaussian peaks with FWHM of 0.5 eV and only very little noise are visible. The energetic positions of the peaks are in accordance with 2PPE literature. The exciton with an electron in the LUMO+1, the excited singlet exciton, and the lowest singlet exciton can be assigned to these peaks. Gaussian curves are fitted to the peaks to obtain the state dynamics. Sample charging is included by shifting the whole dynamic spectrum.

In the present investigation the measurement is performed on a cooled sample, thus no photopolymerization is expected. The lowest singlet exciton is found at 1.8 eV with a lifetime of 1020 ps in good agreement with Eberhardt and coworkers [39] (1.8 eV, 998 ps). For the excited singlet exciton an energy of 2.1 eV above HOMO and a lifetime from 30 to 40 ps is measured. In separate measurements with higher intensities the exciton with an electron in the LUMO+1 is visible at 2.8 eV and the exciton with an electron in the LUMO+2 is visible at an energy of 4.0 eV above (HOMO). In both investigations, the present and the one by Eberhardt and coworkers, a background of scattered photoelectrons appears in the dynamic spectra near the low energy cut-off. The background is proportional to the integral photoemission which itself is largest at zero delay.

In some time-delay spectra the lowest singlet exciton is missing. The reason may be that the more mobile singlet excitons drift into the copper. Analogously Zhu and coworkers [41] reported increased decay rates for LUMO+1 and LUMO+2 excitons, if less than 5 ML are prepared. Kabler and coworkers [40] reported that pulse fluences above 0.1 mJ/cm² lead to shorter lifetimes of the lowest singlet exciton. This effect could be relevant for the LUMO already at about 40 μ J/cm², due to the higher mobility, though no corresponding fluence dependence is observed. Furthermore the excited singlet exciton may have a larger probe efficacy ($r_{2,1}(t)$ in equation 1.1).

In agreement with photoabsorption measurements by Eklund and coworkers [44] the pump efficacy measured in the current investigation is very low at 2.4 eV (517 nm), is low and constant in the range from 2.9 to 3.3 eV (from 428 to 376 nm), and high at 3.5 eV (354 nm). The likely reason is that the transition from the HOMO to the LUMO+1 (2.8 eV) is just below and the transition from HOMO-1 into the LUMO (3.3 eV) just above the investigated range of energies.

3.3.2 Triplet exciton

The triplet exciton is visible with both delay lines (electronic and mechanic), the lifetime is measured exclusively by means of the electronic delay. The delay step duration of 100 ns is predetermined by the available electronics. The pump laser pulse duration also is about 100 ns depending on power and adjustments. The triplet exciton lives much longer than the laser pulse duration. Like in the opto-mechanic delay measurements the SVD is used to separate a single time-delay spectrum into multiple state dynamics with their respective dynamic spectra. This will be shown in detail for the time-delay spectrum in figure 3.6.

The extracted dynamic spectra are shown in figure 3.27. For the trapped triplet exciton the dynamic spectra extends from 1.1 eV up to 2.4 eV TM with the main part between 1.2 eV and 1.5 eV. The high energy tail can be explained by high lying traps. The free triplet exciton extends from 1.1 eV to 1.8 eV TM with the main part energetically above the trapped triplet exciton. The dynamic spectrum of the singlet exciton dominates around 1.8 eV. Like in the measurements using the mechanic delay the short living state extends down to the low energy cut-off. This may be due to the background mentioned in section 1.2.1. The signal at the energy of the LUMO of 2.2 eV is one 50th of the signal at the singlet exciton energy. Apparently, after excitation with 3.49 eV (355 nm) the LUMO+1 directly decays into the singlet exciton. The lifetimes of the LUMO+1 and to a lesser degree of the LUMO are much shorter than the singlet exciton lifetime, thus they are additionally suppressed in the dynamic spectrum.

In figure 3.28 the state dynamics of the trapped triplet exciton has a baseline at negative delays with a height of 0.2 times the height at large positive delays. This shows the quality of the background subtraction in the analysis. The trapped triplet exciton does not decay in the period of 25 μ s scanned after excitation. This is consistent with 400 μ s lifetime measured by EPR. The free triplet exciton does have a measurable lifetime of 5.0 μ s which is rather short for a triplet exciton. The singlet exciton is only populated at zero delay and the following two time slots. Regarding the set-up the concentration of the signal at a single delay shows that the pulse duration and also the overall jitter are below the delay step size.

From figure 3.6 three states can be extracted. From other measurements in this series only two states can be extracted due to noise. In figure 3.28 the area below the state dynamics of each triplet state is larger than the area below the singlet exciton state dynamics. Thus the two dominant states are the triplet excitons. The SVD

automatically extracts these from the other time-delay spectra and mostly ignores the singlet exciton. The remaining influence by the singlet exciton is further reduced by simply ignoring delays shorter than 400 ns for the lifetime fit.

The pulse fluence is chosen so that in accordance with literature only marginal triplet-triplet quenching occurs and appropriately the state dynamics is singly exponential and cannot be fitted better by including triplet-triplet exciton annihilation [11, 104]. This is verified for all measurements using the electronic delay.

3 Two-photon photoemission on fullerite films

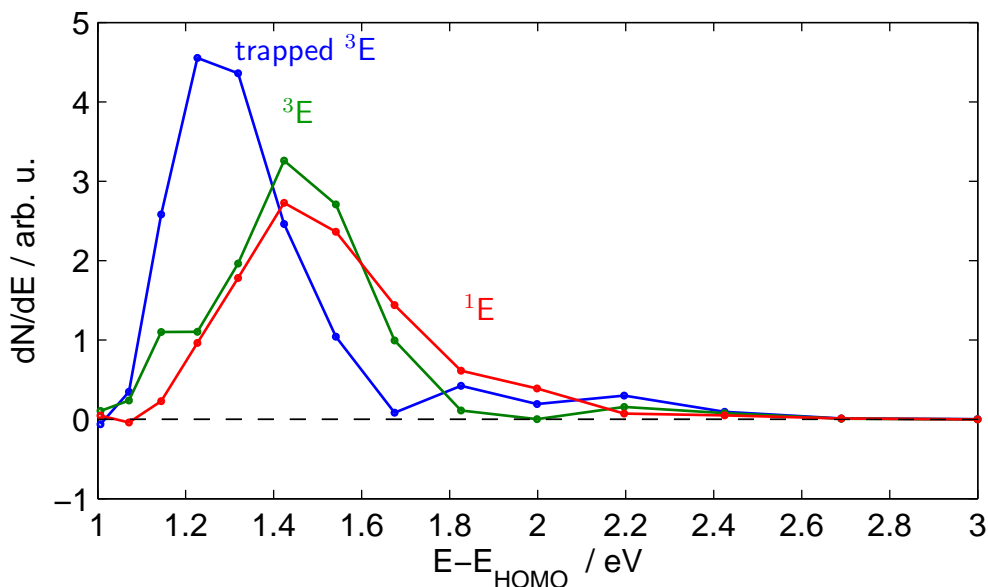


Figure 3.27: The dynamic spectra of three states extracted from a single time-delay spectrum (figure 3.6) using the electronic delay. Pump photon energy: 3.49 eV (355 nm). Probe photon energy: 5.88 eV ($\lambda = 211$ nm). Temperature: 140 K.

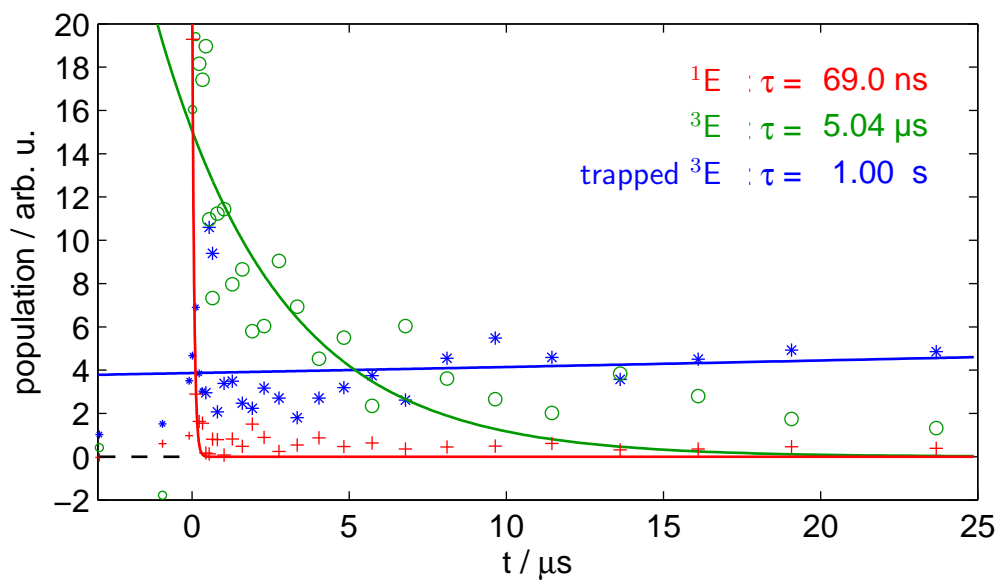


Figure 3.28: The state dynamics of three states extracted from a single time-delay spectrum (figure 3.6). Pump photon energy: 3.49 eV (355 nm). Probe photon energy: 5.88 eV ($\lambda = 211$ nm). Temperature: 140 K.

3.3.2.1 Dependence on film thickness and temperature

To measure the mobility of the triplet exciton, preparations of different thickness (from 9 to 17 ML) are compared. Due to the slow intrinsic decay of the triplet exciton electron-phonon coupling is expected to be relevant. Therefore, the triplet decay is measured at different sample temperatures. Reducing the pressure of liquid nitrogen for the chiller allows the sample to heat up from 140 K to 300 K over a period of 10 hours.

In figure 3.29 the thickness of the fullerite film is varied from 9.7 ML to 19.3 ML. The measurements at 9.7 ML and at 13.7 ML have the lowest noise. The measurement at 10.7 ML does not allow to fit two triplet states. The data point at 19.3 ML is very uncertain and the mean lifetime thus probably too low. The lifetime of the trapped triplet exciton is doubled with increasing the number of MLs from 10 to 14. As was discussed in subsection 1.1.4, an increase in lifetime is expected because the additional decay into the copper substrate is hindered. This decay path is of similar importance as the intrinsic decay for both triplet excitons and it is thus concluded that the short living state also has a higher mobility. Considering the thicknesses from 9.7 ML to 16.6 ML and the uncertainty bars the lifetime of the trapped triplet exciton stays at $100 \mu\text{s}$ and the lifetime of the free triplet exciton stays at $3 \mu\text{s}$ (uncertainty probably underestimated).

In the future measurements on fullerite films with an even lower number of MLs need to be taken to see a clear reduction of the lifetime. Using larger delays it may be possible to reduce the uncertainty in the lifetimes measured on larger number of MLs and to more clearly resolve a saturation of the lifetime to the bulk value.

In figure 3.30 the efficacy seems to decrease with more MLs. This at least shows that there is no significant decrease in efficacy if the number of MLs is reduced down to 9 ML.

Time-delay spectra taken on a 12 ML thick film at two different temperatures are analysed. The fit yields a trapped tripped exciton lifetime of $94 \mu\text{s}$ at 140 K and of $47 \mu\text{s}$ at 290 K. In figure 3.31 the change of the lifetimes, when continuously increasing the sample temperature from 140 K to 295 K, is shown. A special analysis technique has to be employed because the measurements at intermediate temperatures suffer from noise due to the short measurement time and lack of experimental accuracy. Consequently larger uncertainty bars (in absolute numbers) are assigned to the data points at intermediate temperatures: Each intermediate time-delay spectrum is fitted by a linear combination of the already analysed time-

3 Two-photon photoemission on fullerite films

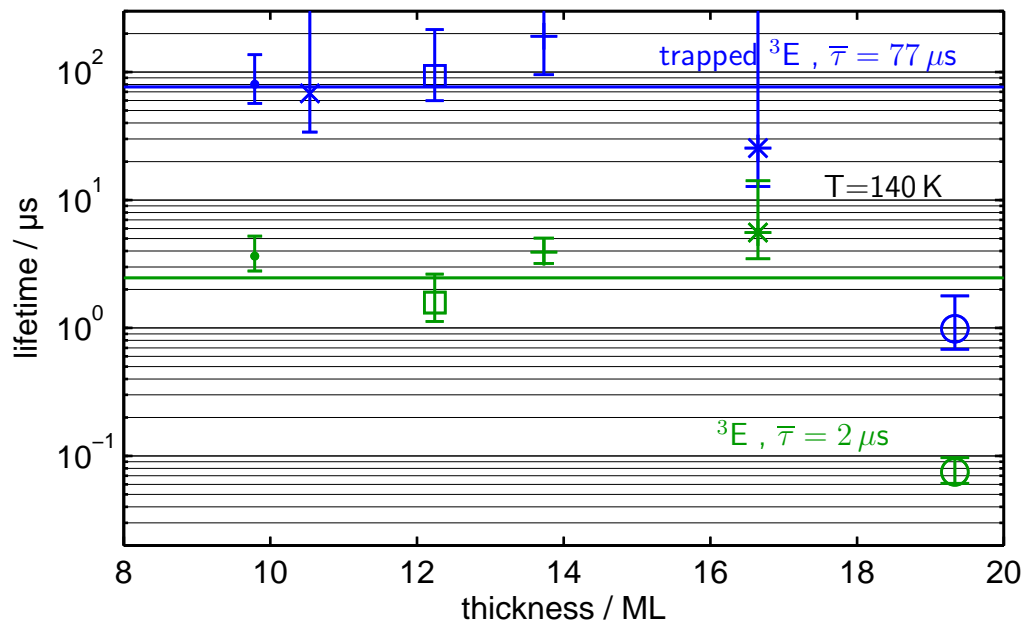


Figure 3.29: Lifetime dependence on thickness determined using SVD. Three error bars extend to extremely high values and are thus cut-off.

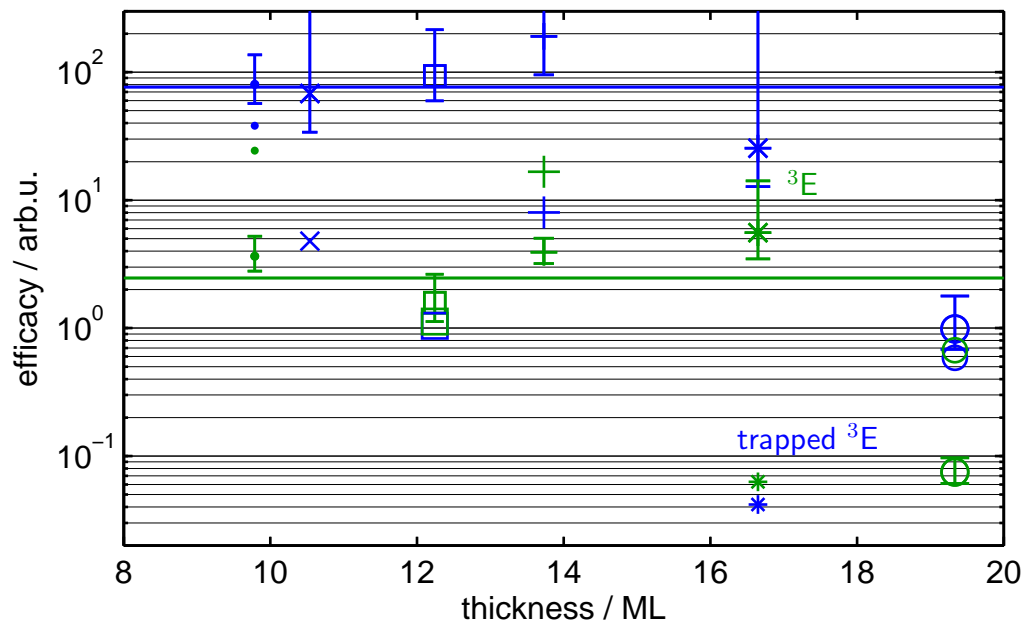


Figure 3.30: Efficacy dependence on thickness determined using SVD.

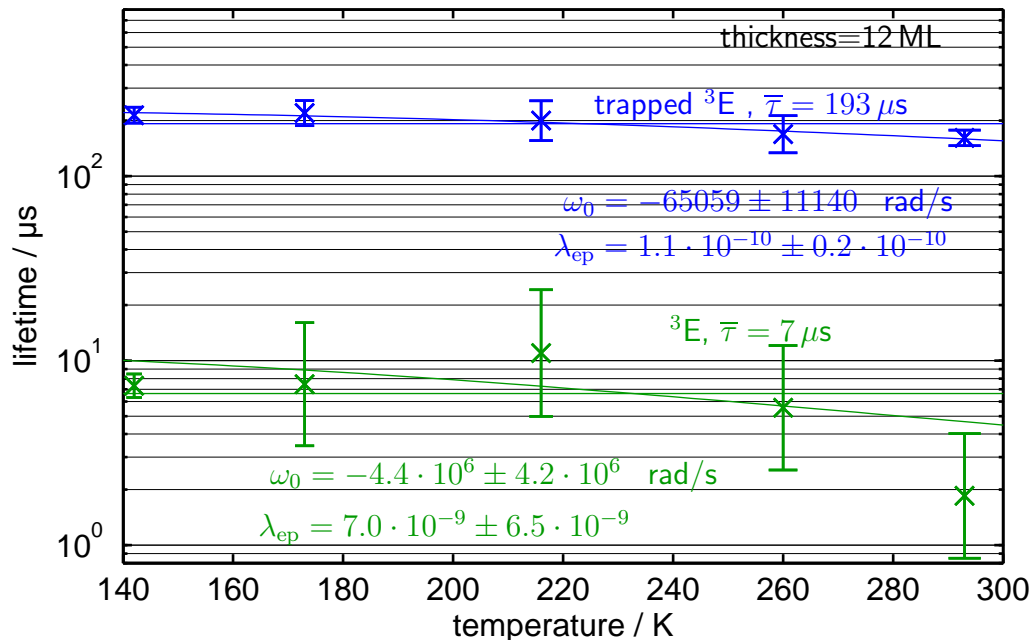


Figure 3.31: Lifetime dependence on sample temperature obtained by SVD.

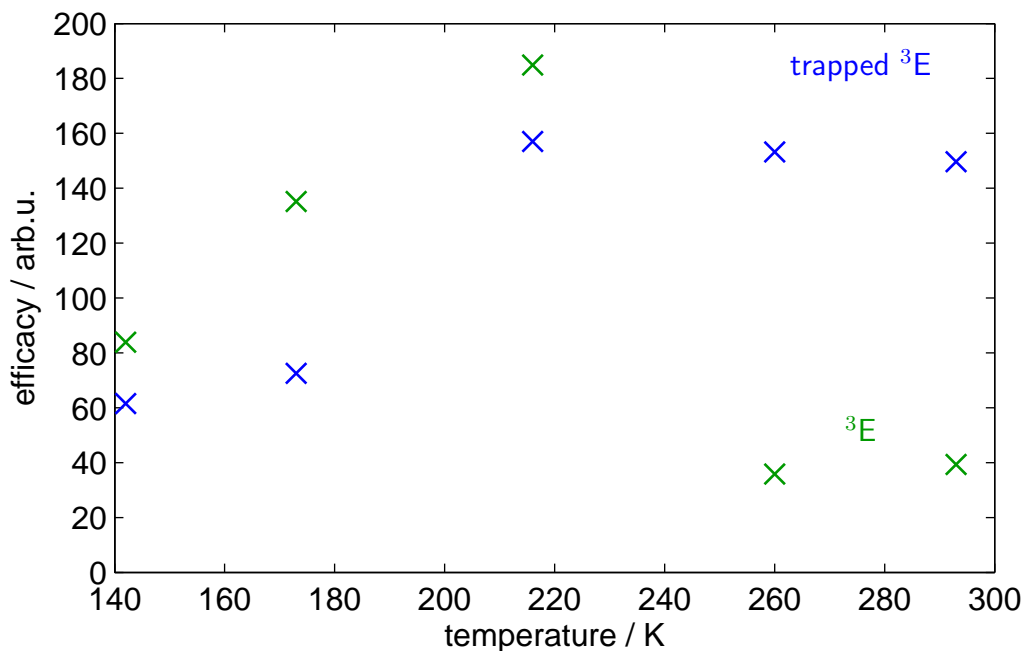


Figure 3.32: Efficacy dependence on sample temperature obtained by SVD.

3 Two-photon photoemission on fullerite films

delay spectra. The lifetime is then generated by linear combination using the same coefficients and shown in figure 3.31. As one result the trapped triplet exciton has a lifetime of $210 \mu\text{s}$ — the calculated lifetime has changed with the analysis method — and the free triplet exciton exhibits a lifetime of $7 \mu\text{s}$, both at 140 K. When increasing the sample temperature from 140 K to 260 K, a constant lifetime of $7 \mu\text{s}$ for the free triplet exciton and a constant lifetime of $193 \mu\text{s}$ for the trapped triplet exciton meet the uncertainty-bars. When further increasing the sample temperature to 295 K the lifetime of the free triplet exciton is reduced from $7 \mu\text{s}$ to $2 \mu\text{s}$ and the lifetime of the trapped triplet exciton is reduced from $193 \mu\text{s}$ to $160 \mu\text{s}$.

As discussed in section 1.1.3 the lifetime decrease may be due to electron-phonon coupling: a fit yields a very low coupling constant in the order of 10^{-9} and an unrealistic negative linewidth after subtraction of the electron phonon coupling. Alternatively, the decreased lifetime may be due to increase rotation of the molecules, or the measurement done on heating up to 295 K and the measurement at 295 K already polymerised the sample — which has not been cross-checked by any complementary method. This would lead to the reduced lifetime of $15 \mu\text{s}$ measured by Kabler and coworkers [40] on polymerised fullerite. The results on fullerite are in agreement with other measurements on C_{60} . From an article by Echt and coworkers [29] lifetimes of $47 \mu\text{s}$ and $28 \mu\text{s}$ for 140 K and 295 K respectively and can be extrapolated for free C_{60} from measurements above 600 K. From the review in an article by Campbell and coworkers [30] $94 \mu\text{s}$ and $54 \mu\text{s}$ can be extracted for 140 K and 295 K for isolated C_{60} , though no saturation of the lifetime down to 4 K is visible. Therefore the saturation in fullerite needs to be confirmed by measurements with delays even larger than $25 \mu\text{s}$.

The efficacy in figure 3.32 is so noisy that only general trends can be guessed: the efficacy of the trapped triplet exciton increases with temperature, while the efficacy of the free triplet exciton decreases. Theoretically the decrease of the lifetime of the free triplet exciton can be explained by an increased drift velocity, leading to a decay into the copper substrate and a more complete filling of all traps. Thus the number of trapped triplet excitons increases.

3.4 Cold preparation

By modifying the preparation method for the C_{60} film described in section 2.1 the electronic structure of the fullerite film can be influenced in a reproducibly. For the measurements presented so far the temperature is reduced to 360 K and then up to 20 ML are adsorbed onto the substrate. For the following measurements the temperature is reduced down to 300 K, which is referred to as “cold”, and then up to 20 ML are adsorbed onto the substrate.

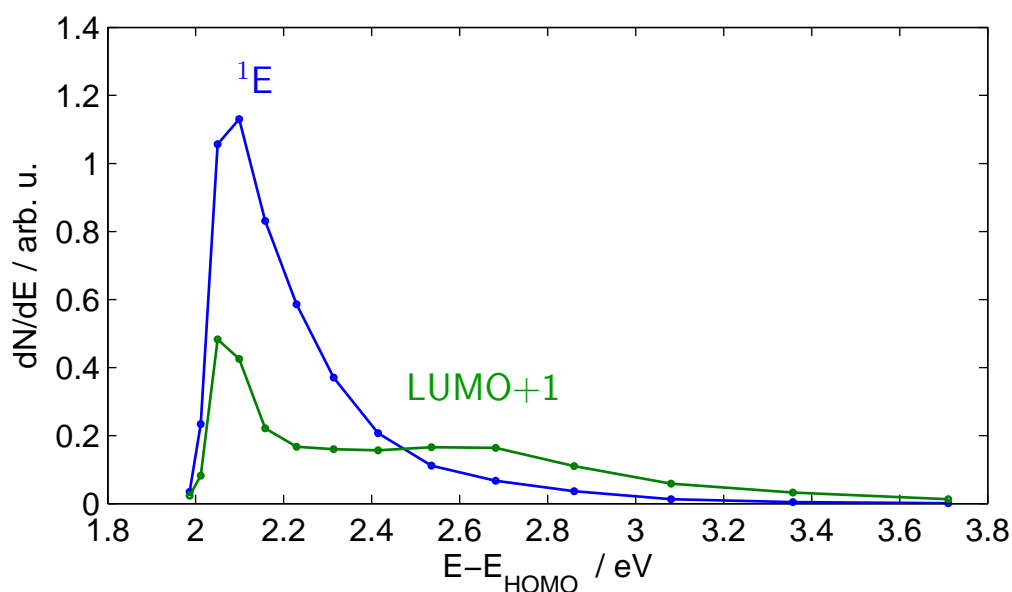


Figure 3.33: Mean cold preparation dynamic spectra. Probe photon energy: 4.71 eV.

The cold preparation is investigated using photons with 4.71 eV energy only. In figure 3.33 the average of the resulting dynamic spectra are shown. They are very stable across this series, thus taking the mean does not obscure any information. The singlet exciton is cut off at an energy of 2.1 eV and is the dominant state up to 2.5 eV. As shown in figure 3.34 it lives for typically 429 ps. The dynamic spectrum of the exciton having an electron in the LUMO+1 ¹ peaks at 2.8 eV. Due to scattering during the photoemission process the spectrum extends down to zero kinetic energy. Also around 2.3 eV the dynamic spectrum may be non-zero due to excited singlet excitons, which also have a lifetime shorter than the laser pulse duration.

Using the cold preparation the lowest singlet exciton is visible applying 4.71 eV photon energy. Theoretically this can be explained by traps. The lifetime could increase because deep traps are available and prevent the lowest singlet exciton from drifting into the copper substrate. The preparation does not influence the

¹whose lifetime is far below the laser pulse duration

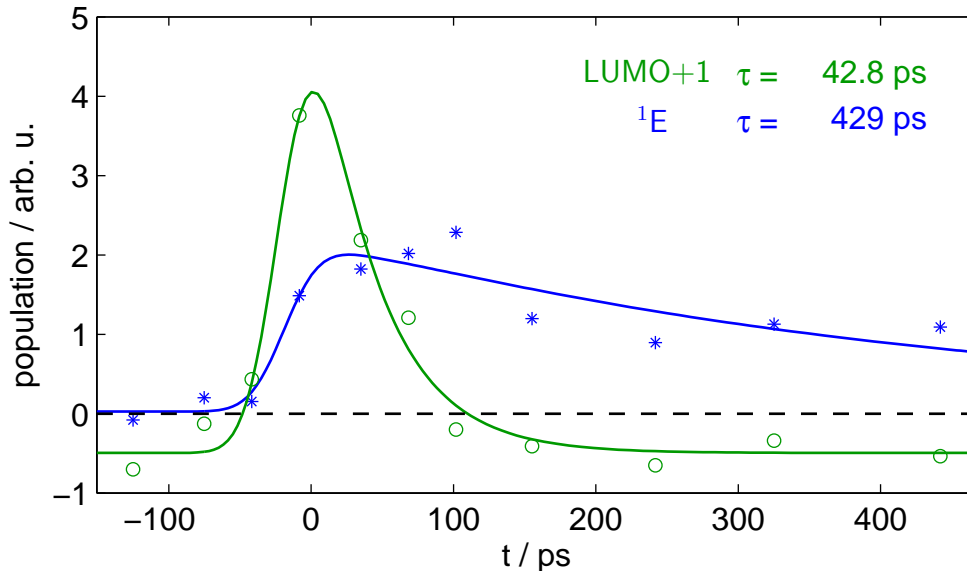


Figure 3.34: Typical state dynamics measured on the cold preparation analysed by SVD. Pump photon energy: 3.26 eV ($\lambda = 380.0$ nm). Probe photon energy: 4.71 eV.

excited singlet exciton. The fitted lifetime in figure 3.34 is, compared with the warm preparation and the values reported in the literature, slightly too short for the lowest singlet exciton and far too short for the triplet exciton. Thus it can be concluded that the traps do not increase the lifetime. Rather the binding of the hole to some traps is strong and can compensate anti-binding of the electron. This electron then appears at a higher energy in the spectrum.

On the cold preparation and using 4.71 eV probe photon energy a series of pump-probe measurements with various pump photon energies is performed, which is similar to the series with the warm preparation in figure 3.21.

For these measurements a slightly smaller range of delays is scanned. All measurements described in this section are done on the same preparation. There is no gradual decay over the measurements due to evaporation, polymerization, or contamination.

3.4.1 Efficacy dependence on photon energy

In figure 3.35 the result of the pump tuning is presented. At 380 nm and 387 nm the lifetime of the exciton with an electron in the LUMO+1 is only slightly below the laser pulse duration. At all other wavelengths the lifetime is cut off by the lower limit of the lifetime axis as marked by the small lines at the bottom of the figure. The reasons for the short lifetime at other wavelengths may be an inhomogeneous pump beam profile, which has a roughly doubled intensity in some spots, and a larger

pulse-to-pulse variance of the laser fluence. This reduces the lifetime of the excited singlet exciton. This in turn enhances the dominance of the LUMO+1 exciton in the time-delay spectrum. This in turn reduces the lifetime of the extracted state dynamics even more. As can be seen in figure 3.36 the long lifetime correlates with a high efficacy. Since the lifetime is shorter than the pulse duration, it is expected that the peak height of the Gaussian is approximately proportional to the lifetime. This already explains the variation of the efficacy and it can be concluded that excitation efficacy is constant across the scanned pump-photon energies.

3 Two-photon photoemission on fullerite films

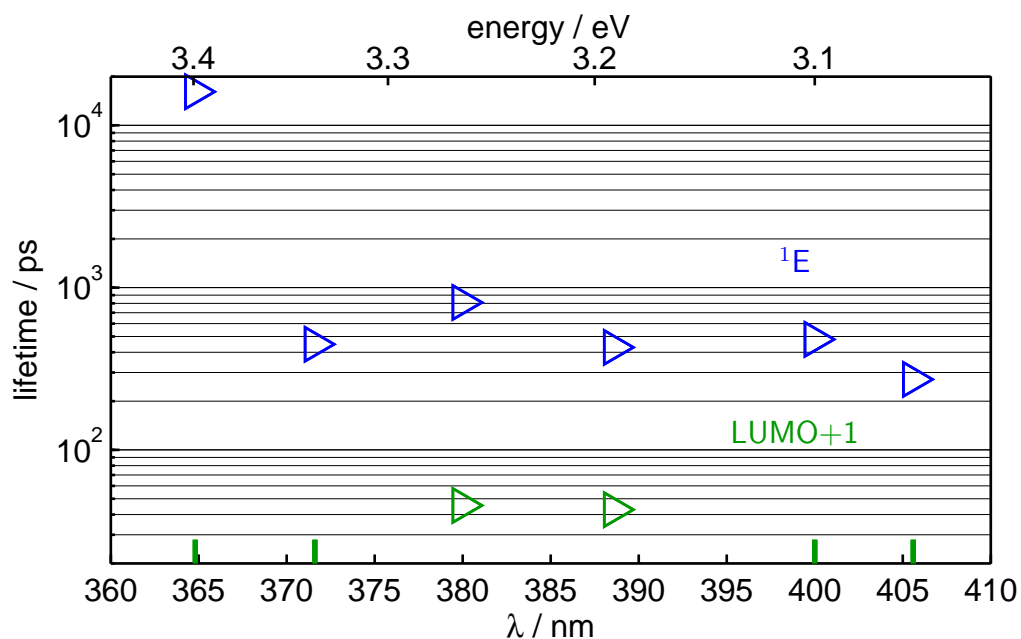


Figure 3.35: Lifetimes of the long living state on the cold preparation measured by the mechanical delay and analysed using the SVD. Some lifetimes are below 1 ps, thus they are below the time resolution of the measurement, and are cut off to not inflate the axis.

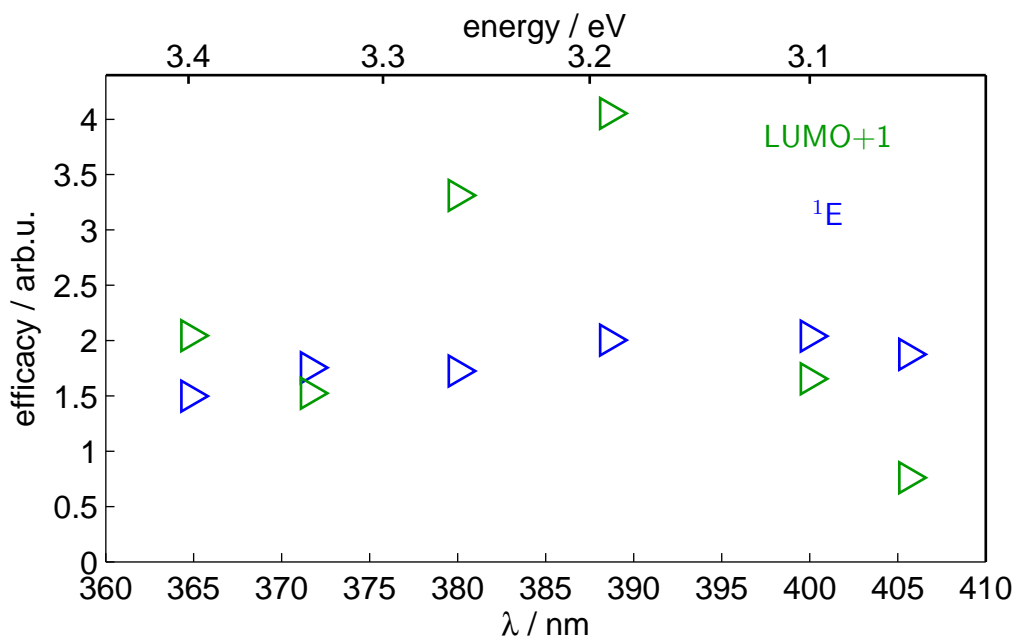


Figure 3.36: Efficacy of the state on the cold preparation measured by the mechanical delay and analysed using the SVD.

3.4.2 Improved beam overlap

The following two measurements with a slightly varied pump photon energy were performed in a second measurement campaign. Compared to the measurements on the cold preparation in section 3.4.1 the beam overlap is improved as discussed in section 2.3.1, but the preparation is nominally identical to that used in section 3.4.1. The evaporator is freshly filled and calibrated and the preparation is 20 ML thick. The lower noise allows to isolate three states, which are the lowest triplet exciton, the lowest singlet exciton, and collectively all higher excitons, which have lifetimes shorter than the laser pulse duration. On this good preparation and using a photon energy of 4.71 eV the background contributes only 1/4 to the measured spectrum at zero delay. Therefore, it is justified to measure the background in between the delay sweeps and to subtract the average from all delays. The sample is pumped with a fluence of 0.4 mJ/cm², which is rather strong compared to section 3.3.

As shown in figure 3.37 the triplet exciton has a positive TM at 2.5 eV, which is much higher than in other measurements or reported in the literature. This can be explained by hole traps and by the probe fluence, which in this measurements leads to significant mono-colour 2PPE out of the HOMO and thus also out of the triplet exciton. This dynamic spectrum is also cut off and may extend well down to lower energies. The singlet exciton dominates around 2.5 eV. The LUMO+1 dominates around 2.8 eV.

In figure 3.38 the lowest free triplet exciton has a lifetime of 6.06 ns. Considering that the largest applied delay is 400 ps, the real lifetime could be much larger. The singlet exciton has a lifetime of 182 ps. The decay is not very clearly separated from the decay of the other states, thus the lifetime has an uncertainty of about 30 ps. The high fluence may reduce the lifetime of the singlet exciton. The exciton with an electron in the LUMO+1 has a lifetime 8.37 ps. Considering the time resolution of the set-up, the uncertainty range is from 0 ps to 20 ps.

In figure 3.40 the triplet exciton has a lifetime of 40.7 ns, which is much larger than the maximum delay. The singlet exciton has a lifetime of 97 ps and dominates at a delay of 50 ps. The decay is not very clearly separated from the decay of the other states, thus the lifetime has an uncertainty of about 30 ps. The exciton with an electron in the LUMO+1 has a lifetime of 1 ps. As in the other measurements in this section the uncertainty range is from 0 ps to 20 ps.

In figure 3.39 all dynamic spectra show a low-energy cut-off at slightly higher energies compared to figure 3.38, possibly due to a higher work function of the specific preparation. All dynamic spectra increase monotonically towards lower energies. The dynamic spectrum of the lowest triplet exciton dominates below

3 Two-photon photoemission on fullerite films

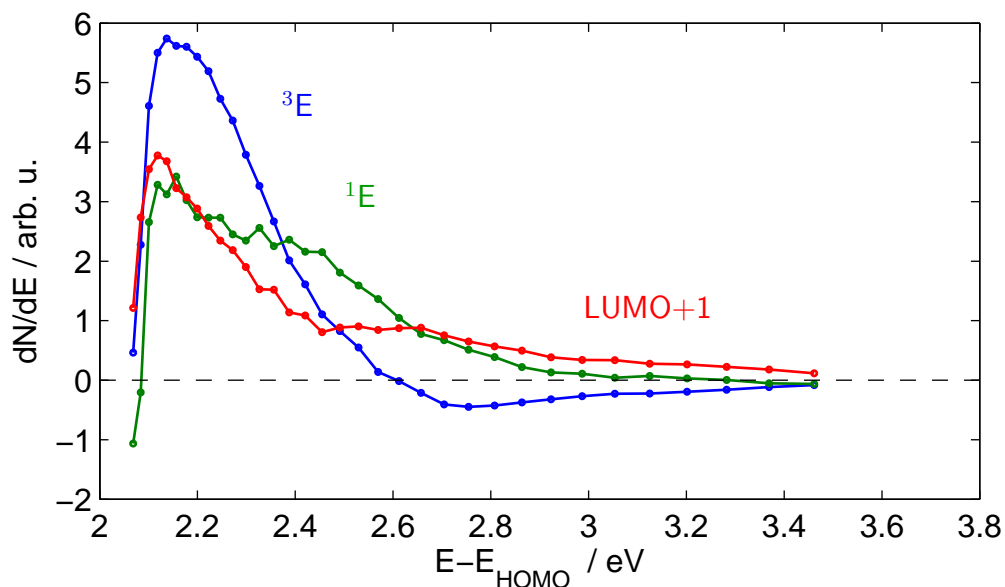


Figure 3.37: Cold preparation time-delay spectrum separated into three dynamic spectra. The corresponding state dynamics are shown in figure 3.38

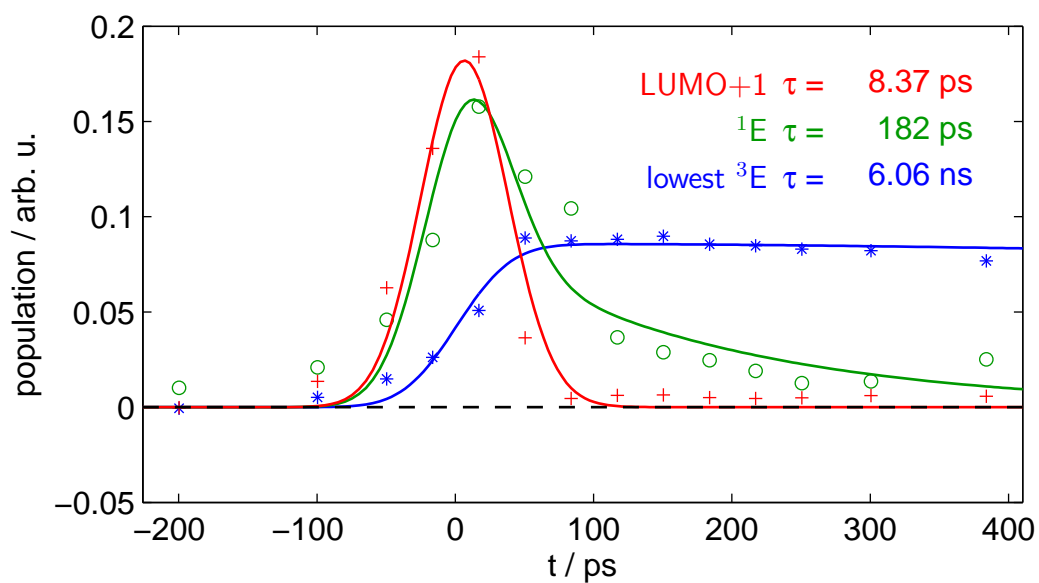


Figure 3.38: Cold preparation state dynamics. The corresponding dynamic spectra are shown in figure 3.37. Pump photon energy: 3.22 eV ($\lambda = 385$ nm). Probe photon energy: 4.7 eV ($\lambda = 263$ nm).

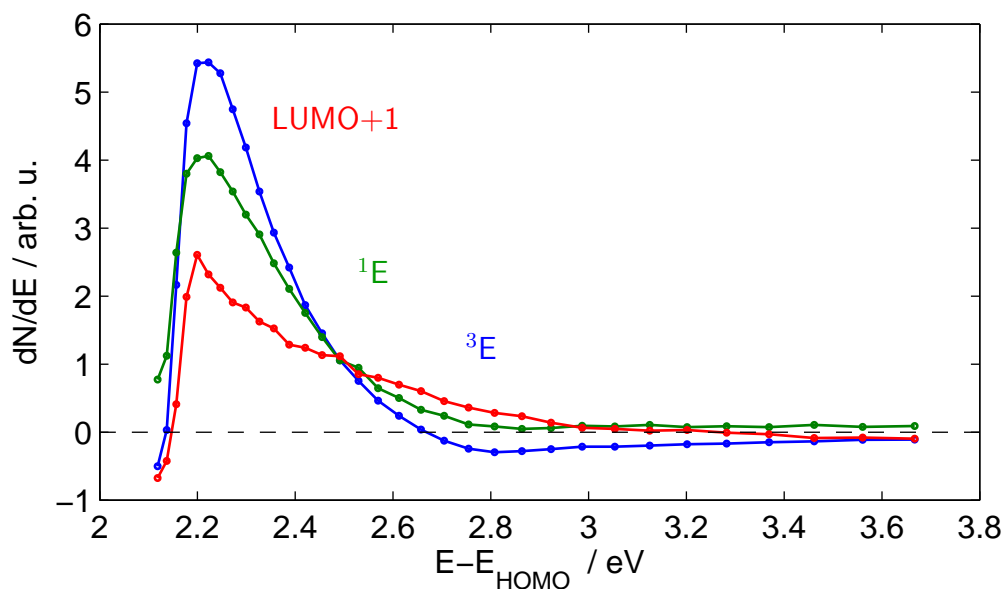


Figure 3.39: Cold preparation time-delay spectrum separated into three dynamic spectra. The corresponding state dynamics are shown in figure 3.40 .

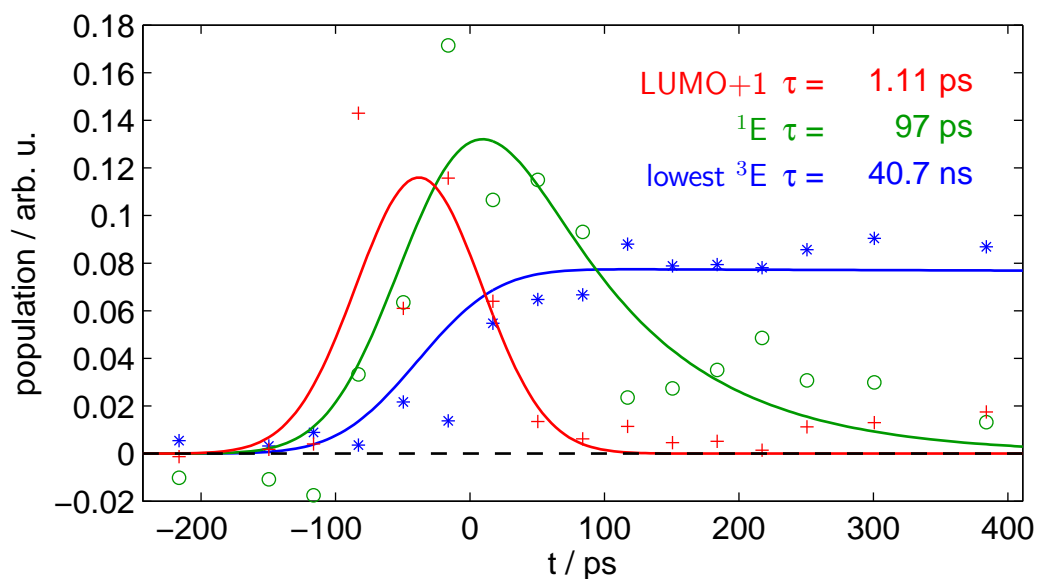


Figure 3.40: Cold preparation state dynamics. The corresponding dynamic spectra are shown in figure 3.39. Pump photon energy: 3.19 eV. Probe photon energy 4.7 eV.

3 *Two-photon photoemission on fullerite films*

2.4 eV. The dynamic spectrum of the singlet exciton dominates at 2.5 eV and at energies above 3.0 eV. The dynamic spectrum of the exciton with an electron in the LUMO+1 dominates above 2.6 eV and has its positive TM at 2.9 eV.

3.4.3 Conclusions

On the warm preparation and on the cold preparation the pump efficacy is very low at 2.4 eV (517 nm), is low and constant in the range from 2.9 to 3.3 eV (from 428 to 376 eV), and high at 3.5 eV (354 nm).

On the coldly prepared fullerite sample a long lifetime state appears in the time-delay spectrum at such high energy that it is visible using probe photons with an energy of 4.71 eV.

The temperature of the substrate during the condensation of the C₆₀ molecules has a big influence on the creation of lattice defects, which in turn modifies the electronic structure. These defects lead to defect states within the conduction band gap and thus to a significant background signal in the two-photon photoemission.

4 Summary

In the present investigation the electronic structure of a fullerite film on the Cu(111) surface is investigated by means of two-photon photoemission. Electronic states already reported in the literature are identified in the measurements. The dynamic spectra of the states exhibit some differences to the dynamic spectra already reported in literature, which also vary. Using 80 ps pulse duration and up to 97 ns delay every time-delay spectrum is a superposition of the triplet exciton, the lowest singlet exciton and the excited singlet exciton with overlapping dynamic spectra and distinct state dynamics. Using 100 ns pulse duration the singlet excitons cannot be separated any more. Using the 25 μ s delay, which are available only in this case, two different triplet excitons can be separated. Thus also in this case every time-delay spectrum is a superposition of three states with overlapping dynamic spectra and distinct state dynamics.

The density of traps in thin films is high enough for them to be considered as an integral part of the time-delay spectrum. Following known recipes the number of different kinds of traps is kept low by using a single crystal substrate with low lattice mismatch (Cu(111)), filling the crucible with the highest purity fullerite powder commercially available, degassing it in UHV, condensing and annealing the first monolayer (ML), and condensing the following ML at a minimal temperature of 360 K with a controlled rate of 1/300 ML/s (lower for lower pressure and higher for higher sample temperature). For the photoemission the sample is cooled down to 140 K to suppress photopolymerisation. It seems to be advantageous to cool down

| LUMO lowest triplet singlet exciton | | chemical potential μ | LUMO excited singlet excitons | LUMO band minimum | LUMO+1 exciton band centre | LUMO+2 exciton | method or figure |
|-------------------------------------|-----|--------------------------|-------------------------------|-------------------|----------------------------|----------------|------------------|
| | | 1.9 | | | 2.8 | 3.9 | figure 3.1 |
| 1.4 | 1.7 | | 2.1 | | | | figure 3.16 |
| 1.3 | 1.8 | | | | | | figure 3.13 |
| 1.4 | 1.8 | | | | | | figure 3.7 |
| 1.4 | 1.8 | | | | | | figure 3.18 |
| 1.5 | 1.9 | | | | | | figure 3.28 |
| | | | 2.1 | | 2.7 | | figure 3.33 |

Table 4.1: Energetic positions / eV referenced to the HOMO inferred by different experiments. Additionally, a HOMO-1 band is visible in UPS 1.2 eV below the HOMO (in figure 1.6 and partly cut-off in figure 2.7).

4 Summary

with maximal 1 K/s until the phase transition is certainly passed, to reduce the number of dislocations due to the sudden change of the lattice constant.

In table 4.1 the spectral position of the triplet exciton is 1.4 eV (886 nm) and as such on the low energy side of the reported values in the literature. This may be due to different traps present in the respective preparations or emphasised by the respective measurement method. The average of the measured energies of the lowest singlet exciton is 1.8 eV (689 nm), which is in agreement with the literature. The dynamic spectra with a large signal around 2.3 eV (539 nm) are interpreted as excited singlet excitons in agreement with the majority of the literature. No compulsory reason for the interpretation as mainly free electrons [39] is found. The strong signal of the excited excitons at low kinetic electron energies is interpreted as due to the photoemission process. In separate measurements with higher fluence the LUMO+1 exciton is visible at 2.8 eV and the LUMO+2 exciton is visible at an energy of 3.9 eV, which is also in agreement with the known literature.

The lifetime of the triplet exciton is 94 μ s, and it stays constant if varying the number of MLs between 9 and 19. This proves that the decay path into the substrate does not reduce the lifetime of the trapped triplet exciton. Increasing the temperature from 140 K to 295 K it is shown that above 200 K the lifetime decreases reaching 47 μ s at 295 K. The publication coming closest to the present investigation measured the triplet lifetime in photopolymerised fullerite at 81 K and yielded 15 μ s [40]. The measurements by Kabler and coworkers [40] are coming closets in their intent to the present investigation and yielded a triplet lifetime in photopolymerised fullerite at 81 K of 15 μ s [40].

The lowest singlet exciton has a lifetime of 1020 ps in agreement with Eberhardt and coworkers [39] (1.8 eV, 998 ps).

At no fluence the second order effects (2PPE) dominate over first-order effects (PES) and higher-order effects are negligible. Therefore, the fluence of each laser shot is recorded, and the fluence dependence can, if the fluence variation is high enough, be separated into discrete orders by means of a polynomial fit. Regarding the higher order effects, the decrease of the lifetime and the efficacy of the lowest singlet exciton is in agreement with the results by Kabler and coworkers [11].

In agreement with photoabsorption measurements by Eklund and coworkers [44] the efficacy is very low at a pump photon energy of 2.4 eV (517 nm), is low and constant in the range from 2.9 to 3.3 eV (from 428 to 376 nm), and high at 3.5 eV (354 nm). This can be rationalized by the following: The transition from the HOMO to the LUMO+1 at 2.8 eV (443 nm) and the transition from HOMO-1 into the LUMO at 3.3 eV (376 nm) photon energy lead to a double peak with a shallow valley in between.

4.1 German translation

In der vorliegenden Arbeit wird die elektronische Struktur von Fullerit-Filmen, die auf einer Cu(111)-Oberfläche kondensiert sind, mittels zeitaufgelöster Zweiphotonenphotoemission untersucht. Schon in der Literatur bekannte Zustände können in den Messungen identifiziert werden. Die Form der Spektren der Zustände weisen einige Unterschiede zu den Spektren in der Literatur auf, die sich untereinander auch unterscheiden. Bei Verwendung von 80 ps dauernden Pulsen und einer maximalen Verzögerung von 97 ns ist jedes Zeitverzögerungs-Spektrum eine Überlagerung des Triplett-Exzitons, des niedrigsten Singlett-Exzitons und der angeregten Singlett-Exzitonen mit überlappenden dynamischen Spektren und unterscheidbarer Zustandsdynamik. Bei Verwendung von 100 ns dauernden Pulsen können die Singlett-Exzitonen nicht mehr unterschieden werden, aber aufgrund der dann möglichen maximalen Verzögerung von 25 μ s können dafür zwei verschiedene Triplett-Exzitonen unterschieden werden. Also ist auch in diesem Fall jedes dynamische Spektrum eine Überlagerung von drei Zuständen mit überlappenden dynamischen Spektren und unterscheidbarer Zustandsdynamik.

Die Dichte der Gitterdefekte in dünnen Filmen ist hoch genug, um ihn als integralen Bestandteil der Zeitverzögerungs-Spektrum zu betrachten. Bekannten Rezepten folgend wird die Anzahl der Arten von Defekten gering gehalten durch Verwendung eines Einkristall-Substrats mit geringer Gitterfehlpassung (Cu(111)), Füllung des Tiegels mit Fullerite-Pulver von höchster kommerziell erhältlichen Qualität, Ausgasen im UHV, Kondensation und Anlassen der ersten Monolage und Kondensation der folgenden Monolagen bei einer Substrat-Temperatur von mindestens 360 K und einer kontrollierten Rate von einer Monolage jede 300 s (niedriger bei niedrigeren Druck und höher bei höherer Proben temperatur). Für die Photoemission wird die Probe auf 140 K abgekühlt, um Photo-Polymerisation zu unterdrücken. Dabei erscheint es vorteilhaft, mit maximal 1 K/s abzukühlen bis der Phasenübergang sicher vollzogen ist, um die Zahl der Versetzungen aufgrund der sprungartige Änderung der Gitterkonstante gering zu halten.

In Tabelle 4.1 ist die spektrale Position des Triplett Exzitons mit 1,4 eV (886 nm) eher auf der niedrigen Seite der in der Literatur bekannten Werte angesiedelt. Das liegt wahrscheinlich an den energetischen Unterschieden der Bindungsstärke an die verschiedenen Gitterdefekte und der Empfindlichkeit der verschiedenen Messmethoden auf die verschiedenen Gitterdefekte. Das niedrigste Singlett-Exziton liegt in Übereinstimmung mit der Literatur im Mittel bei 1,8 eV (689 nm). Die dynamischen Spektren mit einem starken Signal bei 2,3 eV (539 nm) werden als angeregte Singlett-Exzitonen interpretiert, was in Einvernehmen mit dem Großteil der Literatur geschieht. Es konnte kein zwingender Grund gefunden werden für die Interpretation, dass dieses Signal hauptsächlich von freien Elektronen [39] herrührt. Das starke Signal der angeregten Exzitonen bei niedriger kinetischer Energie der

4 Summary

Elektronen wird wahrscheinlich durch den Photoemissionsprozess erzeugt. In einer getrennten Messung mit höherer Laserpuls-Fluenz erscheint das LUMO+1 Exziton bei 2.8 eV und des LUMO+2 Exziton bei 3.9 eV, was auch mit der bekannten Literatur übereinstimmt.

Die Lebenszeit des Triplett-Exzitons wird zu $94 \mu\text{s}$ bestimmt, und sie bleibt konstant, falls man die Zahl der Monolagen zwischen 9 und 19 variiert. Das zeigt, dass der Zerfallskanal in das Substrat die Lebenszeit des Defekt-gebundenen Triplett Excitons nicht reduziert. Bei Erhöhung der Temperatur von 140 K auf 295 K zeigt sich, dass sich ab 200 K die Lebenszeit reduziert und bei 295 K einen Wert von $47 \mu\text{s}$ erreicht. Die Messungen von Kabler und Mitarbeitern [40] kommen in ihrer Zielsetzung der hier vorliegenden Arbeit am nächsten, und sie ergaben eine Lebenszeit des Triplett-Exzitons in Photo-polymerisiertem Fullerite bei 81 K [40] von $15 \mu\text{s}$. Das niedrigste Singlett-Exziton hat eine Lebenszeit von 1020 ps, was übereinstimmt mit dem Wert von Eberhardt und Mitarbeitern (1,8 eV, 998 ps).

Es existiert keine Fluenz bei der Effekte 2.Ordnung (Zweiphotonenphotoemission) über Effekte 1.Ordnung (Photoemission) dominieren und Effekte höherer Ordnung vernachlässigbar sind. Deshalb wird die Fluenz jedes Laserpulses mitgeschrieben und die Fluenz-Abhängigkeit kann, bei genügender Fluenz-Varianz, in die verschiedenen Ordnungen getrennt werden, indem man ein Polynom anfittet. Bezüglich der höheren Ordnungen kann gesagt werden, dass die Abnahme der Lebenszeit und der Pump-Wirksamkeit des niedrigsten Singlett-Exzitons übereinstimmt mit den Ergebnissen von Kabler und Mitarbeitern [11].

In Übereinstimmung mit Photoabsorptionsmessungen von Eklund und Mitarbeitern [44] ist die Pump-Wirksamkeit sehr niedrig bei 2,4 eV Photonenenergie (517 nm), ist niedrig und konstant im Bereich der Photonenenergien von 2,9 bis 3,3 eV (428 bis 376 nm) und hoch bei 3,5 eV (354 nm). Das kann folgendermaßen erklärt werden: Der Übergang vom HOMO in den LUMO+1 bei 2,8 eV (443 nm) und der Übergang vom HOMO-1 in den LUMO bei 3,3 eV (376 nm) führen zu einer Doppelspitze mit einem flachen Tal dazwischen.

A Ellipsometry details

In this appendix some more details for section 2.1.1 are presented. The diagonal polarizer leads to identical amplitudes in s and p polarization (with respect to the sample):

$$a_{s1} = a_{p1}$$

Following the Jones calculus [130] this is expressed as a vector, and in ellipsometry the intensity is typically normed (here to 2):

$$\begin{bmatrix} a_{s1} \\ a_{p1} \end{bmatrix} = \begin{bmatrix} 1 \\ 1 \end{bmatrix}$$

The light is reflected by the sample. The r_s and r_p are calculated in a lengthy way. The angle of incidence in the set-up in the present investigation is 60° . l is the index of the layer, where: 0 = vacuum, 1 = C_{60} , 2 = Cu .

$$n = \begin{bmatrix} 1 & + & 0i \\ 2.12 & + & 0.0327i \\ 25.4 & + & 1.23i \end{bmatrix} \quad (\text{A.1})$$

The refractive index of fullerite is taken from Ren and coworkers [43].

Definition of some abbreviations:

$$\begin{aligned} k &= 2\pi/(532 \text{ nm}) \\ s &= \sin(60^\circ/360^\circ \cdot 2\pi) \\ k_\perp &= l \rightarrow k\sqrt{n_l^2 - s^2} \end{aligned}$$

The transmission and reflection is described by Fresnel equations,

$$\begin{aligned} F = (k_0, k_1, \frac{n_1}{n_0}) &\rightarrow \begin{bmatrix} r_{s01} & t_{s01} \\ r_{p01} & t_{p01} \end{bmatrix} \\ &= \begin{bmatrix} k_0 + k_1 & 0 \\ 0 & k_0 \frac{n_1}{n_0} + k_1 \frac{n_0}{n_1} \end{bmatrix}^{-1} \begin{bmatrix} k_0 & - & k_1 & 2k_0 \\ k_0 \frac{n_1}{n_0} & - & k_1 \frac{n_0}{n_1} & 2k_0 \end{bmatrix}, \end{aligned} \quad (\text{A.2})$$

with k being k_\perp in the indicated medium (0 or 1) and with n being the index of refraction in the indicated medium (0 or 1). Note that these indices 0 and 1 are defined within this function and upon calling this function will be replaced

A Ellipsometry details

with indices in accordance with equation A.1. Further note that $r_{10} = -r_{01}$. The propagator through the fullerite layer is given by $P = \exp(ik_{\perp}z)$ with z being the thickness. Let a_1 denote the amplitude of the electric field of the wave propagating into the fullerite film measured just below the surface. Let a_2 denote the amplitude of the electric field of the wave propagating out of the fullerite film measured just above the interface to the Cu(111). The boundary conditions are expressed as follows:

$$\begin{bmatrix} t_{01} \\ 0 \\ r_{01} \end{bmatrix} \bullet a_0 = \begin{bmatrix} -1 & -P_1 r_{01} & 0 \\ P_1 r_{12} & -1 & 0 \\ 0 & P_1 t_{10} & -1 \end{bmatrix} \bullet \begin{bmatrix} a_1 \\ a_2 \\ a_3 \end{bmatrix}$$

Here the polarization indices have been omitted. Matrix inversion yields

$$a_3 = \left(\frac{r_{01} + r_{12}(r_{01}^2 + t_{10}t_{01})P^2}{1 + r_{12}r_{01}P^2} \right) \cdot a_0 \quad .$$

One factor can be eliminated by inserting the Fresnel equations A.2 (note that the second factor in the first line originally was the denominator):

$$\begin{aligned} & (r_{01}^2 + t_{10}t_{01}) \cdot \left(k_0 \frac{m_0}{m_1} + k_1 \frac{m_1}{m_0} \right)^2 \\ = & \left(k_0 \frac{m_1}{m_0} - k_1 \frac{m_0}{m_1} \right)^2 + 2k_1 k_0 \\ = & \left(k_0 \frac{m_1}{m_0} \right)^2 + \left(k_1 \frac{m_0}{m_1} \right)^2 - 2k_1 k_0 + 4k_1 k_0 \\ = & \left(k_0 \frac{m_1}{m_0} + k_1 \frac{m_0}{m_1} \right)^2 \end{aligned}$$

Here:

$$\frac{m_1}{m_0} = \begin{cases} 1 & \text{s polarization} \\ \frac{n_1}{n_0} & \text{p polarization} \end{cases} \quad .$$

This finally leads to equation 2.1.

B References

- [1] S. Minomura, editor. *Solid State Physics Under Pressure: Recent Advances With Anvil Devices* D Reidel Pub Co (Dordrecht, Boston, London), (1985)
- [2] J. Kepler. *Harmonice mundi Opera Omnia (Frankfurt)* **5**, 75–334 (1619)
- [3] H. W. Kroto, J. R. Heath, S. C. O'Brien, R. F. Curl, and R. E. Smalley. C_{60} : Buckminsterfullerene *Nature* **318**, 162 (1985)
- [4] T.P.I. Saragi and J. Salbeck. Organic heterostructure field-effect transistors using C_{60} and amorphous spirolinked compound *Appl. Phys. Lett.* **89**, 253516 (2006)
- [5] T.D. Anthopoulos, B. Sigh, N. Marjanovic, N.S. Sariciftci, A.M. Ramil, H. Sitter, M. Cölle, and D.M. de Leeuw. High performance n-channel organic field-effect transistors and ring oscillators based on C_{60} fullerene films *Appl. Phys. Lett.* **89**, 213504 (2006)
- [6] G. Yu, J. Goa, J.C. Hummelen, F. Wudl, and A.J. Heeger. Polymer photovoltaic cells: Enhanced efficiencies via a network of internal donor-acceptor heterojunctions *Science* **270**, 1789 (1995)
- [7] A.K. Pandey and J.-M. Nunzi. Efficient flexible and thermally stable pentacene/ C_{60} small molecule based organic solar cells *Appl. Phys. Lett.* **89**, 213506 (2006)
- [8] C. L. Yang, Z. K. Tang, W. K. Ge, J. N. Wang, Z. L. Zhang, and X. Y. Jian. Exciton diffusion in light-emitting organic thin films studied by photocurrent spectra *Appl. Phys. Lett.* **83**, 1737–1739 (2003)
- [9] X. Y. Sun, B. F. Ding, Q. L. Song, X. Y. Zheng, X. M. Ding, and X. Y. Hou. Dissociation of excitons in the C_{60} film studied by transient photovoltage measurements *Appl. Phys. Lett.* **93**, 063301 (2008)
- [10] M.R. Wasielewski, M.P. O'Neil, K.R. Lykke, M.J. Pellin, and D.M. Gruen. Triplet states of Fullerenes C_{60} and C_{70} : Electron paramagnetic resonance spectra, photophysics, and electronic structures *J. Am. Chem. Soc.* **113**, 2774 (1991)

B References

- [11] J.P. Long, S.J. Chase, and M.N. Kabler. Photoelectron spectroscopy and dynamics of excitons in C_{60} and photopolymerized C_{60} films *Chem. Phys. Lett.* **347**, 29 (2001)
- [12] Carsten Marzok. Laserdesorption von NO von C_{60} -Filmen *Diplomarbeit* University of Münster (2004)
- [13] T. Hoger, C. Marzok, R.T. Jongma, and H. Zacharias. Laser desorption of NO from a thick C_{60} film *Surf. Sci.* **600**, 3590 (2006)
- [14] Daniel Grimmer. NO Laserdesorption von $C_{60}/Cu(111)$ *Diplomarbeit* University of Münster (2006)
- [15] J. C. Slater. The theory of complex spectra *Phys. Rev.* **34**, 1293 (1929)
- [16] C.C.J. Roothaan. New developments in molecular orbital theory *Review of Modern Physics* **23**, 69 (1951)
- [17] G.G.Hall. The molecular orbital theory of chemical valency. viii. a method of calculating ionization potentials *Proc. R. Soc. A* **205**, 541–522 (1951)
- [18] Wolfgang Nolting. *Grundkurs Theoretische Physik 5 Quantenmechanik. Teil 2: Anwendungen* Viewig, (1997)
- [19] S. Satpathy, V. P. Antropov, O. K. Andersen, O. Jepsen, O. Gunnarsson, and A. I. Liechtenstein. Conduction-band structure of alkali-metal-doped C_{60} *Phys. Rev. B* **46**, 1773 (1992)
- [20] G. E. Scuseria. Ab initio theoretical predictions of the equilibrium geometries of C_{60} , $C_{60}H_{60}$ and $C_{60}F_{60}$ *Chem. Phys. Lett.* **176**, 423–427 (1991)
- [21] Linus Pauling. The nature of the chemical bond. application of results obtained from the quantum mechanics and from a theory of paramagnetic susceptibility to the structure of molecules. *J. Am. Chem. Soc.* **53**, 1367 (1931)
- [22] G. Gensterblum. Structural, vibrational and electronic proerties of fullerene and epitaxial C_{60} (111) films grown on GeS (001): a review *J. Elect. Spec. Rel. Ph.* **81**, 89 (1996)
- [23] B. Friedman. Electronic absorption spectra in C_{60}^- and C_{60}^+ *Phys. Rev. B* **48**, 2743 (1993)
- [24] K. Harigaya and S. Abe. Optical- absorption spectra in fullerenes C_{60} and C_{70} : Effects of Coulomb interactions, lattice fluctuations, and anisotropy *Phys. Rev. B* **49**, 16746–16753 (1994)
- [25] R. Eder, A.-M. Janner, and G. A. Sawatzky. Theory of nonlinear optical response of excitons in solid C_{60} *Phys. Rev. B* **53**, 12786 (1996)

- [26] T. Hara, S. Narita, S. Kumei, and T. Shibuya. Complete TDA and RPA calculations on the electronic transitions of Fullerene-C₆₀ in the CNDO/S and INDO/S approximations *International J. of Quantum Chemistry* **85**, 136–161 (2001)
- [27] J. Frenkel. On the transformation of light into heat in solids. I *Phys. Rev.* **37**, 17 (1931)
- [28] G. H. Wannier. The structure of electronic excitation levels in insulating crystals *Phys. Rev.* **52**, 191 (1937)
- [29] O. Echt, S. Yao, and R. Deng. Vibrational energy dependence of the triplet lifetime of isolated, photoexcited C₆₀ *J. Phys. Chem. A* **108**, 6944 (2004)
- [30] M. Hedén, A. V. Bulgakov, K. Mehlig, and E. E. B. Campbell. Determination of the triplet state lifetime of vibrationally excited C₆₀ *J. Chem. Phys.* **118**, 16 (2003)
- [31] P. Rudolf, M.S. Golden, and P.A. Brühwiler. Studies of fullerenes by the excitation, emission, and scattering of electrons *J. Elect. Spec. Rel. Ph.* **100**, 409 (1999)
- [32] N. Troullier and J.L. Martins. Structural and electronic properties of C₆₀ *Phys. Rev. B* **46**, 1754 (1992)
- [33] E.L. Shirley and S.G. Louie. Electron excitation in solid C₆₀: energy gap, band dispersion, and effects of orientational disorder *Phys. Rev. Lett.* **71**, 133 (1993)
- [34] O. Gunnarson, S. Satpathy, O. Jepsen, and O.K. Anderson. Orientation of C₆₀ clusters in solids *Phys. Rev. Lett.* **67**, 3002 (1991)
- [35] G. Gensterblum, J.-J. Pireaux, P.A. Thiry, R. Caudano, T. Buslaps, R.L. Johnson, G. Le Lay, V. Aristov, R. Günther, A. Taleb-Ibrahimi, G. Indlekofer, and Y. Petrov. Experimental evidence for 400 meV valence-band dispersion in solid C₆₀ *Phys. Rev. B* **48**, 14756 (1993)
- [36] T.R. Ohno, Y. Chen, S.E. Harvey, G.H. Kroll, J.H. Weaver, R.E. Haufler, and R.E. Smalley. C₆₀ bonding and energy-level alignment on metal and semiconductor surfaces *Phys. Rev. B* **44**, 13747 (1991)
- [37] J.-M. Themlin, S. Bouzidi, F. Coletti, J.-M. Debever, G. Gensterblum, L.-M. Yu, J.-J. Pireaux, and P.A. Thiry. One-dimensional commensurability and conduction-band dispersion in heteroepitaxial C₆₀ on GeS *Phys. Rev. B.* **46**, 15602 (1992)

B References

- [38] S. Link, A. Scholl, R. Jacquemin, and W. Eberhardt. Electron dynamics at a Ag/C₆₀ metal - semiconductor interface *Sol. State Comm.* **113**, 689 (2000)
- [39] R. Jacquemin, S. Kraus, and W. Eberhardt. Direct Observations of the dynamics of excited electronic states in solids: f-sec time resolved photoemission of C₆₀ *Sol. State Comm.* **105**, 449 (1998)
- [40] J.P. Long, S.J. Chase, and M.N. Kabler. Excited-state photoelectron spectroscopy of excitons in C₆₀ and photopolymerized C₆₀ films *Phys. Rev. B* **64**, 205415 (2001)
- [41] G. Dutton and X.-Y. Zhu. Distance-dependent electronic coupling at molecule-metal interfaces: C₆₀/Cu(111) *J. Phys. Chem. B* **108**, 7788 (2004)
- [42] A. Goldoni, C. Cepek, and S. Modesti. First-order orientational-disordered transition on the (111) surface of C₆₀ *Phys. Rev. B* **54**, 2890 (1996)
- [43] S.L. Ren, Y. Wang, A.M. Rao, E. McRae, J.M. Holden, T. Hager, K. Wang, W-T. Lee, H.F. Ni, J. Selegue, and P.C. Eklund. Ellipsometric determination of the optical constants of C₆₀ (Buckminsterfullerene) films *Appl. Phys. Lett.* **59**, 2678 (1991)
- [44] Y. Wang, J.M. Holden, A.M. Rao, P.C. Eklund, U.D. Venkateswaran, D. Eastwood, R.L. Lidberg, G. Dresslhaus, and M.S. Dresselhaus. Optical absorption and photoluminescence in pristine and photopolymerized C₆₀ solid films *Phys. Rev. B* **51**, 4547 (1995)
- [45] A.-M. Janner, R. Eder, B. Koopmans, H.T. Jonkman, and G.A. Sawatzky. Excitons in C₆₀ studied by temperature-dependent optical second-harmonic generation *Phys. Rev. B* **52**, 17158 (1995)
- [46] R. Könenkamp, R. Engelhardt, and R. Henninger. Photogeneration and carrier transport in C₆₀ films *Sol. State Comm.* **97**, 285–288 (1996)
- [47] R. Könenkamp, G. Priebe, and B. Pietzak. Carrier mobilities and influence of oxygen in C₆₀ films *Phys. Rev. B* **60**, 11804 (1999)
- [48] B. Mishori, Y. Shapira, A. Belu-Marian, M. Manciuciu, and A. Devenyi. Studies of C₆₀ thin films using surface photovoltage spectroscopy *Chem. Phys. Lett.* **264**, 163 (1997)
- [49] S. Kazaoui, N. Minami, Y. Tanabe, H. J. Byrne, A. Eilmes, and P. Petelenz. Comprehensive analysis of intermolecular charge-transfer excited states in C₆₀ and C₇₀ films *Phys. Rev. B* **58**, 7689 (1998)
- [50] W. Guss, J. Feldmann, E. O. Göbel, C. Taliani, H. Mohn, W. Müller, P. Häussler, and H.-U. ter Meer. Fluorescence from X traps in C₆₀ single crystals *Phys. Rev. Lett.* **72**, 2644 (1994)

- [51] D. J. van den Heuvel, I. Y. Chan, E. J. J. Groenen, J. Schmidt, and G. Meijer. Phosphorescence of C_{60} at 1.2 K *Chem. Phys. Lett.* **231**, 111–118 (1994)
- [52] H.J. Byrne, W. Maser, W.W. Rühle, A. Mittelbach, W. Höhle, H.G. von Schnering, B. Movaghar, and S. Roth. Time-resolved photoluminescence of solid state fullerenes *Chem. Phys. Lett.* **204**, 461 (1993)
- [53] R.W. Lof, M.A. van Veenendaal, B. Koopmans, H.T. Jonkman, and G.A. Sawatzky. Band gap, excitons, and Coulomb interaction in solid C_{60} *Phys. Rev. Lett.* **68**, 3924 (1992)
- [54] E.L. Shirley, L.X. Benedict, and S.G. Louie. Excitons in solid C_{60} *Phys. Rev. B* **54**, 10970 (1996)
- [55] W.Z. Wang, C. L. Wang, A.R. Bishop, and Z.B. Su. Dynamic Jahn-Teller effect in C_{60} : Self-trapped excitons and resonant Raman scattering *Phys. Rev. B* **51**, 10209–10212 (1995)
- [56] E. Teller G. Herzberg. Schwingungsstruktur der Elektronenübergänge bei mehratomigen Molekülen *Z. Phys. Chem. (Leipzig) B* **21**, 410 (1933)
- [57] G. Orlandi and W. Siebrand. Theory of vibronic intensity borrowing. Comparison of Herzberg-Teller and Born-Oppenheimer coupling *J. Chem. Phys.* **58**, 4513–4523 (1973)
- [58] M. S. Dresselhaus, G. Dresselhaus, and P. C. Eklund. *Science of Fullerenes and Carbon Nanotubes* Academic Press (Fribourg), (1995)
- [59] A. Sassara, G. Zerza, M. Chergui, F. Negri, and G. Orlandi. The visible emission and absorption spectrum of C_{60} *J. Chem. Phys.* **107**, 8731–8741 (1997)
- [60] T. Hara, Y. Nomura, S. Narita, H. Ito, and T.-I. Shibuya. Electric-dipole forbidden transitions in C_{60} : oscillator strengths induced by the spin-orbit coupling *J. of Molecular Structure (Theochem)* **589**, 139 (2002)
- [61] M. Matus, H. Kuzmany, and E. Sohmen. Self-trapped polaron exciton in neutral fullerene C_{60} *Phys. Rev. Lett.* **68**, 2822 (1992)
- [62] N. Manini, P. Gattari, and E. Tosatti. Jahn-Teller spectral fingerprint in molecular photoemission: C_{60} *Phys. Rev. Lett.* **91**, 196402 (2003)
- [63] H. Thomas Etheridge III, R. D. Averitt, N. J. Halas, and R. Bruce Weisman. C_{60} triplet lifetimes: Vibrational energy dependence from 0 to 80,000 cm^{-1} *J. Phys. Chem.* **99**, 11306 (1995)
- [64] A. G. Stepanov, M. T. Portella-Oberli, A. Sassara, and M. Chergui. Ultrafast intramolecular relaxation of C_{60} *Chem. Phys. Lett.* **358**, 516–522 (2002)

B References

- [65] A. Watanabe, O. Ito, M. Watanabe, H. Saito, and M. Koishi. Picosecond time-resolved near-IR spectra of C_{60} excited states by pump-probe measurements using a probe beam based on broad-band optical parametric generation *Chem. Commun.* **173**, 117 (1996)
- [66] J. W. Arbogast, C. S. Foote, and M. Kao. Electron transfer to triplet C_{60} *J. Am. Chem. Soc.* **114**, 2277 – 2279 (1992)
- [67] B. Hellsing, A. Eiguren, and E. V. Chulkov. Electron-phonon coupling at metal surfaces *J. Phys.: Cond. Matt.* **14**, 5959–5977 (2002)
- [68] A. Goldoni, L. Petaccia, G. Zampieri, S. Lizzit, C. Cepek, E. Gayone, J. Wells, and Ph. Hofmann. Evidence for bandlike dispersion in $K_6C_{60}(110)$ films *Phys. Rev. B* **74**, 045414 (2006)
- [69] E. Grivei, B. Nysten, M. Cassart, A. Demain, and J-P. Issi. Specific heat of fullerenes extract *Sol. State Comm.* **85**, 73–75 (1993)
- [70] K.-D. Tsuei and P.D. Johnson. Charge transfer and a new image state of C_{60} on Cu(111) surface studied by inverse photoemission *Sol. State Comm.* **101**, 337 (1996)
- [71] K.-D. Tsuei, J.-Y. Yuh, C.-T. Tzeng, R.-Y. Chu, S.-C. Chung, and K.-L. Tsang. Photoemission and photoabsorption study of C_{60} adsorption on Cu(111) surfaces *Phys. Rev. B* **56**, 15412 (1997)
- [72] X. Lu, M. Grobis, K. H. Khoo, Steven G. Louie, and M. F. Crommie. Charge transfer and screening in individual C_{60} molecules on metal substrates: A scanning tunneling spectroscopy and theoretical study *Phys. Rev. B* **70**, 115418 (2004)
- [73] L. Wang and H. Cheng. Rotation, translation, charge transfer, and electronic structure of C_{60} on Cu(111) surfaces *Phys. Rev. B* **69**, 045404 (2004)
- [74] G. Dutton and X.-Y. Zhu. Unoccupied states in C_{60} thin films probed by two-photon photoemission *J. Phys. Chem. B* **106**, 5975 (2002)
- [75] K. Kuhnke, R. Becker, M. Epple, and K. Kern. C_{60} exciton quenching near metal surfaces *Phys. Rev. Lett.* **79**, 3246 (1997)
- [76] A. Sassara, G. Zerza, and M. Chergui. Phosphorescence of C_{60} in rare gas matrices *Chem. Phys. Lett.* **261**, 213–220 (1996)
- [77] W.-C. Hung, C.-D. Ho, C.-P. Liu, and Y.-P. Lee. Laser-induced fluorescence and phosphorescence of C_{60} isolated in solid Ne *J. Phys. Chem.* **100**, 3927–3932 (1996)

- [78] M. Bennati, A. Grupp, M. Mehring, K.P. Dinse, and J. Fink. Pulsed EPR on the photoexcited triplet state of C_{60} fullerene *Chem. Phys. Lett.* **200**, 440 (1992)
- [79] G. Gensterblum, J.-J. Pireaux, P.A. Thiry, R. Caudano, J.P. Vigneron, P. Lambin, A.A. Lucas, and W. Krätschmer. High-resolution electron-energy-loss spectroscopy of thin films of C_{60} on Si(100) *Phys. Rev. Lett.* **67**, 2171 (1991)
- [80] A.-M. Janner, H.T. Jonkman, and G.A. Sawatzky. Second-harmonic generation spectroscopy: A technique for selectively probing excitons *Phys. Rev. B* **63**, 085111 (2001)
- [81] T. Hoger, D. Grimmer, and H. Zacharias. UV laser desorption of nitric oxide from semiconducting $C_{60}/Cu(111)$ *Appl. Phys. A* **88**, 449–458 (2007)
- [82] L. Kronik and Y. Shapira. Surface photovoltage spectroscopy of semiconductor structures: at the crossroads of physics, chemistry and electrical engineering *Surf. Interface Anal.* **31**, 954–965 (2001)
- [83] T. Rabenau, A. Simon, R. K. Kremer, and E. Sohmen. The energy gaps of fullerene C_{60} and C_{70} determined from the temperature dependent microwave conductivity *Z. Phys. B* **90**, 69–72 (1993)
- [84] H. Lüth. *Surfaces and Interfaces of Solid Materials* Springer-Verlag (Berlin, Heidelberg, New York), (1997)
- [85] S. Hüfner. *Photoelectron Spectroscopy* Springer-Verlag (Berlin, Heidelberg, New York), (1995)
- [86] K. Oura, V.G. Lifshits, A.A. Saranin, A.V. Zotov, and M. Katayama. *Surface Science* Springer-Verlag (Berlin, Heidelberg, New York), (2003)
- [87] C.N. Berglund and W.E. Spicer. Photoemission Studies of Copper and Silver: Theory *Phys. Rev.* **136**, A1030 (1964)
- [88] R. Courths and S. Hüfner. Photoemission on Copper *Phys. Rep.* **112**, 53 (1984)
- [89] D. A. Shirley. High-resolution x-ray photoemission spectrum of the valence bands of gold *Phys. Rev. B* **5**, 4709 (1972)
- [90] M. Göppert-Mayer. Über Elementarakte mit zwei Quantensprüngen *Ann. Phys.* **401**, 273–294 (1931)
- [91] M. Sheik-Bahae, D.J. Hagan, and E.W. Van Stryland. Dispersion and band-gap scaling of the electronic Kerr effect in solids associated with two-photon absorption *Phys. Rev. Lett* **65**, 96–99 (1990)

B References

- [92] P.A. Franken, A.E. Hill, C.W. Peters, and G. Weinreich. Generation of optical harmonics *Phys. Rev. Lett.* **7**, 118–119 (1961)
- [93] W. Kaiser and C. G. B. Garrett. Two-photon excitation in $\text{CaF}_2: \text{Eu}^{2+}$ *Phys. Rev. Lett.* **7**, 229 – 231 (1961)
- [94] H. Ueba and T. Mii. Theory of energy- and time-resolved two-photon photoemission from metal surfaces - influence of pulse duration and excitation condition *Appl. Phys. A* **71**, 537 (2000)
- [95] D. Hilbert, L. Nordheim, and J. von Neumann. Über die Grundlagen der Quantenmechanik *Mathematische Annalen* **98**, 1–30 (1927)
- [96] T. Hertel, E. Knoesel, M. Wolf, and G. Ertl. Ultrafast Electron Dynamics at $\text{Cu}(111)$: Response of an Electron Gas to Optical Excitation *Phys. Rev. Lett.* **76**, 535 (1996)
- [97] R. Loudon. *The Quantum Theory of Light* Oxford Science Publications, Great Clarendon Street, Oxford, (1997)
- [98] J. Hubbard. Electron correlations in narrow energy bands *Proc. R. Soc. A* **276**, 238–257 (1963)
- [99] N. W. Ashcroft and N.D. Mermin. *Solid state physics* Thomson learning, (1976)
- [100] E. Rotenberg, C. Enkvist, P. A. Brühwiler, A. J. Maxwell, and N. Mårtensson. Local-field effects on photoemission of C_{60} *Phys. Rev. B* **54**, R5279 (1996)
- [101] A.J. Maxwell, P.A. Brühwiler, A. Nilsson, N. Mårtensson, and P. Rudolf. Photoemission, autoionization, and X-ray-absorption spectroscopy of ultrathin-film C_{60} on $\text{Au}(110)$ *Phys. Rev. B* **49**, 10717 (1994)
- [102] P.A. Brühwiler, A.J. Maxwell, P. Rudolf, C.D. Gutleben, B. Wästenberg, and N. Mårtensson. C 1s autoionization study of electron hopping rates in solid C_{60} *Phys. Rev. Lett.* **71**, 3721 (1993)
- [103] C. Jabs. *Flugzeit-Photoelektronenspektroskopie an Ni(111)- und NiO(111)/Ni(111)-Oberflächen* Diplomarbeit, Universität Essen, (1996)
- [104] B. Göhler. Zeitaufgelöste Zweiphotonenphotoelektronenspektroskopie von C_{60} -Filmen *Diplomarbeit* University of Münster (2007)
- [105] D.M. Poirier, D.W. Owens, and J.H. Weaver. Alkali-metal-fulleride phase equilibria *Phys. Rev. B* **51**, 1830 (1995)

- [106] A. Popović, G. Dražič, and J. Marsel. Mass spectrometric investigations of fullerenes. I. vapour pressure over the C_{60} / C_{70} binary system *Rapid Communications in Mass Spectrometry* **8**, 985–990 (1994)
- [107] K.-I Iizumi, K. Saiki, and A. Koma. Investigation of the interaction between a C_{60} epitaxial film and a $Si(111)-7\times 7$ surface by electron energy loss spectroscopy *Surface Science* **518**, 126 (2002)
- [108] J.A. Larsson, S.D. Elliott, J.C. Greer, J. Repp, G. Meyer, and R. Allenspach. Orientation of individual C_{60} molecules adsorbed on $Cu(111)$: Low-temperature scanning tunneling microscopy and density functional calculations *Phys. Rev. B* **77**, 115434–9 (2008)
- [109] T. Hashizume, K. Motai, X.D. Wang, H. Shinohara, Y. Saito, Y. Maruyama, K. Ohno, Y. Kawazoe, Y. Nishina, H.W. Pickering, Y. Kuk, and T. Sakurai. Intramolecular structures of C_{60} molecules adsorbed on the $Cu(111)-(1\times 1)$ surface *Phys. Rev. Lett.* **71**, 2959 (1993)
- [110] W.W. Pai, C.L. Hsu, M.C. Lin, K.C. Lin, and T.B. Tang. Structural relaxation of adlayers in the presence of adsorbate-induced reconstruction: $C_{60}/Cu(111)$ *Phys. Rev. B* **69**, 125405 (2004)
- [111] David P. Craig. Emission centres in anthracene single crystals *J. Chem. Soc., Faraday Trans. 2* **74**, 292–303 (1978)
- [112] A. Fartash. Orientational epitaxy of high-quality C_{60} films on $Ag(111)$ *Phys. Rev. B* **52**, 7883 (1995)
- [113] Michael Bass, editor. *Handbook of Optics*, volume 2 McGraw-Hill, 2nd edition, (1994)
- [114] K. Finsterbusch, R. Urschel, and H. Zacharias. Tunable, high-power, narrow-band picosecond IR radiation by optical parametric amplification in KTP *Appl. Phys. B* **74**, 319 (2002)
- [115] K. Finsterbusch, R. Urschel, and H. Zacharias. Fourier-transform-limited, high-power picosecond optical parametric oscillator based on periodically poled lithium niobate *Appl. Phys. B* **70**, 741 (2000)
- [116] K. Finsterbusch. Effiziente Erzeugung von weit durchstimmbaren, schmalbandigen Pikosekunden-Laserpulsen im nahen und mittleren Infrarot, *Dissertation*, University of Münster (2004)
- [117] J. Kutzner and H. Zacharias. VUV generation by frequency tripling the third harmonic of a picosecond kHz Nd:YLF laser in xenon and mercury vapour *Appl. Phys. B* **66**, 571 (1998)

B References

- [118] D.H. Jundt. Temperature-dependent Sellmeier equation for the index of refraction, n_e , in congruent lithium niobate *Optics Lett.* **22**, 1553–1555 (1997)
- [119] U.K. Sapaev, I.A. Kulagin, and T.Usmanov. Theory of second-harmonic generation for limited laser beams in nonlinear crystals *J. Opt. B.* **5**, 355 (2003)
- [120] P.A. Thomas, I.J Tebbutt, and A.M. Glazer. Potassium titanyl phosphate, KTiOPO_4 . I. experimental investigation of optical gyration, absolute optical chirality and twinning *J. Appl. Cryst.* **24**, 963–967 (1991)
- [121] J. J. Zondy, M. Abed, and S. Khodja. Twin-crystal walk-off-compensated type-II second-harmonic generation: single-pass and cavity-enhanced experiments in KTiOPO_4 *J. Opt. Soc. Am. B* **11**, 2368 (1994)
- [122] R. Paucksch. *Ein- und Zwei-Photonen-Photoemissionsspektroskopie von Oberflächenzuständen an Ni(111)* Dissertation, Universität Essen, (2000)
- [123] F. Theilmann, R. Matzdorf, G. Meister, and A. Goldmann. Influence of surface structural disorder on linewidths in angle-resolved photoemission spectra *Phys. Rev. B* **56**, 3632–3635 (1997)
- [124] M. Weinelt. Time-resolved two-photon-photoemission from metal surfaces *J. Phys. Condens. Matter* **14**, 1099–1141 (2002)
- [125] T. Stephan, J. Zehnpfenning, and A. Benninghoven. Correction of dead time effects in time-of-flight mass spectrometry *J. Vac. Sci. & Techn. A* **12**, 405–410 (1994)
- [126] S. Okamoto and S. Sakurai. Singular value decomposition analysis of time-resolved small-angle X-ray scattering during morphological transition in a block copolymer *J. Appl. Cryst.* **36**, 982–985 (2002)
- [127] M. Schmidt, S. Rajagopal, Z. Ren, and K. Moffatyz. Application of singular value decomposition to the analysis of time-resolved macromolecular X-ray data *Biophys. J.* **84**, 2112–2129 (2002)
- [128] G. Golub and W. Kahan. Calculating the singular values and pseudo-inverse of a matrix *J. Soc. Industr. and Appl. Mathem.: Series B, Numerical Analysis* **2**, 205–224 (1965)
- [129] Donald W. Marquardt. An algorithm for Least-Squares estimation of nonlinear parameters *Journal of the Society for Industrial and Applied Mathematics* **11**, 431–441 (1963)
- [130] R. C. Jones. New calculus for the treatment of optical systems *J. Opt. Soc. Am.* **31**, 488–493 (1941)

C Lebenslauf

| | |
|---------------------|--|
| Name | Arne Christian Rosenfeldt |
| Geburtsdatum | 01.06.1977 |
| Geburtsort | Braunschweig |
| Staatsangehörigkeit | Deutsch |
| Eltern | Heinrich Leonhard Rosenfeldt Ilse Ingeborg Rosenfeldt geb. Mehrfort |

Schulausbildung

| | |
|------------|--|
| 1983–1987 | Grundschule Bassen |
| 1988–1990 | Pestalozzischule, Oyten |
| 1991–1996 | Cato Bontjes van Beek Gymnasium, Achim |
| 21.05.1996 | Allgemeine Hochschulreife |

Studium

| | |
|------------|--|
| 1997–1999 | Studium der Physik an der Universität Bremen |
| 02.09.1998 | Diplom-Vorprüfung |
| 2000–2002 | Hauptstudium der Physik an der Westfälische Wilhelms-Universität Münster |
| 2001–2002 | Diplomarbeit in experimenteller Physik Lineare und nichtlineare, rasternde Laser-Mikroskopie an Kristallen mit Domänen und anderen Proben |
| 13.03.2002 | Diplomprüfung |

Promotionsstudium

| | |
|------------|-------------------------|
| 11.08.2002 | Beginn der Dissertation |
|------------|-------------------------|

Berufstätigkeit

| | |
|-----------|---|
| 2001–2002 | Studentische Hilfskraft am Physikalischen Institut der Westfälische Wilhelms-Universität Münster |
| 2002 | Wissenschaftliche Hilfskraft am Physikalischen Institut der Westfälische Wilhelms-Universität Münster |
| 2002–2008 | Wissenschaftlicher Mitarbeiter am Physikalischen Institut der Westfälische Wilhelms-Universität Münster |

Münster, 01.04.2009 ,

D Acknowledgment

The project has been financially supported by the Deutsche Forschungsgemeinschaft in the Schwerpunktprogramm SPP1093 “Dynamik von Elektronentransferprozessen an Grenzflächen”.

I thank everybody who helped me to succeed with my investigation.

This thesis was created in the workgroup of Prof. Dr. H. Zacharias. I thank him for the interest in the progress of my investigation and many proposals and discussions, which allowed me to learn a lot.

I thank Roland Schliesing for introduction into the experiment, the support, and the transfer of the already large C_{60} bibliography. A special thank goes to Benjamin Göhler, for the friendly support and cooperation, especially at the long measurement sessions at night. He contributed a lot of knowledge and suggestions, which entered the investigation. I also thank him and Tim Hoger for helping me with \LaTeX and reading through my manuscript.

For technical support at small and bigger challenges I thank Tamara Kleimann, Frank Wahlert, and Sven Eppenhoff very much. I thank Werner Mai for the competent electronic support.

I thank all members of the workgroup for the enjoyable atmosphere, helpful suggestions, barbeque, swimming, tabletop football, and Zaferna journeys.

I thank my wife Ohkwha for understanding and taking most of the care of our daughter Ines. I thank my parents for long term support and reading through my manuscript.